PLASMON ENHANCED NEAR-FIELD INTERACTIONS IN SURFACE COUPLED NANOPARTICLE ARRAYS FOR INTEGRATED NANOPHOTONIC DEVICES

by
AMITABH GHOSHAL
BA, Hanover College, 2001
MS, University of Central Florida, 2006

A dissertation submitted in partial fulfillment of the requirements
for the degree of Doctor of Philosophy
in the College of Optics and Photonics
at the University of Central Florida
Orlando, Florida

Spring Term 2010

Major Professor: Pieter G. Kik

© 2010 Amitabh Ghoshal

ABSTRACT

The current thrust towards developing silicon compatible integrated nanophotonic devices is driven by need to overcome critical challenges in electronic circuit technology related to information bandwidth and thermal management. Surface plasmon nanophotonics represents a hybrid technology at the interface of optics and electronics that could address several of the existing challenges. Surface plasmons are electronic charge density waves that can occur at a metal-dielectric interface at optical and infrared frequencies. Numerous plasmon based integrated optical devices such as waveguides, splitters, resonators and multimode interference devices have been developed, however no standard integrated device for coupling light into nanoscale optical circuits exists. In this thesis we experimentally and theoretically investigate the excitation of propagating surface plasmons via resonant metal nanoparticle arrays placed in close proximity to a metal surface. It is shown that this approach can lead to compact plasmon excitation devices.

Full-field electromagnetic simulations of the optical illumination of metal nanoparticle arrays near a metal film reveal the presence of individual nanoparticle resonances and collective grating-like resonances related to propagating surface plasmons within the periodic array structure. Strong near-field coupling between the nanoparticle and grating resonances is observed, and is successfully described by a coupled oscillator model. Numerical simulations of the effect of nanoparticle size and shape on the excitation and dissipation of surface plasmons reveal that the optimum particle volume for efficient surface plasmon excitation depends sensitively on the particle shape. This observation is quantitatively explained in terms of the shape-dependent optical cross-section of the nanoparticles.

Reflection measurements on nanoparticle arrays fabricated using electron-beam lithography confirm the predicted particle-grating interaction. An unexpected polarization-dependent splitting of the film-mediated collective resonance is successfully attributed to the existence of out-of plane polarization modes of the metal nanoparticles. In order to distinguish between the excitation of propagating surface plasmons and localized nanoparticle plasmons, spectrally resolved leakage radiation measurements are presented. Based on these measurements, a universally applicable method for measuring the wavelength dependent efficiency of coupling free-space radiation into guided surface plasmon modes on thin films is developed. Finally, it is shown that the resonantly enhanced near-field coupling the nanoparticles and the propagating surface plasmons can lead to optimized coupler device dimensions well below 10 μm.

This work is dedicated to the pursuit of science – to all science, to curiosity, discovery, and learning, and their place in the story of humanity.

ACKNOWLEDGEMENTS

I would like to express my heartfelt gratitude to my parents Swapan Ghoshal and Rajkumari Ghoshal. If I were to choose one thing they did for me that most directly led to me being here writing these words, it would be that they always convinced me that I could do whatever I dreamed of doing. But they did more than that. My parents helped me learn to contextualize my dreams in reality – so I would be able to go beyond dreaming and realize the dreams as well. Without them, I may not even have dreamt of pursuing this highest of degrees, let alone achieve it.

Special thanks to my advisor Professor Pieter Kik, for allowing me the privilege of being one of his first students. Professor Kik has been deeply involved in my scientific projects from conception and brainstorming to the nitty-gritty of doing the research and the minutiae of writing and editing manuscripts. His quest for perfection has been an example for me during the years I have worked with him; I hope to always carry that standard with me.

Oleksandr Savchyn's positive outlook and strong work ethic has always been an inspiration to me. I am also thankful to him for setting up some characterization instruments that were essential for a few measurements presented in the following chapters. Seyfollah Toroghi joined our group very recently. In the short time that he has been here, he found the time to help me with some measurements, for which I am thankful.

Nathan Bickel shared his broad expertise in operating many of the tools I used to fabricate the samples discussed in the following chapters. Without his knowledge, and his willingness to help troubleshoot problems, I would have spent many more hours in the cleanroom. For his help, I am thankful.

In the past seven years, I have come to realize deeply how much my success depends on the support of the people around me. Without their willing friendship and encouragement, my journey to this day would have been inestimably more difficult. To these people I am deeply thankful.

Professor Winston Schoenfeld and Professor Michael Bass have been generous with their time in mentoring me, beyond any obligation to do so. For that I am grateful. John Ahrens has always been a willing friend and mentor. I have grown to value his perpetual support and unique wisdom more and more with each passing year. His words have been few but wise, and always apropos. Ivan Divliansky has been instrumental in this work, both by sharing his expertise in electron-beam lithography, and also by encouraging and guiding me when necessary.

Richard Zotti has been instrumental in teaching me to design and make some of the tools I have used to do these experiments. For his willing sharing of his skill and the gift of his friendship, I am grateful.

The time Troy Anderson and I have spent in formulating a perspective of what our graduate work means in the context of our personal and professional goals was extremely valuable to me. I will always cherish those weekly meals together! I am thankful to Amy Thompson for her friendship; she helped me keep a sense of perspective in life when I needed it most. If there is a friend who has always been there, it is my old friend Haimanti Nag Weld. Our conversations have had no limits, and I truly value them.

My uncle Manohar Awatramani and my aunt Nargis Awatramani have been instrumental in helping me start this journey that began in 1998 and culminates with this degree. Their willing help and encouragement was critical and I have a deep gratitude for their confidence in me.

Clarisse Mazuir, Josue Davila-Rodriguez, K Shavitranuruk, Hyo-Yang Ahn, Christopher Brown, Forrest Ruhge, and Kimberly Ruhge, are friends I have developed through these interesting years – for their involvement in my life during these years, I am grateful.

Finally, I am thankful to the CREOL staff for always being there to help with any and everything. This effort is possible by virtue of their behind-the-scenes work.

TABLE OF CONTENTS

LIST OF FIGURES

LIST OF TABLES

1 INTRODUCTION

The use of surface plasmons (SPs) continues to develop in a broad variety of fields due to their unique properties. Surface plasmons are charge density waves propagating on the interface between a metal and a dielectric[1]. Surface plasmons have two key properties that make them attractive for applications. First, the electromagnetic modes associated with surface plasmons can be strongly confined, making surface plasmons on metal films possible candidates for nanoscale integrated optical communication devices. Examples of such devices are surface plasmon based waveguides[2-16], surface plasmon based modulators and switches[17], interferometers and ring resonators[18], nanoparticle chain waveguides[19, 20], and surface plasmon based lasers[21, 22]. Second, the oscillatory nature of the surface modes enables the resonant enhancement of the highly confined electromagnetic fields, allowing the use of surface plasmons for the enhancement of optical processes that require high electric field strengths. Examples of surface plasmon based applications include biodetection using Raman scattering[23-27], biodetection using measurement of small changes in refractive index via prism coupling[28, 29], nonlinear signal generation[30, 31], optical limiting[32, 33], and plasmon enhanced optical absorption in thin film solar cells[34-39].

The interest in the use of surface plasmons for on-chip communication is driven by the expected bottlenecks in electronic circuits due to known practical and fundamental physical limitations of capacitance and heating.[40-42] Surface plasmon nanophotonics combines features of both optics and electronics and presents the possibility of overcoming several of the challenges in on-chip communication applications.[43-46] In photonic applications, strongly coupled resonances play a key role.[18-20, 47] In this thesis, we study the strong coupling displayed by nanoparticles arranged in a regular array coupled to surface plasmons on a nearby metal film. To enable a thorough understanding of the work presented in this thesis, the following sections present a brief overview of the theoretical underpinnings of the research done in this field.

1.1 Theory

1.1.1 Surface Plasmons on Planar Films

As mentioned above, surface plasmons are charge oscillations that can exist at a metal-dielectric interface. The properties of surface plasmon modes can be found from Maxwell's equations by ensuring that solutions satisfy the wave equation inside homogeneous media, and by applying electromagnetic boundary conditions at the metal-dielectric interface.

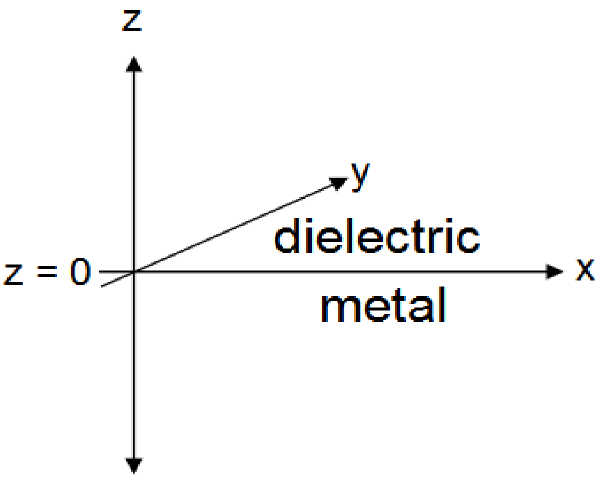

Figure 1.1. The coordinate system used for the description of surface plasmons in this section.

In the coordinate system shown in Figure 1.1, $z > 0$ is the dielectric, $z < 0$ is the metal, and the metal-dielectric interface is in the x-y plane. The field solutions in the dielectric are of the form:

$$
\begin{aligned}
H_d &= \left(0, H_{y,d}, 0\right) e^{i\left(k_x x + k_{z,d} z - \omega t\right)} \\
E_d &= \left(E_{x,d}, 0, E_{z,d}\right) e^{i\left(k_x x + k_{z,d} z - \omega t\right)}
\end{aligned}
\tag{1.1}
$$

The field solutions in the metal are of the form:

$$
\begin{aligned}
H_m &= \left(0, H_{y,m}, 0\right) e^{i\left(k_x x + k_{z,m} z - \omega t\right)} \\
E_m &= \left(E_{x,m}, 0, E_{z,m}\right) e^{i\left(k_x x + k_{z,m} z - \omega t\right)}
\end{aligned}
\tag{1.2}
$$

where the subscripts *d* and *m* indicate dielectric and metal respectively, the subscripts *x*, *y*, and *z* indicate the coordinate dimensions, *H* is the magnetic field, *E* is the electric field, k_i is the projection of the wave vector along direction *i*, and ω is the angular frequency. In the above, the plasmon wavevector k_x is related to the angular frequency ω through the known dispersion relationship:[1]

$$
k_x = \frac{\omega}{c} \sqrt{\frac{\varepsilon_m \varepsilon_d}{\varepsilon_m + \varepsilon_d}}
\tag{1.3}
$$

where $k_x = 2\pi/\lambda_x$ with λ_x the plasmon wavelength, *c* is the speed of light in vacuum, and $\varepsilon_m(\omega)$ and $\varepsilon_d(\omega)$ are the dielectric functions of the metal and the dielectric respectively. Note that the dielectric functions here are complex, leading to a complex wave vector. The normal wavevector in either the metal or the dielectric is found from the relation $k_x^2 + k_z^2 = \varepsilon_i \left(\omega/c\right)^2$, leading to:

$$
k_{z,i} = \sqrt{\varepsilon_i \left(\frac{\omega}{c}\right)^2 - k_x^2}\,.
\tag{1.4}
$$

$k_{z,i}$ is predominantly imaginary, corresponding to electric fields that decay exponentially with increasing distance from the interface. The electric field strength decays with the inverse of k_x'' – the imaginary part of k_x – and the intensity of the surface plasmon is proportional to the square of the electric field. Thus, the characteristic frequency dependent propagation length L_p of the surface plasmon at the interface between a metal and a lossless dielectric is given by

$$L_p = \frac{1}{|2k_x''|} = \frac{c}{\omega}\left(\frac{\varepsilon_m' + \varepsilon_d}{\varepsilon_m' \varepsilon_d}\right)^{3/2} \frac{\varepsilon_m'^2}{\varepsilon_m''} \quad (1.5)$$

where ε_m' and ε_m'' are the real and imaginary parts of the metal dielectric function respectively. Based on existing literature data[48, 49] for dielectric functions of silver and silica (SiO_2), one finds that surface plasmons at a silver-silica interface excited with light at a free-space wavelength λ_0 = 850 nm can propagate over a distance of 100 μm, while surface plasmons excited at λ_0 = 1.5 μm can propagate as far as 390 μm. These types of propagation lengths are sufficiently long to create functional plasmon based optical devices. Gold has a larger imaginary contribution to the dielectric function at this frequency, and gives a correspondingly shorter propagation length of 18 μm at a free-space wavelength λ_0 = 850 nm, and 87 μm at a free-space wavelength λ_0 = 1.5 μm.

Figure 1.2 shows a dispersion curve of a surface plasmon at a Ag-SiO_2 interface, calculated using equation (1.3) and based on experimentally obtained dielectric properties[48]. Note that there is no surface plasmon propagation above 5.25×10^{15} rad/s, corresponding to the localized surface plasmon resonance frequency ω_{SP}. Also note that at low frequencies, the surface plasmon dispersion lies close to the light-line. As a result, the group velocity of the surface plasmon is similar to the group velocity of light in the dielectric at these frequencies.

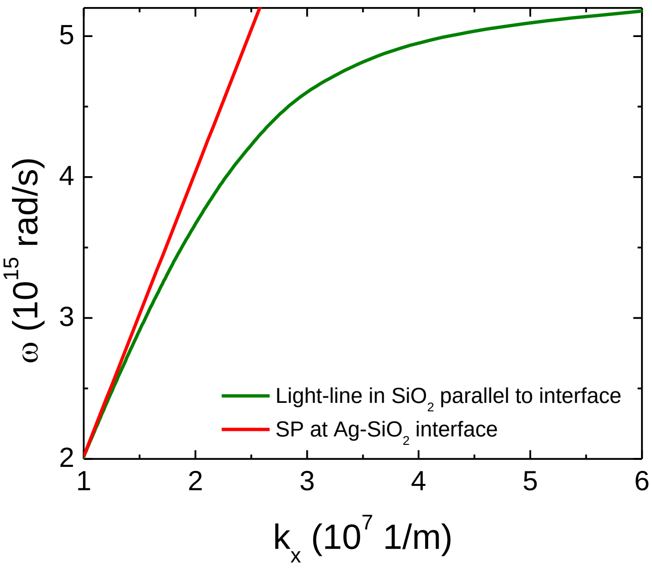

Figure 1.2. Dispersion curve of Ag-SiO_2 surface plasmon based on literature values for the real part of the silver dielectric function. Note that the surface plasmon dispersion curve lies below the light-line in SiO_2.

1.1.2 Surface Plasmons on Metal Nanoparticles

The frequency dependent behavior of spherical sub-wavelength particles is described by Mie theory. When illuminated with light, metal nanoparticles support a resonantly excited dipolar charge oscillation, known as the Fröhlich mode. Due to the resonant nature of the excitation, the magnitude of the local field strength can exceed the driving field by more than an order of magnitude for spherical particles.[50, 51] For ellipsoidal particles excited along one of their main axes this resonance occurs at a frequency that depends on the aspect ratio of the particle axes, the particle orientation relative to the incident field, and the dielectric functions of the particle and its surroundings. This is reflected in the particle polarizability given by:[52]

$$\alpha = V\varepsilon_0 \, \frac{\varepsilon_m - \varepsilon_d}{\varepsilon_d + F(\varepsilon_m - \varepsilon_d)} \tag{1.6}$$

where α is the polarizability along a semi-axis of the nanoparticle, V is the volume of the particle, and ε_0 is the permittivity of free space. F is a shape-dependent factor ranging from 0 to 1 that can be calculated using the integral:

$$F = \int_0^\infty \frac{1}{\left(\sqrt{(q+a^2)(q+b^2)(q+c^2)}\right)(q+c^2)} dq \tag{1.7}$$

where a, b, and c are the semi-axes of the ellipsoid with c being the axis along which the incident light is polarized, and q is a variable of integration. For a sphere, $F = 1/3$. The existence of a Fröhlich mode coincides with the frequency at which the calculated polarizability reaches a maximum. Figure 1.3 shows the calculated resonance frequency of an ellipsoidal Ag nanoparticle in SiO_2 as a function of the axis aspect ratio c/a, with the incident light polarized along the c-axis.

For increasing aspect ratio (increasingly more elongated needle-shaped particles), the resonance frequency of an ellipsoidal particle is increasingly red-shifted. For aspect ratios < 1 (disk-like particles), the particle surface perpendicular to the polarization increasingly resembles a planar film with respect to the illuminating field. Consequently, the resonance frequency blue-shifts and approaches the plasma frequency of the metal which, in this case is approximately 5.25×10^{15} rad/s.

The following sections discuss methods currently used to excite surface plasmons, and will illustrate the relevant issues in designing an efficient far-field to surface plasmon coupler.

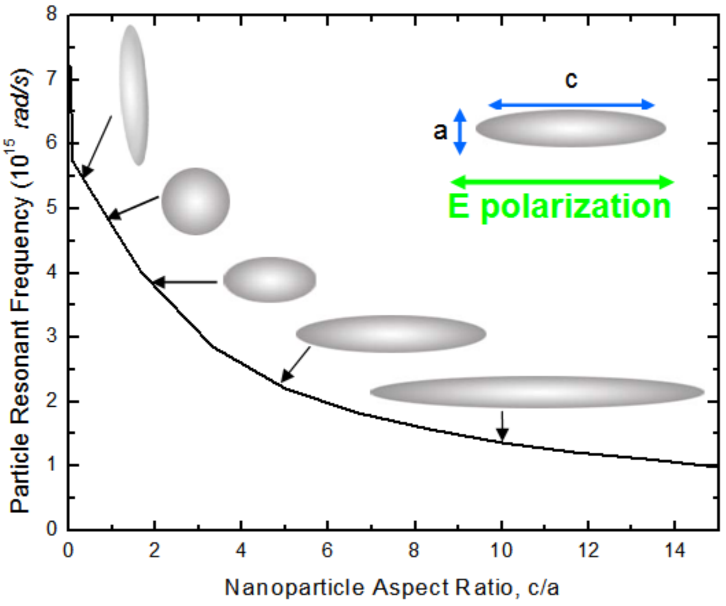

Figure 1.3. Resonance frequency of an ellipsoidal silver nanoparticle in SiO_2 based on literature values for the silver dielectric function. Axes *a* and *b* are assumed equal in length. The incident light is polarized along the *c*-axis.

1.2 Far-Field to Near-Field Coupling

Since surface plasmons on smooth metal surfaces represent bound modes, they cannot be excited by using free-space illumination of a planar surface or interface. This can be seen as a consequence of momentum mismatch: since the surface plasmon wavelength is smaller than the corresponding free-space wavelength, the phase velocity of the incident light cannot be matched to the phase velocity of the surface plasmons. This momentum mismatch can be visualized by comparing the maximum projection of the wavevectors associated with incident light (the light-line) along the surface of the metal, and those of surface plasmons at a given frequency. Surface plasmon modes are found to lie to the right of the light line, indicating that at all frequencies the wavevector of the surface plasmon k_{SP} is greater than the wavevector of the incident light.

The momentum mismatch can be overcome by modifying the wavevector of the incident light, either using high index dielectrics or by introducing inhomogeneities in the dielectric constant of the material near the metal film. Common methods are:

- prism-coupling, involving weak coupling of light with surface plasmons over a relatively large area
- grating coupling, using periodic modulation of a metal surface
- near-field excitation, involving relatively strong light-surface plasmon coupling using individual nanostructures.

In the following, the advantages and disadvantages of these methods are discussed.

1.2.1 Weak Coupling with Large Structures

1.2.1.1 Prism Coupling

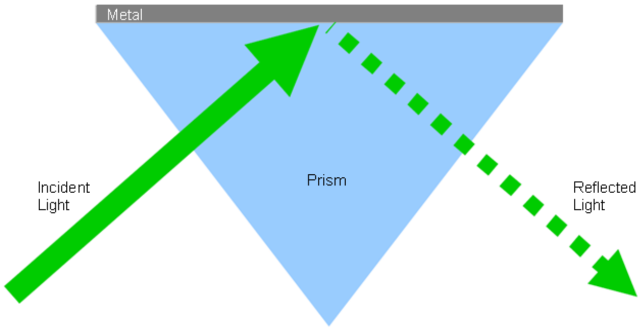

Figure 1.4. A schematic of the Kretchmann geometry for exciting surface plasmons.

Prism coupling is commonly done in the Kretschmann-Raether geometry[1], as shown schematically in Figure 1.4. In this geometry the light undergoes either total internal reflection or specular reflection at the metal-dielectric interface. In the case of total internal reflection, the incident light generates a corresponding evanescent field outside the prism that decays exponentially inside the metal film, resulting in a finite field strength at the metal-air interface. The magnitude of the field at the metal surface depends on the film thickness and the dielectric function of the metal. The wavevector of this field parallel to the interface depends on the angle of incidence of the light and the refractive index of the prism. When the wavevector of the incident light matches that of the surface plasmon at the metal-air interface, surface plasmons will be excited. As the incident beam is scanned through angles greater than the critical angle, the excitation of surface plasmons is observed as a dip in the reflectivity at the angle for optimum coupling. A set of sample reflectivity curves is shown in Figure 1.5.

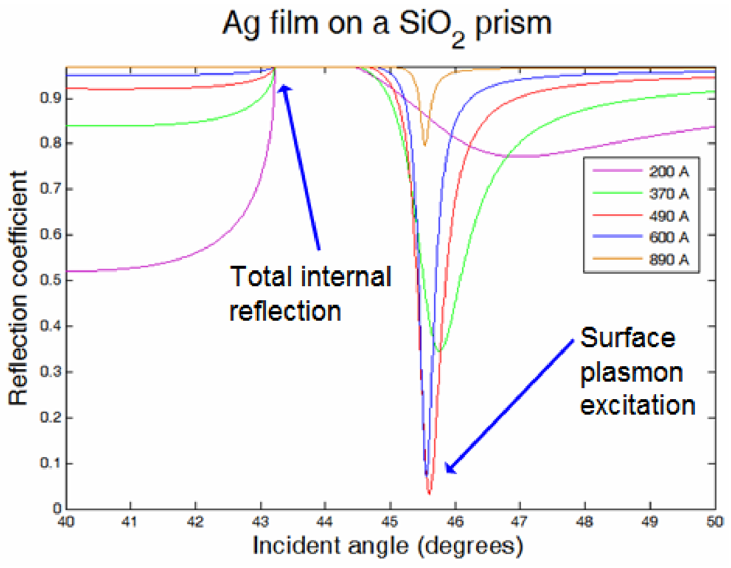

Figure 1.5. Calculated reflectivity as a function of angle in the Kretschmann geometry calculated for silver films with different thickness on an SiO$_2$ prism. The excitation wavelength is 546 nm. Note that the film thicknesses are specified in angstroms.

The Otto setup[1] is a configuration similar to the Kretschmann configuration, and is shown in Figure 1.6. In this case the metal film is deposited on a substrate, and the prism is held at a finite distance from the metal surface. In this configuration, the surface plasmon is excited at the metal-air interface by the evanescent waves that extend across the prism-air-metal surface gap. This method can be used on opaque substrates, but requires precise control over the prism-film spacing.

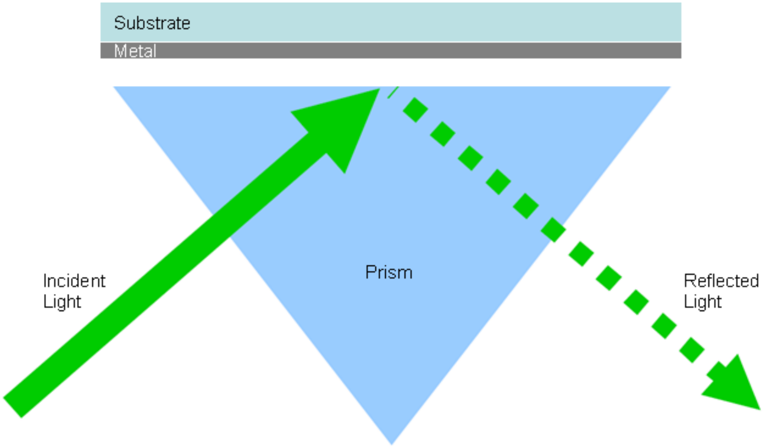

Figure 1.6. A schematic of the Otto geometry for exciting surface plasmons.

In both methods the momentum mismatch between the free-space light and the surface plasmon is overcome by the use of a high index dielectric, as illustrated in Figure 1.7. The green line represents the surface plasmon dispersion curve at the metal-SiO_2 interface, and the red line represents the light-line in SiO_2 for light parallel to the interface. The dashed red line represents the lateral projection of the wavevector of the light-line in a dielectric of refractive index $n = 1.8$ at grazing incidence. The appearance of an intersection of this light-line and the surface plasmon dispersion curve shows that momentum matching can be achieved as long as the light incident from within the dielectric produces a finite field strength at the metal surface. Thus, by changing the angle and frequency of the light in the dielectric, surface plasmons of different wavelength can be excited at the metal-air interface.

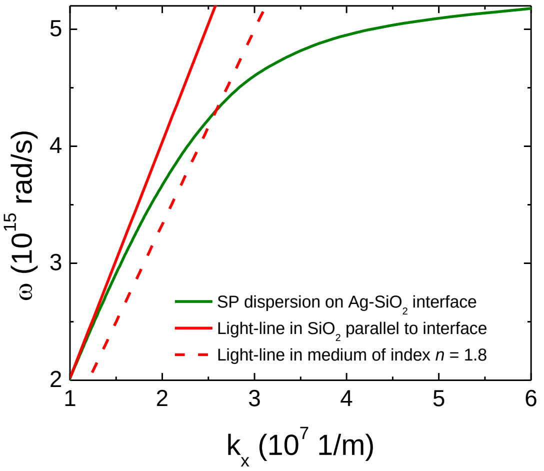

Figure 1.7. The dispersion curve of a surface plasmon at a silver-silica interface (green). The light-line in silica is shown in red, and the light-line in a medium with an index of 1.8 is the dashed red line.

In prism coupling, efficient surface plasmon excitation is achieved by optimizing the thickness of the metal film. The thickness dependent behavior can be understood by describing the film surface as a driven damped Lorentzian oscillator, where the amplitude of the oscillator represents the electric field associated with the surface plasmon. The damping of the surface plasmon mode at the metal surface contains two several contributions: nonradiative loss including surface plasmon damping in the metal due to electron scattering in the metal film, surface scattering of the electrons, and radiative losses due to surface roughness and due to finite coupling of the surface plasmon into the prism. Maximum power is transferred into the surface plasmons when:

- the film is thin enough to obtain significant excitation field amplitude at the metal-air interface under far-field illumination from within the prism
- the film is thick enough so that the evanescent surface plasmon field at the metal-air interface does not introduce significant radiation loss back into the prism

This behavior is clearly observed in Figure 1.5. For films thinner or thicker than 50 nm, the minimum reflectivity is 0.3 or more showing inefficient surface plasmon excitation. For thicknesses smaller than 50 nm, the reflectivity minimum is relatively broad which is indicative of high radiation loss. At an intermediate film thickness (at approximately 50 nm) the reflectivity is seen to drop to almost zero, indicating efficient surface plasmon excitation. Additionally, a narrower reflection minimum is observed, indicative of relatively low radiative damping. At a film thickness in excess of 60 nm, the resonance width does not change significantly, while the reflection minimum becomes less pronounced. In this limit, radiative damping is no longer a significant contribution to the total damping, and the maximum field amplitude is given by the intrinsic surface plasmon damping and the field strength at the metal surface. This interpretation of a driven resonator can also be seen in the mathematical form of the reflection coefficient. At low frequencies, the reflectivity is given by:[1]

$$R = 1 - \frac{4\Gamma_i \Gamma_{rad}}{[k_x - (k_x^2 + \Delta k_x)]^2 + (\Gamma_i + \Gamma_{rad})^2} \tag{1.8}$$

where

$$\Delta k_x = \left[\frac{\omega}{c} \frac{2}{1 + |\varepsilon_{metal}^{'}|} \left(\frac{|\varepsilon_{metal}^{'}|}{|\varepsilon_{metal}^{'}| - 1} \right)^{3/2} e^{(-2|k_x^0| d_1)} \right] r_{01}^{p}(k_x^0) \tag{1.9}$$

and $k_x^0 = \frac{\omega}{c}\sqrt{\varepsilon_0}\sin\theta_0$. In the above, d, Γ_i, Γ_{rad}, θ_0, r_{01}^{p} are the film thickness, the intrinsic and radiative damping, the angle of incidence, and the reflection coefficient of the light traveling from the dielectric to the metal respectively. ε_0 is the permittivity of free-space.

For optimum coupling, it can be seen that the surface plasmon excitation must be ‘resonant’ which in this case means that the driving wavevector must match the surface plasmon wavevector, setting a requirement on the angle of incidence. Additionally, for a fixed Γ_i, optimum excitation efficiency is achieved when Γ_{rad} is equal to Γ_i. Note that the magnitude of the radiative loss term can be modified by changing the thickness of the film. Under this condition, the total field emitted in the reflected direction can be as low as 2%, and the remaining power in the incident beam goes into the surface plasmon excited at the metal-air interface. Such a balance between excitation strength and radiative loss is a key element in any coupler design.

1.2.1.2 Grating Coupling

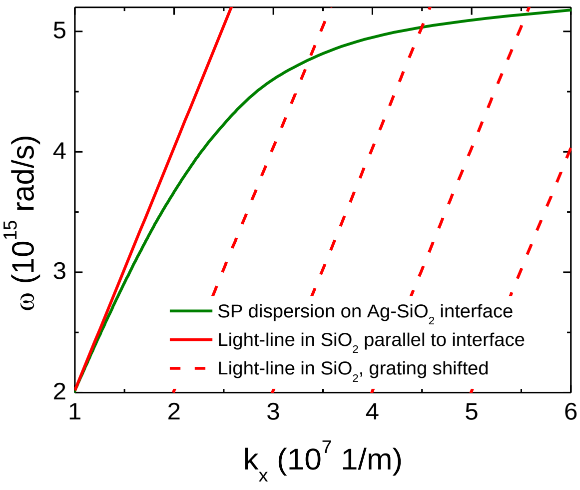

Figure 1.8. The calculated dispersion curve of surface plasmons at a silver-SiO_2 interface based on literature values for the real part of the silver dielectric function. The red line is the light-line in SiO_2, and the dashed lines are the grating-shifted light-line.

In addition to the use of high dielectric constant materials for phase matching, gratings can also be used to couple free-space radiation to surface plasmons. Consider a metallic grating oriented perpendicular to the *x*-*y* plane, with the grating periodicity along the *x*-direction. If the grating period exceeds the surface plasmon wavelength, surface plasmons can be excited on the grating surface. The periodicity of a grating can thus be used to overcome the momentum mismatch between the free-space light and the surface plasmon. A calculated example of this is shown in Figure 1.8. The blue curve is the dispersion curve of surface plasmons at a silver-SiO_2 interface, and the red line is the light-line in the dielectric.

Constructive excitation of surface plasmons on a grating is achieved when the grating equation is satisfied:

$$k_{SP} = k_{//} \pm nG \qquad n = 0, \pm 1, \pm 2, \pm 3, \dots \tag{1.10}$$

where $k_{//}$ is the *x*-projected wavevector of the incident light, k_{SP} is the wavevector of the surface plasmon along the *x*-direction, and G is the grating constant, given by $G=2\pi/L$, where L is the grating period. The wavevector of light in SiO_2, is shifted in *k*-space by the grating. This grating-shifted wavevector for $n = 1$ through 4 are shown in Figure 1.8 as dashed red lines. While the light-line itself does not intersect the surface plasmon dispersion curve, the grating shifted light-lines do intersect with the surface plasmon dispersion curve at several frequencies. As in the case of prism coupling, the intersection of the two gives the frequency at which surface plasmons can be excited. Note that because of the nature of light-grating-surface plasmon interaction, only discrete frequencies can excite surface plasmons at a particular grating period and at a fixed angle of incidence. This allows for wavelength selective coupling.

The efficiency of grating coupling is wavelength dependent, and excitation efficiencies close to 100% have been achieved.[1] The gratings that have been realized are typically created directly in the surface of the metal where the surface plasmon is to be excited. However, dielectric gratings have also been used. For example, a sinusoidally modulated wax grating above an aluminum alloy surface was used to excite surface plasmons in the microwave regime.[53] The coupling efficiency of grating couplers is affected by the grating profile. For example, Giannattasio *et al*. recently showed that for a square grating, a duty cycle of 0.5 is the most efficient in exciting surface plasmons at a silver-air interface, at a free-space wavelength of 543 nm.[54]

1.2.2 Strong Near-Field Coupling with Nanostructures

Prism coupling and grating coupling both make use of constructive excitation over relatively large areas (often hundreds of optical wavelengths in size). Although large area excitation can yield high efficiency, it is not an absolute requirement for achieving efficient coupling. When an electromagnetic field is incident on small physical or dielectric features near a metallic surface, surface charge oscillations are introduced at the discontinuities. These surface charge oscillations introduce localized non-radiating *E*-fields, called the *near field*, that contain high spatial frequency components (large wavevector values). Some of these generated wavevectors can couple to surface plasmon modes on the metal surface. The following sections describe some of the approaches seen in literature, and discuss the role of localized and collective resonances in the excitation process.

1.2.2.1 Near Field Probes

In early works, surface plasmons were excited using a small diameter electron beam incident on a metal surface in the process of electron loss spectroscopy.[55, 56] For exciting surface plasmons optically, features with a size smaller than the plasmon wavelength are required. For example, the tip of a Near-field Scanning Optical Microscope (NSOM) illuminated using far field radiation can be used to excite surface plasmons.[57]

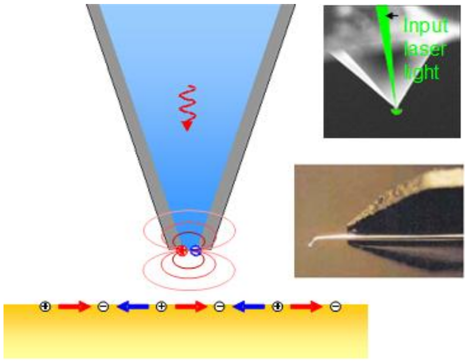

Figure 1.9. A sketch of the oscillatory electric near fields excited at an NSOM tip, and the resulting surface plasmon excitation in a nearby metal film. The light traveling down the tip is assumed to be polarized horizontally. Insets: Mirroscopic (top) and macroscopic (bottom) images of NSOM tips.

An NSOM probe consists of a nano-scale aperture in a metal coating defined on a sharp dielectric object. Different types of NSOM probes exist. One type of tip makes use of a nano-aperture defined on a tapered and metalized optical fiber. A picture of such a fiber based NSOM tip is shown in the bottom right inset in Figure 1.9. The inset in the top right of Figure 1.9 shows a second common type of NSOM tip built on a Si cantilever. The Si is etched using various controlled etch steps leaving a SiO_2 pyramid on the Si cantilever. The cantilever with the SiO_2 pyramid is metalized with aluminum at a controlled angle resulting in an aluminum covered pyramid with an unmetalized apex approximately 80 nm in diameter. Light incident on the nanoaperture generates local fields near the aperture as shown in Figure 1.9. The high spatial frequency components of the local electric field in turn can excite surface plasmons on a metal surface.[57] Surface plasmon excitation using near-field probes is a complex mechanism which makes the determination of the excitation efficiency difficult. It appears that no direct measurements of the surface plasmon excitation efficiency via NSOM probes have been performed.

1.2.3 Particle Arrays Near Surfaces and Interfaces

The examples of surface plasmon excitation discussed above show that the coupling efficiency is affected by the scattering strength of surface features, and the periodicity of these features. The frequency dependent optical response of nanostructures can be engineered by changing the shape, size, and material of the structure. As a consequence of their small size, individual nanostructures have a small interaction area with an incident field, and are consequently expected to be relatively inefficient surface plasmon excitation elements. Large structures with low radiation loss have been shown to enable highly efficient surface plasmon excitation, but implementation of such large structures in nanoscale circuits is undesirable. A combination of the methods described above could enable the development of an optical coupling element with a small footprint and large excitation efficiency. Towards this end, this thesis investigates metal nanoparticle arrays coupled with a metal film to resonantly excite surface plasmons on the metal surface.

1.2.3.1 Optical Response of Nanoparticle Arrays

As discussed above in section 1.1.2, individual nanoparticles can be described as an oscillator with a resonance frequency that is determined by the particle shape. However, when a particle is part of an array, the individual particle behavior is modified by local electric fields that develop due to the structure of the array. Several experiments have been published in literature that investigate this behavior.[19, 58-60] Two major effects that have been observed. The first is the shifting of the particle resonance in dense particle arrays due to the presence of neighboring particles.[60] The second is the collective behavior of the particle array as a grating.[58, 59]

The resonance of a particle in an array can be redshifted or blue-shifted depending on the polarization of the incident light and the particle arrangement. Consider an array of metallic particles as shown in Figure 1.10. The long axis of the particles is c, and the short axes a, and b are assumed equal. The distance between the particles in the x and y directions are d_x and d_y respectively.

In this setup, the light incident on the particle array is polarized along the x-direction. Let us first consider the effect of particles aligned along the x-direction. The charge oscillations induced in an isolated particle (particle 1) create a field distribution which is sketched in Figure 1.10(a). Particle 2, which is drawn in a lighter color, also has a similar field distribution. The dipole field of particle 1 at the center of particle 2 is in the same direction as the field of particle 2. The restoring force on the displaced electron cloud of a particle depends directly on the field inside the particle. Since the field of particle 1 enhances the field inside particle 2, the restoring force is increased, resulting in a blue-shift of the resonance frequency of the Fröhlich mode.

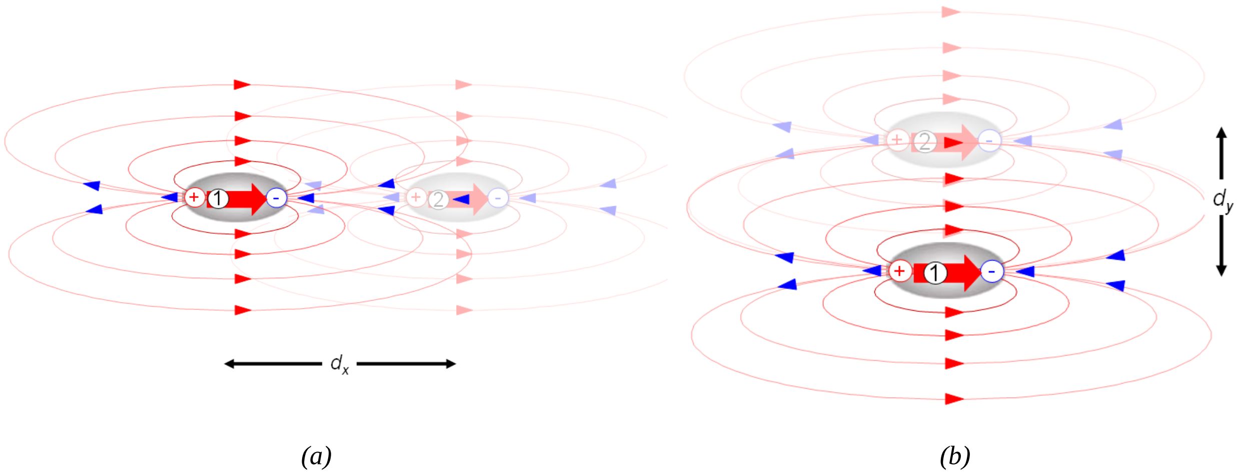

Figure 1.10. A sketch of the field distribution of two neighboring nanoparticles. The excitation field is polarized along the *x*-direction for both sketches.

Now consider the interactions between neighboring particles in the *y*-direction. The fields of two particles are shown in Figure 1.10(b). Here, the field of particle 1 at the center of particle 2 opposes the internal field of particle 2. Thus, as the field strength is reduced inside the particle, the resonance frequency is also decreased.

Clearly, as the distance d_x or d_y increases, the influence of a particle on its neighboring particle reduces. Correspondingly, the deviation of the particle's resonance frequency from its individual resonance frequency decreases. This dependence of particle resonance on inter-particle spacing was demonstrated by Maier *et al*.[19] and Sweatlock *et al*.[60].

The above description is applicable for the near-field region, in which the quasi-static approximation is valid. However, when the inter-particle distance is increased to the order of the wavelength, diffractive contributions start playing an important role. Zou *et al*.[59] studied a one-dimensional array of Ag nanoparticles, of various sizes with various spacings. They found that the scattered light showed the features of the individual dipoles, as well as diffractive features of the entire array.

1.2.3.2 Particle-Film Interaction

As we have seen earlier in this chapter, the electron oscillations of a nanostructure near a surface can couple to surface plasmon modes in the surface. However, surface plasmon excitation is not the only possible near-field interaction in such a system. The presence of a static dipole above a metal surface is well known to result in the creation of an image dipole in the metal.[61] This static case does not account for surface plasmon excitation in the metal surface, or phase differences between the particle surface plasmon oscillations and the surface plasmon oscillations in the metal film. Particle-surface coupling, including the excitation of surface plasmons, has been theoretically and numerically investigated by Takemori *et. al*.[62] who found a distinct red-shift in the absorption spectrum of a Ag sphere above a Ag surface, with the shift increasing with decreasing particle-substrate distance. This red-shift can be understood in terms of interaction of the dipole moment on the nanoparticle with the (partial) image dipole in the metal substrate.

As surface plasmon oscillations in a metal particle can induce surface plasmons in a metal film, similarly, a surface plasmon traveling along a metal surface can induce oscillations in a particle near the surface. These particle surface plasmon oscillations can scatter the surface plasmon into free-space radiation as well as into surface plasmons at the metal surface. Evlyukhin *et al*. investigated the scattering of surface plasmons from a metal surface by ellipsoidal particles[63] and found that particles with their long axis perpendicular to the surface scattered surface plasmons more efficiently than particles with the long axis parallel to the surface. Such shape dependent interaction between surface plasmons and particles will become important in chapter 4.

1.3 Summary

The coupling efficiency of free-space light into surface plasmons is affected by factors such as balance of different damping contributions, the interplay of multiple resonances, and the coupling strength between the various resonances. The coupling efficiency is typically low for isolated or random structures, whereas more efficient coupling can be obtained for extended periodic structures.

While substantial work has been done in order to examine various facets of surface plasmon excitation, the use of intentionally tuned local resonances combined with resonant excitation of surface plasmons has received little attention. We investigate this method in depth using both a theoretical and an experimental approach. Metal nanoparticle arrays near a metal surface provide an ideal system to investigate the role of localized resonances. The particle-surface coupling strength can be optimized by particle-film spacing and particle volume, the resonance frequency of the particles can be tuned using particle shape, and particle-surface plasmon coupling can be further modified by varying the inter-particle spacing. These parameters can be used to develop an optimized structure for far-field to near-field coupling.

1.4 This Thesis

In this thesis we investigate the coupling between metal nanoparticle resonances and collective resonances associated with propagating surface plasmons with the specific goal of exciting propagating surface plasmons.

We begin in Chapter 2 with an investigation of excitation of surface plasmons on a metal film by a nearby infinite array of nanoparticles using full-field electromagnetic simulations. In these simulations individual nanoparticle and grating resonances are observed, and seen to interact strongly. A coupled oscillator model is introduced to describe the interaction between the particle and grating resonances, providing a deeper insight into the coupling mechanism.

In addition to shape, the effect of particle size on excitation and damping of surface plasmons is also investigated via full-field simulations in Chapter 3. These simulations suggest a different optimum particle volume exists for the efficient excitation of surface plasmons for each of the particle shapes studied. Analytical calculations taking into account known relations for optical cross-sections suggest that the optimum particle volume corresponds to a balance between increasing particle-mediated surface plasmon excitation strength and increasing damping of the surface plasmon by the nanoparticles. The analytical calculations provide an easy way for researchers to estimate damping of surface plasmons via nanoparticles without the need for full-field simulations.

A reflection spectroscopy study of the strong coupling between particle and grating resonances in finite arrays is presented in Chapter 4. In addition to observing the predicted grating-particle interaction for the in-plane illumination polarization modes, an additional grating mode associated with the polarization normal to the sample surface is found to be excited due to the finite range of angles in the illumination spot. By changing the illumination conditions, the short and long wavelength modes are determined to correspond to the in-plane and out-of-plane illumination polarizations.

In contrast with the reflection measurements discussed in Chapter 4, Chapter 5 discusses spectrally resolved leakage radiation measurements to explicitly identify propagating surface plasmon modes excited by a nanoparticle array. It is shown that the grating resonances lead to strong leakage radiation signals whereas the previously observed broad reflection minimum associated with the localized surface plasmon resonance on the metal particles appears only as a weak leakage radiation signal. These results demonstrate that in the absence of constructive surface plasmon excitation by a periodic structure, propagating surface plasmon excitation makes up only a minor fraction of the total dissipation of the incident radiation by the nanoparticles.

Based on leakage radiation measurements similar to those in Chapter 5, in Chapter 6 a universally applicable method for measuring the wavelength-dependent efficiency of coupling from free-space light to surface plasmons on thin films is developed. Using this method, the surface plasmon excitation efficiency of the nanoparticle grating coupler is determined to be approximately 3.5% for both grating modes.

Finally, in Chapter 7 the array-size dependent evolution of the surface plasmon excitation using the array-film coupled system is studied using leakage radiation measurements. The excited surface plasmon amplitude exiting the arrays, integrated over all wavelengths, is seen to rapidly reach saturation as a function of array size – at 8 periods or a 4 μm array size. The mechanism of this saturation is discussed by considering the balance between increase of surface plasmon amplitude by neighboring periods and scattering of the already propagating surface plasmon amplitude by these same array periods.

The main conclusions from the work presented in this thesis are summarized in Chapter 8. In addition, recommendations are made for the development of a high efficiency free-space to surface plasmon coupler based on the presented observations.

2 THEORY AND SIMULATION OF SURFACE PLASMON EXCITATION USING METAL NANOPARTICLE ARRAYS

2.1 Introduction

In this chapter we discuss a plasmonic coupling device consisting of a periodic array of ellipsoidal silver nanoparticles embedded in SiO_2 and placed near a silver surface. By tuning the shape of the particles in the array, the nanoparticle plasmon resonance is tuned. At excitation frequencies close to the localized plasmon resonance the resulting enhanced electric fields near the nanoparticles, in turn, excite surface plasmons on the metal film. We have performed finite integration technique simulations[64] of such a plasmon coupler, optimized for operation near a wavelength of 676 nm. Analysis of the frequency dependent electric field at different locations in the simulation volume reveals the separate contributions of the particle and grating resonance to the excitation mechanism. A coupled oscillator model describing the nanoparticle and the metal film as individual resonators is introduced and is shown to reproduce the trends observed in the simulations. Implications of our analysis on the resonantly enhanced excitation of surface plasmons are discussed.

We consider the use of localized plasmon resonances for the excitation of surface plasmons using two-dimensional arrays of metal nanoparticles placed near a metal-dielectric interface. A schematic of such a structure is shown in Figure 2.1. This combination of resonant nanoparticle based surface plasmon excitation and grating coupling may be used to design compact free-space to surface plasmon couplers as well as field enhancement structures. Ellipsoidal metal nanoparticles exhibit a dipolar surface plasmon resonance known as the Fröhlich mode[52] at a frequency that depends on the particle aspect ratio, its dielectric function, and the dielectric function of its surroundings. The resonantly enhanced localized field distribution that can be excited on individual metal nanoparticles contains high spatial frequencies that can couple to propagating surface plasmons on a nearby metal film. By placing such resonant particles in a periodic arrangement near a metal film, surface plasmons excited by multiple particles can be added constructively, resulting in an enhanced surface plasmon excitation efficiency. In this work we numerically investigate excitation of surface plasmons on a silver film using an infinitely extended two-dimensional array of metal nanoparticles near a silver surface. The excited surface plasmon amplitude is studied as a function of excitation frequency and nanoparticle aspect ratio. The results are compared to an analytical model that describes the silver surface and the metal nanoparticles as coupled resonators. We find that the main features observed in the three-dimensional full-field simulations are described accurately by this coupled oscillator model. Our results show that the strong coupling between the incident light, the resonant nanoparticles, and the silver surface results in mode anti-crossing behavior and a *reduced* surface plasmon coupling efficiency when the individual particle and surface resonance frequencies are approximately equal. Implications for the design of field enhancement structures and surface plasmon couplers are discussed. The work discussed in this chapter was published in the Journal of Applied Physics.[65]

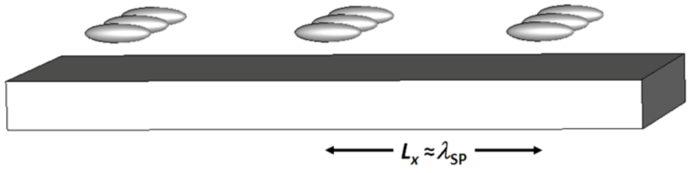

Figure 2.1. A schematic of a section of an infinite array of ellipsoidal silver nanoparticles, embedded in silica, and above an extended silver film.

2.2 Simulation Parameters

The structure under investigation consists of an array of ellipsoidal silver nanoparticles placed in close proximity to a silver surface. The electromagnetic response of the system was studied using the Finite Integration Technique (FIT)[66] as implemented in CST Microwave Studio[64]. A schematic of the simulation volume is shown in Figure 2.2. The system consists of a 200 nm thick silver film extended infinitely in the x-y plane, embedded in SiO_2. The silver film thickness is chosen to prevent measurable coupling of surface plasmon amplitude from the top to the bottom surface of the film. An ellipsoidal silver nanoparticle of semi-axes $a\times b\times c$ along the x, y, and z-directions respectively is located in the SiO_2 with the center of the nanoparticle placed 80 nm above the metal surface. The particle aspect ratio AR = a/c with $a = b$ was varied between 2 and 4 while keeping the particle volume fixed and equal to the volume of a 30 nm diameter spherical nanoparticle. The particle volume was maintained constant to exclusively investigate shape related effects and to eliminate volume related changes in resonance frequency and amplitude. The system is excited at normal incidence using a plane wave polarized along the x-direction and travelling in the negative z-direction. Electric boundary conditions (tangential electric field components zero) were applied at $x = 0$ and at $x = L_x/2$, while magnetic boundary conditions (tangential magnetic field components zero) were applied at $y = 0$ and $y = L_y/2$. Here L_x and L_y are size parameters that describe the simulation geometry. Open boundary conditions were applied along the positive and negative z-directions. These boundary conditions effectively simulate an infinite array of nanoparticles with a longitudinal spacing of L_x and a lateral spacing of L_y above an infinitely extended silver film. The temporal dependence of the excitation signal was chosen to be a Gaussian modulated sine wave centered at a free-space wavelength of 676 nm

(4.35×10^{14} Hz) with a pulse duration of 16 fs. This corresponds to a wavelength range from 451 nm (6.65×10^{14} Hz) to 1357 nm (2.21×10^{14} Hz). The center wavelength was chosen to coincide with an experimentally available laser wavelength; however the trends observed in the simulations do not depend on the exact center wavelength chosen. For example, a similar particle based coupler can be designed at 850 nm, a standard short range optical communications wavelength. For the present study, the lateral particle spacing was chosen to be $L_y = 100$ nm, and the longitudinal inter-particle spacing was set to $L_x = 440$ nm. This spacing was chosen to coincide with the calculated Ag-SiO_2 surface plasmon wavelength at a free-space wavelength of 676 nm. The frequency dependent complex dielectric function of silver was described using a Drude model fit to available literature values[48]. The real part of the modeled permittivity differed from the experimental data[48] by less than six percent across the simulation bandwidth, while the imaginary part of the permittivity was set equal to the known literature value at the design frequency. Since the silver dielectric function deviates from the idealized Drude response, the imaginary part of the dielectric function differs from the literature values[48] by up to a factor 2 in the frequency range used. The dielectric constant of SiO_2 was set to a constant value of $\varepsilon_r = 2.21$ over the entire wavelength range of the simulation. Due to the high dielectric contrast in metallodielectric nanostructures, extremely small mesh sizes are required in order to ensure convergence.[44] In this study mesh cell sizes ranging from 1-4 nm were used near metal-dielectric interfaces. Mesh convergence tests showed that the resulting errors in the electric field magnitude and resonance frequency values in this work are ±2.5% and ±0.2% respectively.

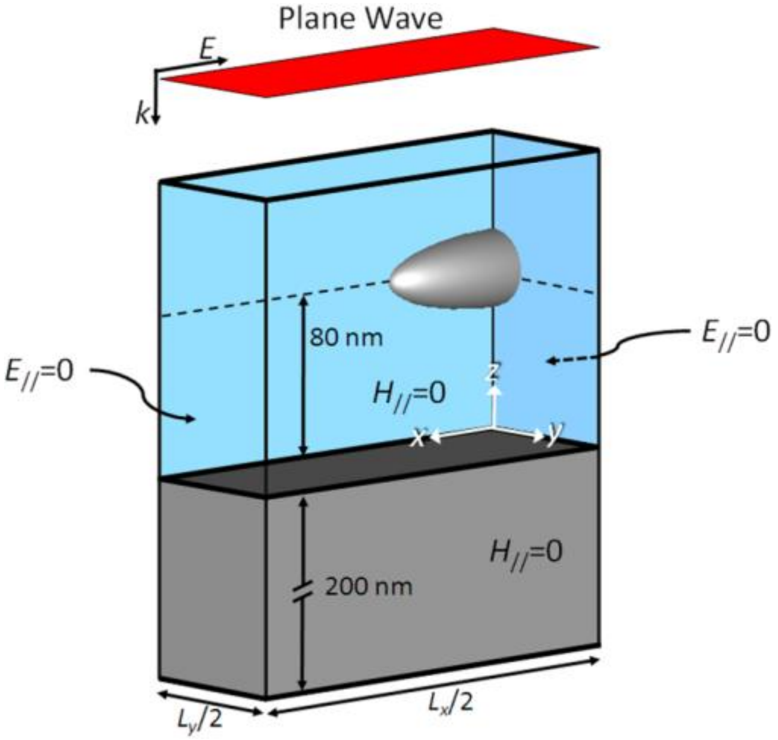

Figure 2.2. A schematic of the simulated plasmon excitation structure. Grey regions correspond to silver, and the blue regions correspond to silica.

2.3 Simulation Results

Figure 2.3 shows the distribution of the *x* and *z* components of the electric field (E_x and E_z) in the simulation volume at $y = 0$, for an ellipsoidal particle with an AR of 3.5 at time $t = 15$ fs, well after the illumination pulse has passed. Several important features are observed. First, note that E_z is maximum near the film surface at locations $x = -L_x/4$ and $x = +L_x/4$ (labeled location 1), and changes sign around the film surface. This is indicative of the presence of surface charge. At the metal surface the corresponding E_x amplitude is found to show a local maximum at $x = 0$ underneath the particle (labeled location 0) as well as at $-L_x/2$ and $L_x/2$. Both these observations point to the presence of surface plasmons. Second, the observed E_x and E_z

field distributions observed around the particle indicate a predominantly dipolar polarization of the particle. The charge distribution responsible for the observed fields at the film surface and near the particle is indicated schematically by the + and – signs in Figure 2.3.

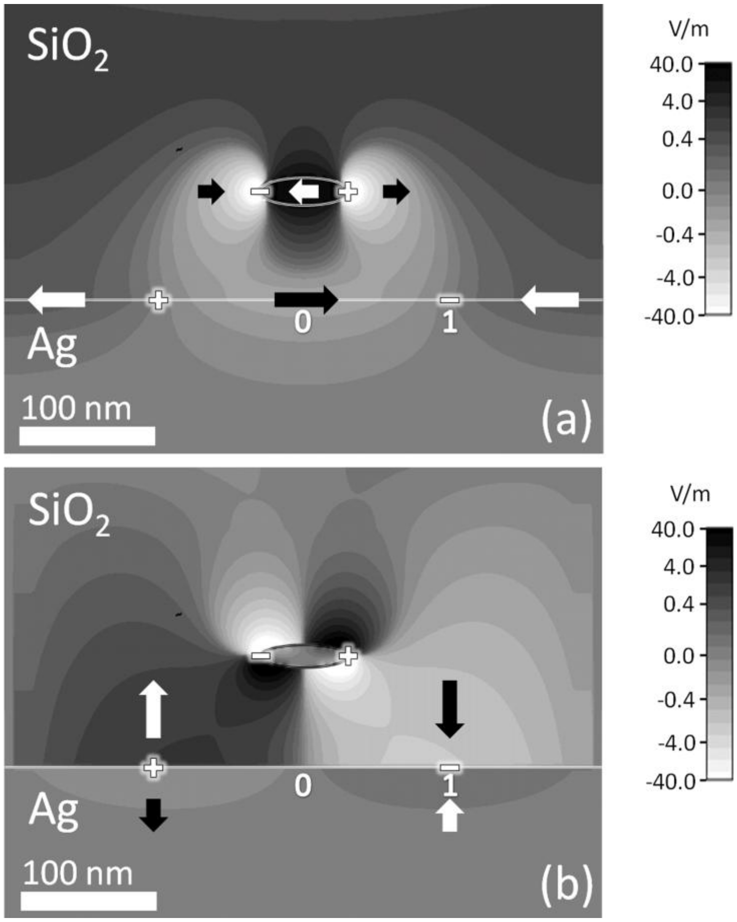

Figure 2.3. (a) $E_x(x,z)$ and (b) $E_z(x,z)$ fields at $y = 0$ at a frequency of 4.35×10^{14} Hz. The arrows indicate the direction of the field, and the location of the corresponding surface charges is indicated schematically.

In order to obtain a measure for the excited surface plasmon amplitude on the metal film, we monitor the E_z amplitude just above the metal film ($z = 1$ nm) at position 1. Note that at this position, the particle dipole field adds a finite E_z contribution. The time evolution of E_z at location 1 is shown in Figure 2.4(b). Although the excitation signal can be seen to end at time

0.016 ps in Figure 2.4(a), extended ringing of E_z is observed well after the excitation signal has passed, indicating the existence of electromagnetic resonances on the system. Note that the full FIT simulation extended for 0.75 ps in order to allow the energy in the system to decay to negligible levels (below -40dB of the maximum energy). Figure 2.5 displays the Fourier Transform of this time-domain signal, normalized to the Fourier Transform of the incident pulse. Two clear resonances with markedly different linewidth are observed. The narrow resonance at 4.35×10^{14} Hz lies close to the theoretical Ag-SiO_2 surface plasmon frequency for a surface plasmon that has a wavevector $k_{SP,x} = \frac{2\pi}{L_x} k_{SP,x} = \frac{2\pi}{L_x}$ which occurs at $f = 4.44\times10^{14}$ Hz based on the dielectric functions used. Consequently, this resonance is attributed to the constructive interference of surface plasmons excited along the *x*-direction by the nanoparticles. The full

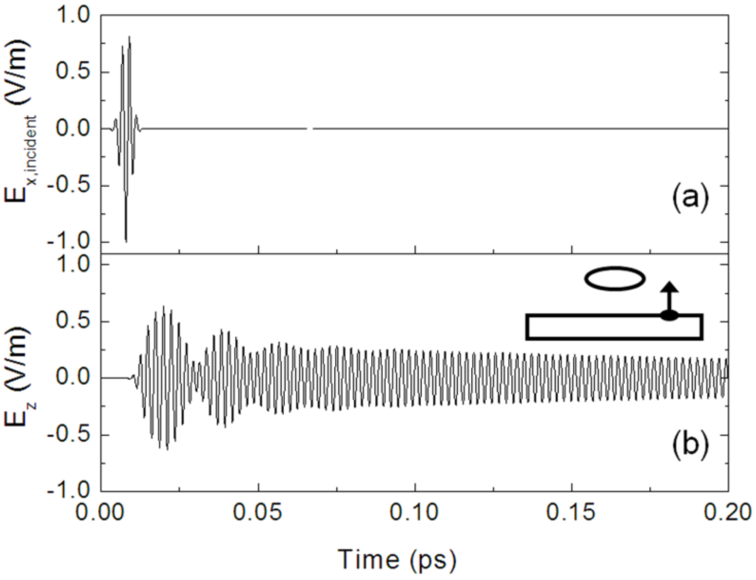

Figure 2.4. (a) Time dependence of the plane-wave excitation amplitude at the input of the simulation volume. (b) Time evolution of the E_z field at location 1 for a particle aspect ratio of 3.5.

width at half maximum of this resonance is found to be 2.0×10^{12} Hz. This sharp resonance will be referred to as the *film resonance* in this chapter. The broader resonance at 3.7×10^{14} Hz lies close to the analytically calculated nanoparticle resonance frequency of 3.81×10^{14} Hz for an isolated silver particle with an AR of 3.5 embedded in SiO_2. This resonance will be referred to as the *particle resonance* in this chapter. Note that since the signal shown in Figure 2.5 is normalized to the Fourier Transform of the excitation signal, field amplitudes larger than 1 are indicative of local field enhancement.

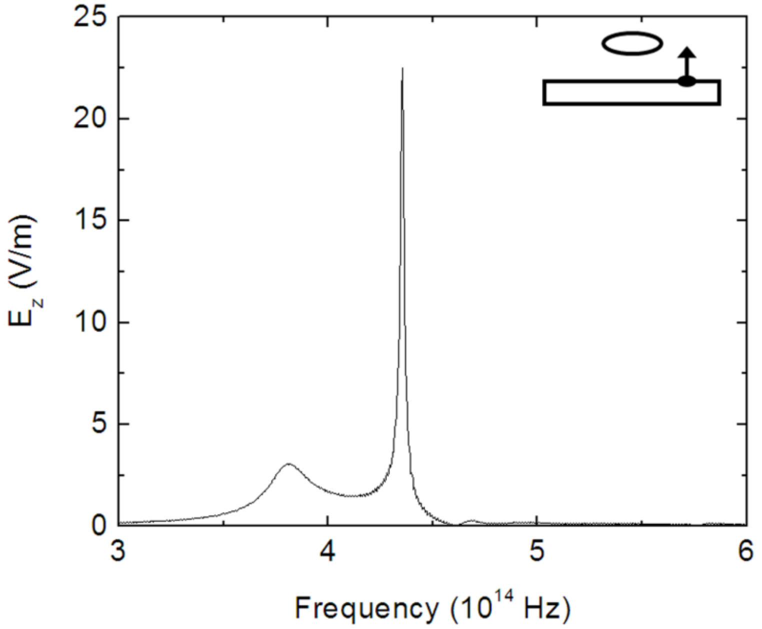

Figure 2.5. Fourier Transform of the time domain E_z signal observed at location 1 for a particle aspect ratio of 3.5.

To study the influence of the particle resonance frequency on the surface plasmon excitation, the calculation shown in Figure 2.5 was repeated for aspect ratios in the range of 2-4 (in steps of 0.1) corresponding to single particle resonance frequencies in the range 5.13×10^{14} Hz to 3.51×10^{14} Hz, as obtained by a separate set of FIT simulations. The resulting E_z magnitude at location 1 (predominantly surface plasmon related) as a function of frequency and particle aspect ratio is shown in Figure 2.6(a), with color representing field amplitude as indicated by the scale bar. The location of the silver-SiO_2 film resonance at 4.35×10^{14} Hz is indicated by the vertical dotted line. As the aspect ratio of the particle is increased from 2 to 4, the resonance frequency

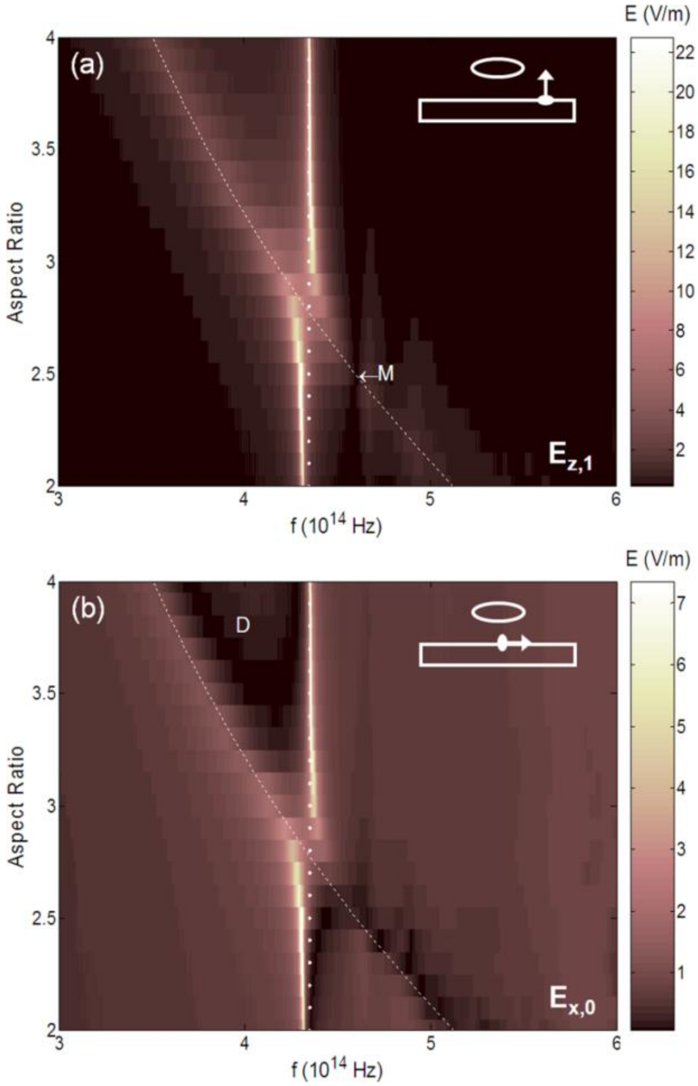

Figure 2.6. (color) Electric field magnitude (a) $|E_x(f)|$ at location 0, and (b) $|E_z(f)|$ at location 1, as obtained from the simulations, for particle aspect ratios in the range 2 to 4.

associated with the nanoparticle (broad feature) is seen to decrease from 5.4×10^{14} Hz to 3.6×10^{14} Hz. This is in correspondence with the expected response of an ellipsoidal particle excited with the electric field oriented along its long axis. For comparison, the dashed white line in Figure 2.5(a-b) and Figure 2.6(a-b) indicates the resonance frequency of an isolated Ag particle in SiO_2 calculated independently using FIT simulations. The observed FWHM of the particle resonance is found to be 3.0×10^{13} Hz, which is close to experimentally observed damping of approximately 6×10^{13} Hz for similarly sized silver nanoparticles.[67] As the particle resonance frequency approaches the film resonance at $\mathrm{AR} \approx 2.9$, a shift in the film resonance frequency as well as in the particle resonance frequency is observed. This shifting of resonances and the resulting anti-crossing is typical of strongly coupled resonant systems. Note that as a result of this strong coupling, the maximum field amplitude is *not* achieved when nanoparticle resonance and film resonance are identical. A final point of interest is the appearance of a field amplitude minimum (labeled M) at a frequency of 4.61×10^{14} Hz for all aspect ratios. Figure 2.6(b) shows the corresponding E_x field amplitudes obtained at location 0. The field at this location contains several field contributions: a contribution from the incident x-polarized wave, a contribution from the dipolar near-fields around the particle, a contribution due to the finite surface plasmon amplitude at the film surface, and fields due to any induced image charges. Similar trends are observed as in Figure 2.5(a), including a clear signature of the particle and film resonances, and evidence for anti-crossing. However notable differences are observed. For example, contrary to observations in Figure 2.5(a), an area of reduced field amplitude is seen at high AR values (dark area labeled D). In addition, a sharp minimum is observed in the E_x amplitude on the high frequency side of the film resonance. These differences will be discussed in greater detail in the *Discussion* section (section 2.5).

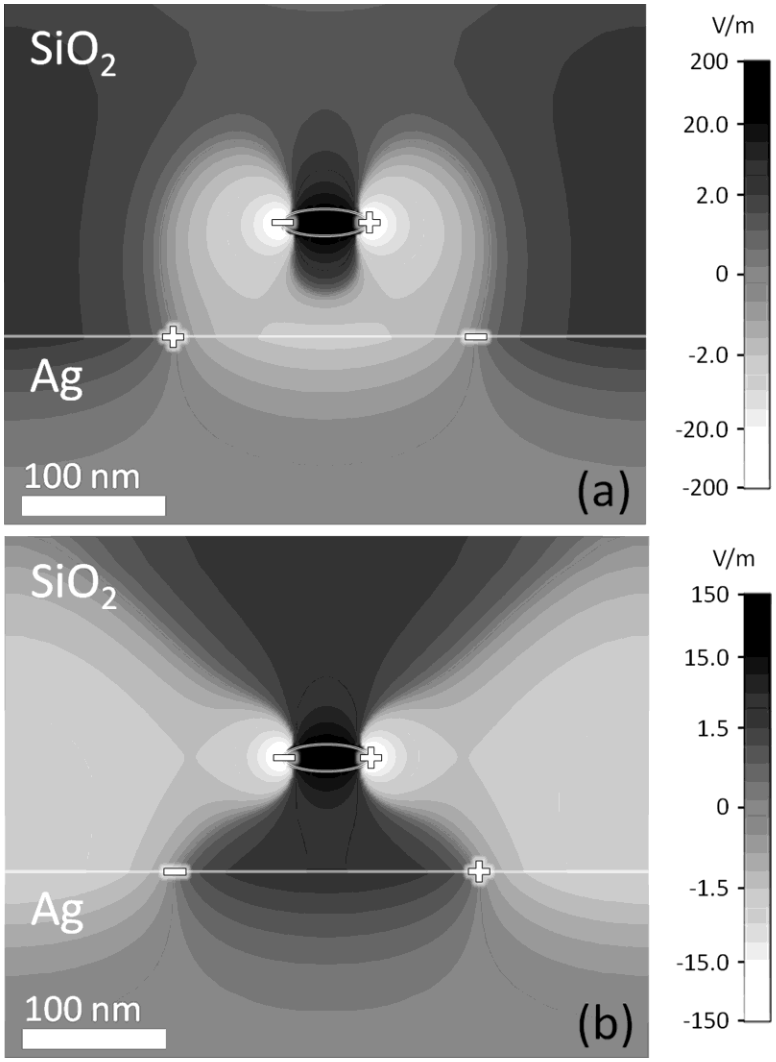

Figure 2.7. $E_x(x,z)$ eigenmodes at $y = 0$ at frequencies (a) 4.23×10^{14} Hz and (b) 4.38×10^{14} Hz at a particle aspect ratio of 2.9. The location of the corresponding charge distribution is indicated schematically.

Figure 2.6 shows that a particle AR of 2.9 leads to strong coupling and the appearance of two eigenmodes at different frequencies. In this strong coupling regime, the nanoparticle oscillation and the surface plasmon mode can no longer be considered independent resonances. Instead, two distinct eigenmodes exist. The nature of the eigenmodes is shown in Figure 2.7, which shows the spatial distribution E_x at a fixed phase at $y = 0$ for AR = 2.9 at frequencies

(a) 4.23×10^{14} Hz and (b) 4.38×10^{14} Hz respectively, corresponding to the two frequencies of maximum amplitude at this aspect ratio. The charge distribution associated with these field distributions is indicated schematically by the + and – signs. For the low energy mode at 4.23×10^{14} Hz shown in Figure 2.7(a), the charge displacement at the nanoparticle location and at the film surface are seen to be antiparallel, corresponding to an out-of-phase oscillation of the charges in the particle and the film. For the high frequency mode shown in Figure 2.7(b), the charge distribution of the nanoparticle and the surface plasmon are seen to be parallel, corresponding to in-phase oscillation of the charges. The observation of anti-crossing, the appearance of field minima at distinct frequencies, and the nature of the observed eigenmodes can be understood in terms of a coupled oscillator model as described below.

2.4 Coupled Oscillator Model

In order to gain insight into the origin of the features observed in Figure 2.5(a-b), we developed a coupled oscillator model of the nanoparticle enhanced coupler. In this model, the nanoparticle is modeled as a driven Lorentz oscillator with a resonance frequency f_p that is determined by the nanoparticle aspect ratio. The time dependent field amplitude at the particle center is given by $E_p(t)$. The surface plasmon related film resonance associated with the surface plasmon present at the Ag-SiO_2 interface occurs at a well defined frequency due to the periodic nature of the system, and is modeled as a Lorentz oscillator with a fixed resonant frequency f_f. The time dependent field amplitude at location 0 is given by $E_f(t)$. The nanoparticle oscillator is driven by the incident radiation with corresponding electric field contribution $E_{in}(t)$, as well as by any E_x contribution due to surface plasmons on the metal surface. Electric fields due to image charges are not considered in this calculation since, near the resonances of interest, we expect the resonantly excited fields to exceed the magnitude of image charge related fields. The resulting time dependent *x*-component of the electric field related to the polarization of the nanoparticle $E_p(t)$ is given by:

$$\frac{\partial^2 E_p(t)}{\partial t^2} + \Gamma_p \frac{\partial E_p(t)}{\partial t} + \omega_p^2 E_p(t) = -A\left[E_{in}(t) + C_{fp} E_f(t)\right] \qquad (2.1)$$

where Γ_p is the effective damping constant of the particle resonance including radiative damping, ω_p represents the resonance frequency of the nanoparticle in rad/s, the parameter A is a proportionality factor that depends on the particle resonance, and C_{fp} is a coupling constant ranging from 0 to 1 relating the surface plasmon field strength at the film surface to the field strength at the particle location. The magnitude of the parameter A can be estimated by realizing that at low frequencies, and neglecting any film contribution, the total field in the conductive nanoparticle tends to zero, or $E_p \approx -E_{in}$. In this low frequency limit the contributions of the differential terms in equation (2.1) become negligible, resulting in the relation $\omega_p^2 E_p \approx -A \times E_{in}$. Substituting $E_p \approx -E_{in}$ we find $A \approx \omega_p^2$. For the resonance frequencies considered here this leads to values for A that are of the order of 10^{31} s^{-2}.

The electric field associated with the surface plasmon mode at the metal film surface $E_f(t)$ (location 0) is driven exclusively by the E_x component of the field caused by the nanoparticle, and *not* directly by the incident radiation due to the large momentum mismatch of the incident light with the surface plasmon waves. The resulting lateral surface plasmon field amplitude at location 0 is described by the following equation:

$$\frac{\partial^2 E_f(t)}{\partial t^2} + \Gamma_f \frac{\partial E_f(t)}{\partial t} + \omega_f^2 E_f(t) = -B\left[C_{pf} E_p(t)\right] \tag{2.2}$$

where Γ_f is the effective damping constant of the surface plasmon mode in the film, ω_f represents the film resonance frequency in rad/s, C_{pf} again a scaling factor ranging from 0 to 1, here linking the nanoparticle field strength to the resulting surface plasmon driving strength. As was done for parameter A, the approximate magnitude of the constant B can be estimated by considering the low frequency limit. In this limit, we expect that fields at the film surface caused by the particle are approximately cancelled by the film response, or $C_{pf} E_p + E_f \approx 0$. Using this relation we find $B \approx \omega_f^2$. Since $f_f = 4.35\times10^{14}$ Hz, B is approximately of the order of 10^{31} s^{-2}. Note that this analysis does not take into account image charge.

Under harmonic excitation with $E_{in}(t) = E_{in}(\omega)e^{-i\omega t}$ $E_{in}(t) = E_{in} e^{-i\omega t}$ it follows that $E_p(t)$ and $E_f(t)$ are of the form $E_m(t) = E_m(\omega)e^{-i\omega t}$ $E_i(t) = E_i e^{-i\omega t}$ with m either p or f for particle and film respectively. Substituting these into equations (2.1) and (2.2) , and solving algebraically to obtain the film and particle field yields

$$E_f(\omega) = -BC_{pf} \frac{E_p(\omega)}{D_f(\omega)} \tag{2.3}$$

and

$$E_p(\omega) = -A\frac{E_{in}(\omega)}{D_p(\omega)}\left(1 - \frac{ABC_{pf}C_{fp}}{D_p(\omega)D_f(\omega)}\right)^{-1}, \tag{2.4}$$

where $D_m(\omega) = \omega_m^2 - \omega^2 - i\Gamma_m\omega$, with again m either p or f for particle or film respectively.

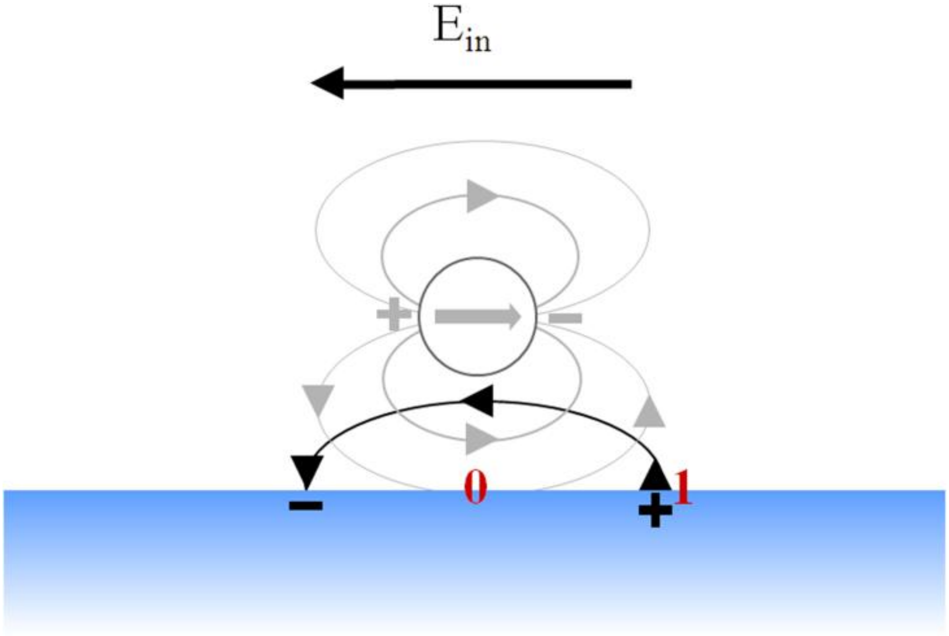

Figure 2.8. Relative orientation of electric field at low frequency excitation. Arrow on top represents direction of the incident field. Grey lines and arrows sketch fields of the polarized nanoparticle. Black lines and arrows sketch fields of the film interface.

To calculate the total field at the positions 0 and 1, we add the relevant contributions of $E_{in}(\omega)$, $E_p(\omega)$, and $E_f(\omega)$ with appropriate signs and scaling factors. To find the relative sign of these contributions we consider the low frequency limit. Figure 2.8 shows the relative field direction under low frequency excitation, and the corresponding charge distribution in the system. At location 0, the lateral components of $E_p(\omega)$ and $E_f(\omega)$ are opposite, which is accounted for in equations (2.1) and (2.2) by the negative sign associated with the parameters A and B. Therefore, the total lateral field at location 0 becomes $E_{sum,0} = p_0 E_{in} + q_0 E_p + r_0 E_f$, where p_0, q_0, and r_0 are all positive scaling factors of order 1 that relate the magnitudes of $E_{in}(\omega)$, $E_p(\omega)$, and $E_f(\omega)$ to their actual contribution at location 0. In contrast, Figure 2.8 shows that for the same low-frequency field distribution, the *z*-component of the surface plasmon related field at position 1 lies *along* the direction of the *z*-component of the particle related field. Thus, at location 1, the total normal field is described by $E_{sum,1} = p_1 E_{in}(\omega) + q_1 E_p(\omega) - r_1 E_f(\omega)$, where p_1, q_1, and r_1 are again positive scaling factors of order 1 that relate the magnitudes of $E_{in}(\omega)$, $E_p(\omega)$, and $E_f(\omega)$ to their actual contribution at location 1 $E_{sum,1} = p_1 E_{in} + q_1 E_p - r_1 E_f$. The values of the field scaling constants used are summarized in Table 2.1. The coupling constants were held fixed at $C_{pf} = C_{fp} = 0.15$, and the damping constants Γ_p and Γ_f were set to 1.7×10^{13} Hz and 9×10^{11} Hz respectively, to match the FWHM as found in the FIT simulations at AR = 3.5.

Table 2.1. Constants used in the coupled oscillator model to obtain the electric fields at locations 0 and 1.

Location	**E-field component**	***p***	***q***	***r***
0	*X*	1.0	0.1	1.0
1	*Z*	0	2.0	3.2

Figure 2.9(a-b) shows the calculated field magnitude using the coupled oscillator model using $A = 0.007\omega_p^2$ and $B = 0.011\omega_f^2$, and $f_f = 4.35\times10^{14}$ Hz. The particle resonance frequency was assumed to be identical to that calculated previously for an isolated Ag particle in SiO_2 as marked by the dashed line in Figure 2.6(a-b). Several features that were observed in the full-field simulation results are reproduced by the calculations based on the coupled oscillator model. With the above parameters, the anti-crossing between the particle resonance and the film resonance observed in Figure 2.5(a-b) is reproduced faithfully in Figure 2.6(a-b). Additionally, the

minimum labeled *M* in Figure 2.6(a) is reproduced using the coupled oscillator model (labeled *M'* in Figure 2.9(a)). The following section discusses the various features observed in Figure 2.5(a-b) and Figure 2.6(a-b).

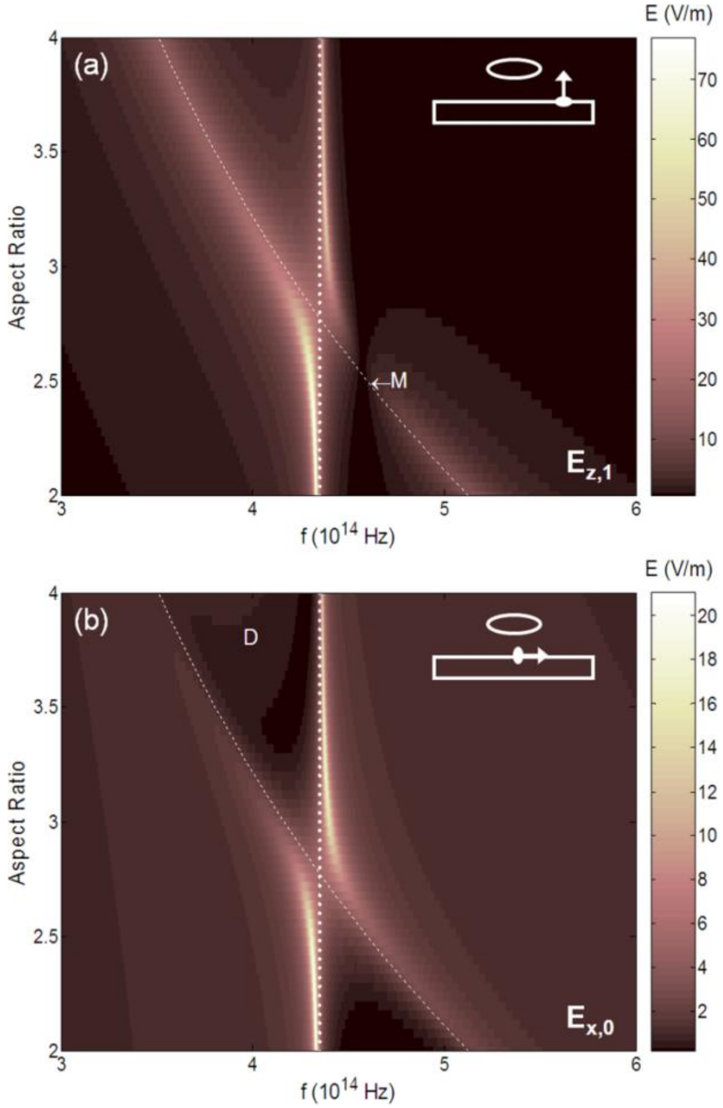

Figure 2.9. (color) Electric field magnitude (a) $|E_x(f)|$ at location 0, and (b) $|E_z(f)|$ at location 1, as calculated using the coupled oscillator model, for particle aspect ratios in the range 2 to 4.

2.5 Discussion

The coupled oscillator model was shown to reproduce several of the features that were observed in the numerical simulations. This allows us to gain insight into the physical origin of these features. In the following we discuss the origin of the anti-crossing, the nature of the sharp minimum in the electric field amplitude above the film resonance frequency, and the origin of the reduced lateral field amplitude at frequencies between the particle and film resonances.

We first consider the observed anti-crossing. To understand the nature of the eigenmodes that appear at the aspect ratio where anti-crossing is observed, we compare the field amplitudes $E_f(\omega)$ and $E_p(\omega)$ at an aspect ratio of AR = 2.9. As seen in Figure 2.9(a), this aspect ratio leads to low-frequency and high-frequency peaks of total field amplitude at $f_\mathrm{L} = 4.24\times10^{14}$ Hz and $f_\mathrm{H} = 4.46\times10^{14}$ Hz respectively. From equations (2.3) and (2.4) , we can now calculate the relative amplitude of the particle field and the film field. In the low frequency case a particle field amplitude of $E_p(\omega) = +3.21$ V/m and a film field amplitude of $E_f(\omega) = -4.32$ V/m are obtained, indicating anti-parallel alignment of the fields. Conversely, in the high frequency case a particle field amplitude of $E_p(\omega) = +3.09$ V/m and a film field amplitude of $E_f(\omega) = +3.79$ V/m are obtained, indicating parallel alignment of the fields. These anti-parallel and parallel field orientations correspond to anti-parallel and parallel charge displacement in the particle and film, which agrees well with the eigenmodes obtained using the full field simulations, as shown in Figure 2.7.

The observed minimum in E_x (labeled *M* in Figure 2.5(a)) can be understood in terms of the magnitude and phase of the particle and surface plasmon field contributions. Since the nanoparticle provides the only driving force of surface plasmons on the metal film, outside the strong coupling regime the phase of the surface plasmon fields at the film surface approximately follows the behavior of a simple damped driven harmonic oscillator. As a result, the surface plasmon response at the film surface experiences a phase lag relative to the phase of the particle field that varies from ~90° under excitation near f_f to ~180° when the film is excited well above its resonance frequency. Thus, at frequencies above f_f a condition exists in which the E_z contribution at location 1 by the film is similar in magnitude and *opposite in sign* to that introduced by the nanoparticle. This results in the observed minimum of the total $E_{sum,1}(\omega)$ field at 4.55×10^{14} Hz. Since the nanoparticle drives the charge oscillation in the film, the magnitude of the surface plasmon related field at any frequency is directly proportional to the particle field magnitude at that frequency. Thus the frequency at which cancellation occurs is independent of the specific nanoparticle resonance frequency, as observed near the frequency marked by *M* and *M'* in Figure 2.5(a) and Figure 2.6(a).

The region of low field magnitude for frequencies labeled *D* in Figure 2.6(b) is also reproduced by the coupled oscillator model, and is labeled *D'* in Figure 2.9(b). This minimum can be understood in terms of the phase and amplitude of the particle field, the excitation signal, and the surface plasmon field. At frequencies above the particle resonance, the lateral field contribution associated with the particle response is finite and approximately *in phase* with the incident field. If these frequencies lie below the resonance frequency of the film, a small surface plasmon amplitude is excited in the film that opposes the particle field. This film response therefore partially cancels the particle field and the incident field near the surface, resulting in the low field amplitude observed in the region labeled *D*. Note that in the FIT simulations the film response can include contributions from image charges, while in the coupled oscillator model the film response is limited to surface plasmon contributions to the field.

A final observation reproduced by the coupled oscillator model is the appearance of reduced surface plasmon amplitude when the single particle resonance frequency and the film resonance frequency are approximately equal, which leads to the observed anti-crossing. This can now be understood in terms of the relative damping of the surface plasmon oscillations on the film and on the nanoparticle. Due to the fact that the damping constant for the dipolar particle resonance is a factor ~20 larger than that of the surface plasmons on the Ag film, the largest surface plasmon field amplitude is achieved at relatively small field amplitudes in the particle. In this particular geometry, this occurs at frequencies well away from the particle resonance. These observations have implications for the use of resonant nanoparticles for surface plasmon excitation in finite size arrays.

The effective damping of surface plasmons on the silver film can be expected to increase for smaller array sizes as a result of surface plasmons propagating away from the array. Based on the previous analysis we expect that for smaller arrays the optimum surface plasmon amplitude will be reached using a small number of strongly coupled scatterers, while for large arrays the highest surface plasmon field strength will be observed using weakly coupled low-loss scatterers. The remaining chapters in this thesis will investigate the dependence of the surface plasmon excitation efficiency on array size, and particle size.

Finally, it should be noted that although the coupled oscillator model presented here reproduces many of the features observed in the full-field simulations, it does not take the place of *ab-initio* calculations. The strength of the full-field calculations lies in the fact that coupling constants and effective damping constants do not need to be determined independently. The coupled oscillator model on the other hand provides a physical interpretation of the observed features, and additionally enables the rapid evaluation of the surface plasmon excitation efficiency for a wide range of geometries by tuning the various parameters.

2.6 Conclusions

Numerical simulations of a nanoparticle-enhanced plasmon excitation structure consisting of ellipsoidal Ag nanoparticles in close proximity to a Ag-SiO_2 interface were presented. It was shown that varying the nanoparticle geometry enables control over the frequency dependent surface plasmon excitation efficiency. Strong coupling between the particle resonance and the film resonance associated with surface plasmons on the silver film was observed as evidenced by anti-crossing of the particle and film resonances. It was observed that for the infinitely extended structures simulated here the maximum field amplitude is *not* achieved when the particle resonance frequency and film resonance frequency are matched. These observations were reproduced using a coupled oscillator model, and explained in terms of a balance between nanoparticle induced damping and intrinsic surface plasmon damping at the Ag-SiO_2 interface. Based on our observations, the optimum geometry for coupling is expected to depend on intrinsic and geometry related damping mechanisms.

3 EFFECT OF PARTICLE-INDUCED DAMPING ON THE EXCITATION OF PROPAGATING SURFACE PLASMONS

3.1 Introduction

In Chapter 2 we theoretically and numerically studied surface plasmon (SP) excitation on a silver film using a nanoparticle enhanced grating coupler, and demonstrated strong coupling between the localized nanoparticle (NP) plasmon resonance and a grating resonance associated with the periodic particle arrangement. While those simulations were carried out for a fixed nanoparticle volume, it is expected that the surface plasmon excitation efficiency can be controlled by independently varying the nanoparticle volume.

In this chapter the excitation of propagating surface plasmons (SPs) on a silver-SiO_2 interface by an array of ellipsoidal silver nanoparticles is investigated using numerical simulations as a function of particle volume for three different nanoparticle aspect ratios. We find that while the surface plasmon amplitude depends sensitively on particle volume for each selected aspect ratio, the maximum surface plasmon amplitude obtained for the different particle shapes is remarkably similar. These observations are explained in terms of particle-mediated surface plasmon excitation, counteracted by a size dependent particle-induced damping. An analytical model is presented that quantitatively describes the observed trends in surface plasmon damping. The work discussed in this chapter was published in Applied Physics Letters.[68]

3.2 Simulation Structure

The structure under investigation is similar to that used in Chapter 2, and consists of an array of ellipsoidal silver nanoparticles placed in close proximity to a silver surface, as shown in

Figure 3.1. The system was studied using the Finite Integration Technique (FIT)[66] as implemented in CST Microwave Studio[69]. The silver film is 200 nm thick and extended infinitely in the *x*-*y* plane, embedded in SiO_2. The film thickness is chosen to prevent measurable coupling of surface plasmon amplitude from the top to the bottom surface of the film. The surface of the film corresponds to location $z = 0$. An ellipsoidal silver nanoparticle of semi-axes $a \times b \times c$ along the *x*, *y*, and *z*-directions respectively is located in the SiO_2 with the center of the nanoparticle placed 80 nm above the metal surface. The particle aspect ratio (AR) is defined as a/b, and for all particles the cross-section is circular, i.e. $c = b$. The system is excited at normal incidence using a plane wave polarized along the *x*-direction and travelling in the negative *z*-direction. Under these conditions, standing surface plasmon waves can be excited on the surface of the metal, as discussed in Chapter 2. The excitation signal was a Gaussian modulated sine wave centered at a free-space wavelength of 676 nm (2.73×10^{15} rad/s) with a pulse duration of 9.5 fs corresponding to a wavelength range from 27 nm (6.9×10^{14} rad/s) to 386 nm

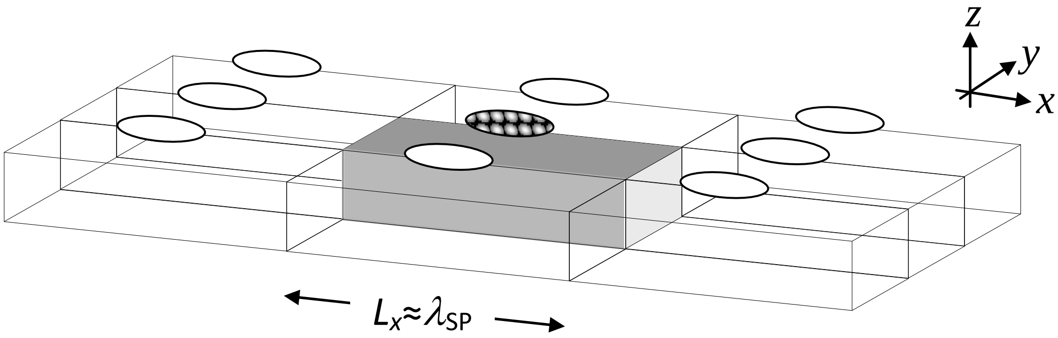

Figure 3.1. Schematic of the simulated plasmon excitation structure, showing nine unit cells of the periodic structure. The silver nanoparticles are embedded in SiO_2 and suspended 80 nm above a silver surface.

(8.87×10^{15} rad/s). Based on symmetry, tangential electric field components were set equal to zero at $x = 0$ and at $x = L_x/2$, while tangential magnetic field components were set to zero at $y = 0$ and $y = L_y/2$. Here L_x and L_y are size parameters that describe the x and y-spacing of the nanoparticles. These boundary conditions effectively simulate an infinite array of nanoparticles with a longitudinal spacing of L_x (set to 440 nm) and a lateral spacing of L_y (set to 100 nm) above an infinitely extended silver film. The longitudinal inter-particle spacing $L_x = 440$ nm, was chosen to coincide with the calculated Ag-SiO_2 surface plasmon wavelength at a free-space wavelength of 676 nm. The frequency dependent complex dielectric function of silver was described using a Drude model fit to known literature values[48], as described in detail in Chapter 2. The dielectric constant of SiO_2 was set to a constant value of $\epsilon_r = 2.21$ over the entire wavelength range of the simulation. Due to the high dielectric contrast in metallodielectric nanostructures, mesh sizes of 1-4 nm are required in order to ensure convergence.[44]

3.3 Simulation Results

To monitor the excited surface plasmon amplitude on the metal film, a probe is used that monitors the E_z amplitude just above the metal surface at position ($L_x/4$, 0, 1 nm) coinciding with the location where the E_z amplitude of the standing surface plasmon wave is maximum, as described in details in reference Chapter 2.

Figure 3.2(a) displays the Fourier transform of the time-domain signal at the probe location, normalized to the Fourier transform of the incident pulse, for a particle with aspect ratio 3.5 and volume equal to 9.8×10^3 nm^3. Two clear resonances with markedly different linewidth are observed that have been previously attributed to resonances related to propagating surface plasmons constructively excited due to the periodicity of the array (sharp resonance at 2.73×10^{15}

rad/s), and surface plasmons excited at frequencies close to the Mie resonance of the nanoparticles (broad resonance at 2.32×10^{15} rad/s). These two features will be referred to respectively as the *grating resonance* (previously called *film resonance* in Chapter 2), and the *particle resonance*. Note that for this particular particle aspect ratio, the particle resonance frequency is lower than the grating resonance frequency as marked by the dashed and solid vertical lines respectively. Figure 3.2(b) and Figure 3.2(c) show the corresponding results obtained for particles with the same volume, but with an aspect ratio of 2.9 and 2.5 respectively.

For AR = 2.9 the isolated particle resonance frequency can be seen to lie very close to the

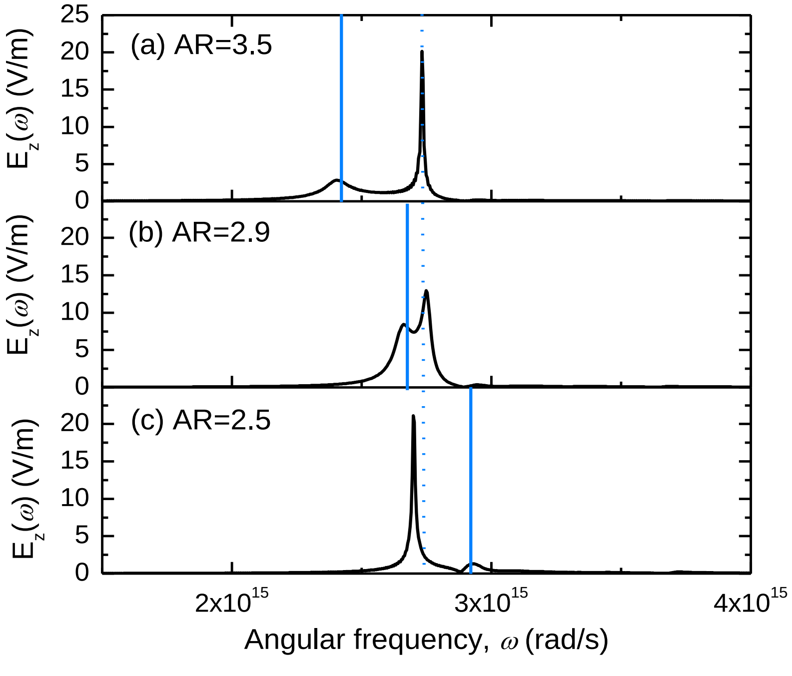

Figure 3.2. Electric field magnitude $|E_z(\omega)|$ at the probe location, for (a) AR = 3.5, (b) AR = 2.9, and (c) AR = 2.5, for a nanoparticle volume of 9.8×10^4 nm^3. The solid line indicates the isolated nanoparticle resonance, and the vertical dashed line marks the grating resonance.

grating resonance, while for AR = 2.5 the isolated particle resonance frequency of lies well above the grating resonance frequency. Chapter 2 has shown that strong coupling between the particle resonance and the grating resonance leads to anti-crossing of the resonances.

To study the influence of the particle volume on the surface plasmon excitation, the calculations shown in Figure 3.2(a)-(c) were repeated for several particle volumes in the range 1.4×10^3 nm^3 – 4.2×10^4 nm^3 where the volume was varied linearly in steps of 1.4×10^3 nm^3. The maximum electric field amplitude and the full-width-half-maximum (FWHM) of the grating

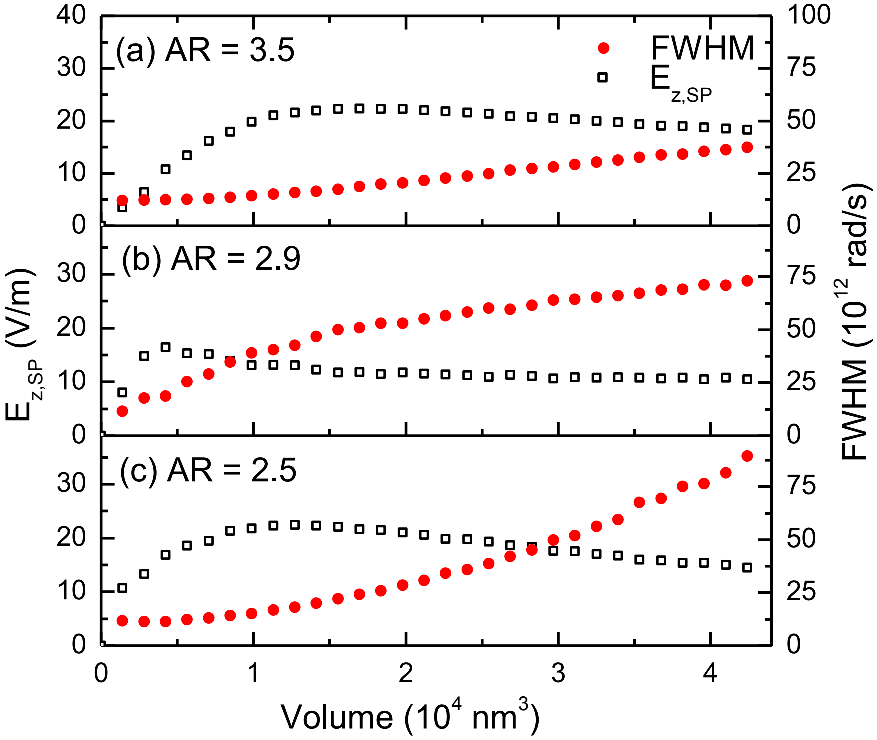

Figure 3.3. Peak electric field amplitudes of the grating resonance (filled squares) and the FWHM of the grating resonance (open circles) as a function of nanoparticle volume for nanoparticle aspect ratios (a) 3.5, (b) 2.9, and (c) 2.5.

resonance peak were obtained for all three particle shapes by performing a two-peak Lorentz fit for the data obtained from the simulations. It should be pointed out that in the strong coupling regime for an aspect ratio of 2.5, the two resonances can no longer be exclusively attributed to either particle or grating related resonances. For this aspect ratio, the narrow peak closest to the grating resonance (dashed vertical line in Figure 3.2(c)) was selected as being most representative of the grating resonance.

Figure 3.3 shows the calculated maximum electric field amplitude (filled squares) and the fitted FWHM (open circles) for the grating resonance as a function of particle volume for the three particle aspect ratios. Figure 3.3(a) shows the results obtained for particles with an aspect ratio of 3.5. Two distinct regimes can be observed. In the small particle limit, the FWHM of the grating resonance is seen to be approximately constant – and seen to increase approximately linearly with particle volume. At high particle volume ($V > \sim 1.5\times10^4$ nm^3) the surface plasmon amplitude is found to decrease slowly as the particle volume is increased, while the FWHM increases significantly. At the transition between these two regimes, a maximum surface plasmon amplitude of 22 V/m is obtained at a volume $V \approx 1.5\times10^4$ nm^3. Similar trends are observed for aspect ratios of 2.9 and 2.5 (Figure 3.3(b) and Figure 3.3(c)) with the peak electric field amplitude reaching a maximum value at a volume of $\sim 4\times10^3$ nm^3 and $\sim 1\times10^4$ nm^3 respectively. Note that in all three cases the maximum surface plasmon amplitude is reached at a volume close to the volume at which the FWHM starts to increases significantly. It should also be noted that in all cases the FWHM of the surface plasmon peak in the low-volume limit seems to approach a fixed value of $\sim 1.17\times10^{13}$ rad/s as the particle volume approaches zero. A final observation is that the maximum surface plasmon amplitude reached in the three cases is very similar, and approximately 20.3±3.3 V/m, despite the very different particle aspect ratio used. Perhaps surprisingly, these results suggest that the frequency of the nanoparticle surface plasmon resonance is not a critical parameter in the optimization of surface plasmon excitation in these nanoparticle enhanced grating couplers.

3.4 Analysis of Results using Calculated Nanoparticle-Induced Damping

In order to obtain further insight into the trends observed above, the nanoparticle induced surface plasmon damping is considered. While the nanoparticles are necessary to convert the incident far-field radiation into near-fields that can excite surface plasmons, they also introduce significant radiative and non-radiative damping. One could therefore expect that the optimum surface plasmon amplitude would be reached by increasing the volume to increase the optical absorption cross-section of the nanoparticles, while maintaining a sufficiently low particle volume to keep the particle induced radiative and non-radiative damping to an acceptable level. These assertions are discussed in more detail in the following.

To evaluate the effect of nanoparticle-induced damping on the maximum surface plasmon amplitude observed in Figure 3.3, we consider the various surface plasmon damping mechanisms. In the system under consideration, plasmon damping occurs due to (a) intrinsic resistive losses in the metal substrate, (b) non-radiative damping due to finite field-overlap of the surface plasmon modes on the substrate and the surface plasmon modes of the particles, resulting in particle induced resistive losses, and (c) radiative damping due to dipole radiation generated by the nanoparticle array due the necessary introduction of far-field to near-field coupling.

The intrinsic surface plasmon damping will be described in terms of a damping rate rather than in terms of a propagation length due to the extended nature of the excitation. The surface plasmon damping rate can be found by solving the plasmon dispersion relation in terms of a real wavevector and a complex frequency[1]. For a Ag-SiO_2 interface this leads to a damping constant $\Gamma_{\text{film}} = 4.7\times10^{12}\ \text{s}^{-1}$ at a free-space wavelength of 676 nm. This value represents the rate of dissipation of the electric field in the surface plasmon.

To evaluate the relative importance of particle related damping on the overall surface plasmon damping, we determine the radiative and non-radiative damping of localized surface plasmons on the nanoparticles. For this purpose we consider calculated Mie cross-sections, and convert these to an estimated damping rate. When an isolated nanoparticle is illuminated along one of its principal axes by a plane wave with electric field amplitude E, the total scattered (radiated) power is given by $P_{r,NP} = \sigma_r I = \frac{1}{2} n c \epsilon_0 E^2 \sigma_r$, where σ_r is the radiative Mie scattering cross-section for the incident electric field direction which can be easily obtained from the known dielectric functions, I is the incident irradiance, n is the refractive index of the host material, ϵ_0 is the permittivity of vacuum, and c is the speed of light in vacuum. In order to determine an approximate value for the particle-induced radiative damping we consider the local electric field E_{loc} at the location of the nanoparticle caused by the presence of surface plasmons on the metal film and make use of the provided relation between incident electric field and radiated power to estimate the particle induced damping. This assumes that the calculated cross-section of the particle remains approximately valid in the presence of the metal substrate. Although this assumption could lead to significant errors in the absolute value of the damping, it allows us to evaluate trends in the different damping contributions.

Under this assumption, we can now estimate the effective particle-induced radiative damping contribution. We can calculate the total electric field energy within a unit cell of volume V associated with the propagating surface plasmon, given by

$U(t) = \int_V \frac{1}{2}\epsilon_0\epsilon(\vec{r})E_{SP}^2(\vec{r},t)dV$. Here ϵ_0 is the permittivity of vacuum, $\epsilon(\vec{r})$ is the local permittivity (here either ϵ_{Ag} or ϵ_{SiO_2} depending on position), and $E_{SP}(\vec{r},t)$ is real the position-dependent electric field amplitude associated with a standing surface plasmon wave with a lateral wavevector $k_x = 2\pi/L_x$, and we assume that the decay of the field is slow compared to the fast phase variation at the time-scale of the optical cycle. Note that $E_{SP}(\vec{r},t)$ was calculated at a single wavelength (676 nm), and we assumed that the nanoparticle affects the electric field of the surface plasmon, and consequently the surface plasmon dispersion negligibly. Radiative damping will contribute to the total energy loss at a rate $\left(\frac{dU}{dt}\right)_{rad} = -2\Gamma_{r,np}U(t)$, where the factor 2 reflects the fact that the damping rates in this study represent electric field decay rates. As discussed above, the total damping of the surface plasmon per unit cell due to re-radiation by a single nanoparticle is approximately given by $\left(\frac{dU}{dt}\right)_{rad} = P_{r,NP} = -½nc\epsilon_0E_{\mathrm{loc}}^2\ \sigma_r$. For a given lateral electric field amplitude E_0 of the surface plasmon at the metal surface, we can obtain the local surface plasmon related driving field E_{loc} at the particle location from $E_{loc} = E_0e^{-k_zz_{np}}$ with k_z the known normal component of the surface plasmon wavevector, and $z_{np} = 80$ nm the height of the nanoparticle above the metal surface. This relation assumes that a single excitation frequency is used (here corresponding to free space wavelength of 676 nm), and that the nanoparticles do not significantly affect the surface plasmon dispersion relation. We now have expressions for the total energy in a unit cell, as well as for the scattered power within a single unit cell, all expressed in terms of E_0 and σ_r. This in turn allows us to calculate the effective radiative damping rate according to $\Gamma_{r,np} = P_r/2U$. An analogous analysis can be done to obtain a similar approximate expression for the nanoparticle induced absorption, based on the non-radiative scattering cross-section σ_{nr}.

Using the analysis described above we calculated the intrinsic surface plasmon damping Γ_{film}, the nanoparticle-induced non-radiative contribution to the surface plasmon damping $\Gamma_{\mathrm{nr,np}}$, and the nanoparticle-induced radiative damping $\Gamma_{\mathrm{r,np}}$, all evaluated at a wavelength of 676 nm corresponding to the grating resonance. The cross-sections were calculated according to $\sigma_{nr} = k \cdot \mathrm{Im}[\alpha]$, and $\sigma_r = k^4/(6\pi)|\alpha|^2$, where $k = 2\pi n/\lambda$ and α is the complex polarizability calculated based on the Rayleigh-Gans theory[52] using the literature dielectric functions for SiO_2 and Ag[48]. This gives an analytical expression for the estimated particle-induced radiative and non-radiative damping: $\Gamma_{r,np} \approx \frac{nc\,\mathrm{e}^{-2k_{\mathrm{z}} z_{\mathrm{np}}}\ \sigma_{\mathrm{r}}}{2\int_V \epsilon(\vec{r})\left(E_{SP}^2(\vec{r},t)/E_0^2\right)dV}$ and $\Gamma_{nr,np} \approx \frac{nc\,\mathrm{e}^{-2k_{\mathrm{z}} z_{\mathrm{np}}}\ \sigma_{\mathrm{nr}}}{2\int_V \epsilon(\vec{r})\left(E_{SP}^2(\vec{r},t)/E_0^2\right)dV}$. Note that for a single metal-dielectric interface these represent entirely analytical expressions, providing a relatively simple way of predicting particle related loss contributions in this type of system.

Particle-induced damping contributions were evaluated for particles with aspect ratios 4.05, 3.38, and 2.97, corresponding to theoretical resonance frequencies that coincide with those observed in the numerical simulations shown in Figure 3.3. Relatively high aspect ratio values were needed to match the numerical results, since the Rayleigh-Gans theory[52] does not take into account finite particle size effects and particle-substrate interactions, both of which affect the particle resonance frequency. Figure 3.4 shows the calculated damping contributions, as well as the sum of all damping contributions as a function of particle volume for the three aspect ratios considered. Since the nanoparticles are the only source of radiative damping, the total radiative damping Γ_{r} (green dotted lines in Figure 3.4) is equal to $\Gamma_{\mathrm{r,np}}$. The total non-radiative damping (blue dashed lines in Figure 3.4) is given by $\Gamma_{\mathrm{nr}} = \Gamma_{\mathrm{nr,np}} + \Gamma_{\mathrm{film}}$. Figure 3.4(a) shows the calculated damping terms for AR = 4.05, corresponding to the case where the particle resonance frequency is lower than the grating resonance frequency. The non-radiative damping Γ_{nr} is seen to increase linearly with increasing particle volume. In the limit of zero particle volume, Γ_{nr} is seen to converge to the non-radiative damping in the metal film Γ_{film}. The linear increase of the non-radiative damping with particle volume follows from the linear relation between the absorption cross-section and the polarizability, which in turn depends linearly on particle volume. The radiative damping term is seen to increase quadratically with increasing particle volume, due to the quadratic relation between the radiative cross-section and the polarizability. At this aspect ratio, for volumes less than 2.1×10^4 nm^3 (marked by the vertical dashed line in Figure 3.4(a)), the non-radiative damping is found to be the dominant loss contribution, whereas for larger particle volumes the radiative damping quickly becomes dominant. The dependence of the FWHM predicted based on the calculated damping contributions mimics the observations made in the full field simulation results shown in Figure 3.3(a), suggesting that particle-induced damping is the cause of the increased FWHM of the grating resonance in Figure 3.3(a) at large volumes. Since the FWHM (units: rad/s) of a narrow Lorentzian resonance is equal to the numerical value of Γ (units: s^{-1}), we may compare the magnitude of the calculated Γ with the FWHM values in Figure 3.3. This comparison reveals that the approximate analytical calculations predict the correct order of magnitude for the FWHM, without the use of any free parameters.

Similar trends are observed for particle aspect ratios of 3.38 and 2.97. For these two cases the volume at which the radiative damping becomes dominant is 1.1×10^4 nm^3 and 1.7×10^4 nm^3 respectively (marked by vertical dashed lines in Figure 3.4(b) and Figure 3.4(c)). Note that for a particle aspect ratio of 3.38, corresponding to a particle resonance frequency close to the grating resonance frequency (Figure 3.4(b)), Γ_r becomes the dominant damping contribution at a relatively small volume. This can be understood by realizing that the damping of the grating resonance depends on the nanoparticle-induced damping *at the grating resonance frequency*. When the nanoparticle resonance is matched with the grating resonance, the particle has a large radiative and non-radiative cross-section (i.e. appears ‘optically large’), leading to strong particle induced damping at relatively low volume.

The presented model also predicts that for all three particle aspect ratios the total damping will converge to the non-radiative damping in the metal film Γ_{film} in the limit of zero particle volume. The results from the numerical simulations in Figure 3.3 show a very similar behavior in the zero particle volume limit, converging to a FWHM of approximately $(1.17\pm0.28)\times10^{13}$ rad/s for small particle volume as noted before. We therefore conclude that the damping at low-particle volume is limited by the intrinsic damping in the metal film, which is governed only by the optical properties of the materials being used at the frequency under consideration.

While the model calculations accurately predict the trends observed in Figure 3.3(a) and Figure 3.3(c), the volume-dependent FWHM in Figure 3.3(b) differs significantly from the corresponding calculated damping curve in Figure 3.4(b) for particles with a resonance close to the grating resonance frequency. At low volume the simulated FWHM follows a similar increase as the corresponding calculations in Figure 3.4(b), but rapidly diverges from the simulation FWHM above the volume of 1.0×10^4 nm^3. Above this volume the calculated particle radiative cross-section exceeds the size of the unit cell, as marked on the right axis vertical axis. We therefore attribute the deviation from the calculated curve in Figure 3.4(b) to the saturation of the radiative damping contribution.

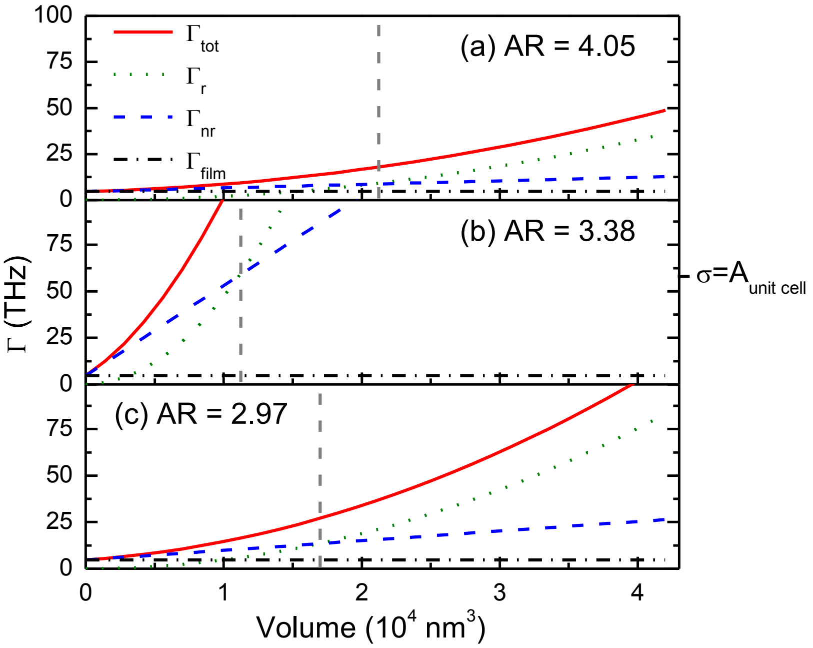

Figure 3.4. Calculated radiative and non-radiative damping contributions to the total surface plasmon damping for (a) AR = 4.05, (b) AR = 3.38, and (c) AR = 2.97. The dashed vertical lines indicate the condition $\Gamma_{nr} = \Gamma_r$.

3.5 Discussion

Based on the observations made above, we conclude that the appearance of a maximum in the surface plasmon amplitude occurs due to the combined effect of an increased excitation of surface plasmons as the particle volume increases, counter-acted by an increase in the particle-induced damping at increasing volume. This is in correspondence with the phenomenon of critical coupling of coupled resonators, for example in surface plasmon excitation using prism coupling[1] where maximum coupling occurs for the case when $\Gamma_r = \Gamma_{nr}$. In addition, we have found that tuning of the particle resonance frequency does not have a strong effect on the maximum attainable surface plasmon amplitude, but instead affects the particle volume at which this maximum amplitude occurs. From these results, it appears that control over the nanoparticle resonance frequency has no strong effect on the surface plasmon excitation efficiency if the particle volume can be freely modified. This has implications for the use of this type of coupled-resonance systems in biosensing applications such as Surface Enhanced Raman Scattering (SERS). While a change in the particle shape may have beneficial effects due the well-known antenna effect[70-72], the surface plasmon field strength is not necessarily enhanced by matching particle and film resonance frequencies. It should be stressed that the present simulations and calculations relate to the case of an infinite particle array, in which the intrinsic surface plasmon damping and the particle related damping terms make up all possible loss contributions. However, for finite size particle enhanced grating couplers, propagation of surface plasmons away from the array will introduce an additional non-radiative loss term. In this case, it is anticipated that the particle volume as well as the particle resonance frequency will need to be optimized in order to maximize the surface plasmon excitation efficiency. These assertions need to be tested in further theoretical and experimental studies.

3.6 Summary

In summary, we have studied the effect of particle-induced damping on the efficiency of surface plasmon excitation. The damping information obtained from simulations was compared to independently calculated nanoparticle contributions to the surface plasmon damping to obtain insight into the mechanism of the surface plasmon excitation. We found that the minimum surface plasmon damping in the system is limited by the intrinsic damping of the surface plasmon in the metal film, and the maximum damping of the surface plasmon was found to begin saturating at the volume of the nanoparticle at which the nanoparticle cross-section equals the area of the unit cell under consideration. The simulation results suggest that for infinite nanoparticle enhanced gratings, the resonance frequency of the nanoparticle surface plasmon is not a critical parameter in the optimization of surface plasmon excitation given free control over the particle volume. It was concluded that the maximum surface plasmon amplitude occurs due to the combined effect of an increased excitation of surface plasmons as the particle volume increases, counteracted by an increase in the particle-induced damping at large volumes.

4 EXPERIMENTAL OBSERVATION OF MODE-SELECTIVE ANTI-CROSSING IN SURFACE-PLASMON COUPLED METAL NANOPARTICLE ARRAYS

4.1 Introduction

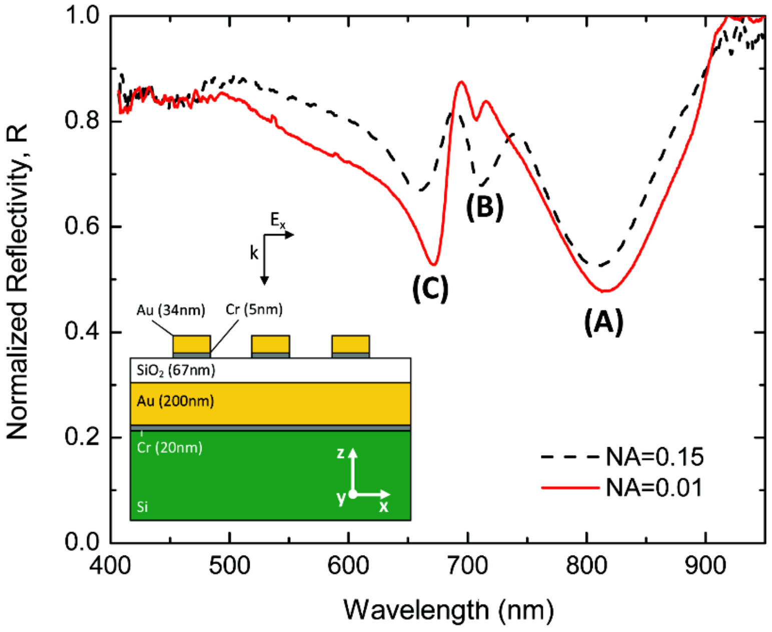

Figure 4.1. Normalized reflection spectra of a surface coupled nanoparticle array with longitudinal spacing L_x=565nm under two conditions: N.A.=0.15 (dashed line), and N.A.=0.01 (solid line). Inset: Schematic of the fabricated sample structure.

In Chapters 2 and 3 we investigated the use of silver nanoparticle arrays for the efficient excitation of surface plasmons (SPs) using compact silicon-compatible nanostructures, and showed that the interaction between nanoparticle resonances and surface plasmons in these arrays could lead to anticrossing.[65] The existence of such anticrossing has recently been demonstrated experimentally on particles arranged in a square lattice.[73] In the present study we investigate the excitation of surface plasmons using dense arrays of anisotropic gold nanoparticles on a thin SiO_2 layer near a gold film. We investigate the interaction between the plasmon resonance of the nanoparticles and the grating resonance of the periodic structures using geometry dependent reflection spectroscopy. In addition to the predicted anticrossing between particle and grating resonance resulting from strong coupling of the in-plane nanoparticle plasmon resonance and propagating plasmons at the Au-SiO_2 interface, we observe a second order mode as well as two additional modes not predicted by the numerical simulations in Chapter 2. Interestingly, the latter modes do not exhibit anticrossing in the entire observed frequency range. By comparing the experimental observations to the known surface plasmon dispersion relation we demonstrate that these observations can be understood in terms of a mode-selective anticrossing caused by the anisotropic nature of the metal nanoparticle polarizability. The work discussed in this chapter was published in Applied Physics Letters.[74]

4.2 *Sample Fabrication*

The sample consists of a gold film deposited on a Si substrate, with nanoparticle arrays fabricated on top of a silica spacer layer. A 20 nm Cr (purity 95%) adhesion layer was deposited onto the Si substrate, followed by thermal evaporation of 200 nm of gold (gold shot, purity 99.999%, International Advanced Materials) using a BOC Edwards FL400 Thermal evaporator. Both metals were deposited at a rate of approximately 2 Å/s. Subsequently a 67 nm thick (as determined by visible ellipsometry) SiO_2 spacer layer was deposited at a rate of approximately 0.9 Å/s by plasma-enhanced chemical vapor deposition (chamber temperature of 250^{o}C, chamber pressure 1052 mTorr, SH_4 flow rate 401 sccm, and NO_2 flow rate 826 sccm, D.C. bias of 7 V, and RF power of 24 W), using a UnAxis PlasmaTherm 790 PECVD/RIE Reactor. Following the metal and silica depositions, nanoparticles were fabricated on the sample using electron-beam lithography. The electron-beam resist used for lithography was Polymethyl Methacrylate with a molecular weight of 495 a.m.u. and diluted in anisole to a molar concentration of 3% (495 PMMA A3, Micro-Chem). The sample was coated with PMMA at a speed of 4000 revolutions per minute (RPM) for 40 s. Subsequently the sample was soft-baked at atmospheric pressure at a temperature of 180^{o}C for 3 min, above the glass transition temperature, to drive off volatile chemicals and water, thus avoiding an inhomogeneous distribution of the fluids in the PMMA matrix. Driving off volatiles allows the PMMA to reach an energetically stable configuration, and allows good planarization of the PMMA layer.[75] Subsequently, the sample was exposed in a Leica EBPG 5000+ electron-beam lithography system, using a beam current of 1 nA and an accelerating voltage of 50 kV. Exposure doses ranged from 400 μC/cm^2 to 780 μC/cm^2, in steps of 80 μC/cm^2. The exposed sample was developed by static immersion in a standard developer (methyl-isobutyl-ketone (MIBK) and isopropyl alcohol (IPA) mixed at a volume ratio MIBK:IPA = 1:3) for 90 s to remove the exposed resist. After developing, the sample was rinsed in IPA for 10 s, and dried using pressurized dry nitrogen. The sample was subsequently treated in an oxygen plasma (using the previously mentioned PECVD/RIE system: (pressure 40 mTorr, He flow rate 10 sccm, O_2 flow rate 20 sccm, RF power 14 W, DC bias 101 V, at a rate of ~20 nm/min) for 20 s to remove any remaining resist in the exposed regions. To form isolated gold nanoparticles on the exposed regions of the SiO_2 layer, a 5 nm Cr adhesion layer was deposited, followed by 35 nm of gold using the Edwards FL400 thermal evaporator. Both metals were deposited at a rate of approximately 1 Å/s. To remove the undeveloped PMMA the sample was soaked overnight in methylene chloride, followed by a rinse with methylene chloride. This unusually long treatment was necessary to resolve previously observed de-lamination of the underlying metal and dielectric films during lift-off. After lift-off, gold nanoparticle arrays remain on the SiO$_2$ surface, along with marker structures included with the mask to identify array parameters.

A schematic of the final sample structure obtained after lift-off is shown in Figure 4.1 (inset). The nanoparticle dimensions along the x, y, and z directions were 125 nm, 50 nm, and 39 nm respectively. Several particle arrays were fabricated, each consisting of 40 periods in the longitudinal (x) and transverse (y) directions, with a constant transverse center-to-center spacing of L_y=270 nm and a longitudinal center-to-center spacing L_x between 505 nm and 1045 nm. A scanning electron microscopy (SEM) image of part of an array with AR = 2.5 and $\mathrm{L_x}$ = 655 nm is shown in Figure 4.2. The SEM image shows consistent spacing between the nanoparticles, and reasonably consistent particle shape, both of which indicate that the electron-beam lithography process provides the level of fabrication control required for these experiments.

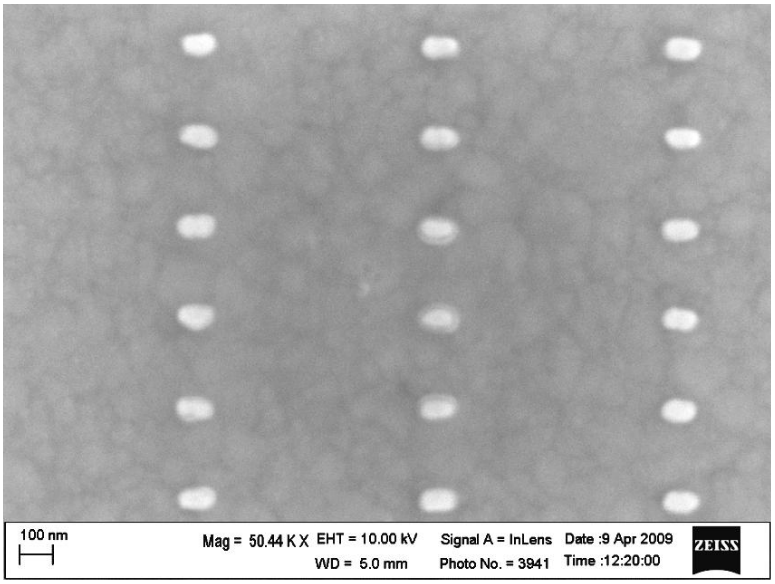

Figure 4.2. A scanning electron microscope image of a section of a nanoparticle array. The bright spots are gold nanoparticles.

Reflection spectra of the arrays were taken using an upright microscope. The sample was illuminated with a standard halogen light source through a 5× microscope objective. The incident light was polarized along the *x*-direction to within 10° using a fixed polarizer in the illumination path. The numerical aperture (N.A.) of the illumination was varied between a low N.A. of 0.01 and a high N.A. of 0.15 by varying the aperture stop of the microscope. The sample was held perpendicular to the optical axis of the microscope to within 0.004^o. For spectral analysis, the reflected light was directed to a multimode collection fiber with a core diameter of 50 μm, and sent to a single grating monochromator(Acton SpectraPro 2300i). Spectra were recorded using a thermoelectrically cooled silicon CCD camera attached to the monochromator at a sensor temperature of 195 K. The integration time was adjusted to prevent signal saturation, and resulting spectra were averaged to improve the signal to noise ratio. For each measurement, an array was aligned with the collection area of the fiber and the signal $S(\lambda)$ was recorded as a function of wavelength λ. A reference spectrum $S_{ref}(\lambda)$ was taken by measuring the reflectivity of a nearby region without nanoparticles, and a dark spectrum $S_{dark}(\lambda)$ was also recorded. The normalized reflectivity R was calculated as $R=(S–S_{dark})/(S_{ref}–S_{dark})$ and thus represents a change in reflectivity of the surface due to the presence of the periodic array. The spectral resolution in the measurements was approximately 4 nm.

4.3 Experimental Results

Figure 4.1 shows the reflection spectrum of an array with a longitudinal center-to-center spacing L_x=565 nm recorded with a relatively high numerical aperture of 0.15 (dashed line). At this grating spacing constructive plasmon excitation is predicted to occur at a free space wavelength of λ=685 nm, based on the known layer thicknesses, Au dielectric function from literature[48], and measured SiO_2 dielectric function. A pronounced reflection minimum (A) is observed at 810 nm. This feature corresponds to the individual nanoparticle plasmon resonance for excitation with light polarized along the x-direction, as confirmed in independent measurements in which the particle aspect ratio was varied (not shown). Two additional reflection minima are observed at $\lambda \approx 660$ nm and $\lambda \approx 710$ nm, close to the predicted free space wavelength of propagating surface plasmons if constructively excited by a grating of spacing L_x=565 nm. Upon reducing the illumination N.A. to 0.01 (solid line) the depth of the reflection minimum related to the particle resonance changes by only 8%, while the depth of the two remaining reflection dips varies more strongly by +22% and -19% respectively. Since lowering the N.A. reduces the relative contribution of vertically polarized light, it appears that the reflection minimum at 710 nm (B) is related to a propagating surface plasmon grating mode excited by the z-polarization of the nanoparticles, while the minimum (C) at 660 nm is a grating resonance excited by the x-polarization of the nanoparticles.

Reflection spectra similar to those shown in Figure 4.1 were taken at N.A.=0.01 for 19 different values of the longitudinal inter-particle spacing L_x from 505 nm to 1045 nm in steps of 30 nm. Figure 4.3 shows the measured normalized reflectivity, with dark regions corresponding to low reflectivity. For the smallest grating spacing (L_x=505 nm), the spectrum observed is similar to the low N.A. spectrum presented in Figure 4.1. Two main minima at approximately 630 nm and 800 nm are observed (open circles), corresponding to the grating resonance and the x-polarization related particle resonance respectively. As the spacing L_x is increased, the grating resonance is initially seen to red-shift, and for large grating spacing (L_x>800 nm) converges to the particle resonance frequency. The particle resonance on the other hand is initially independent of grating spacing, but red-shifts at grating spacing values L_x>600 nm. This pronounced anticrossing is due to the strong interaction of surface plasmon modes and the particle resonance, as predicted in simulations and discussed in detail in Ref. [65]. Very different trends are observed for the weak resonance attributed to *z*-polarized excitation (open triangles). As L_x is increased the weak reflection minimum gradually red-shifts, with no discernible anticrossing at frequencies close to the particle resonance. Above L_x=805 nm, an additional reflection minimum appears at λ≈550 nm (filled circles) which red-shifts as the grating spacing continues to increase. Above L_x=955 nm, a final reflection feature becomes discernable (filled triangles) which also red-shifts for increasing grating spacing.

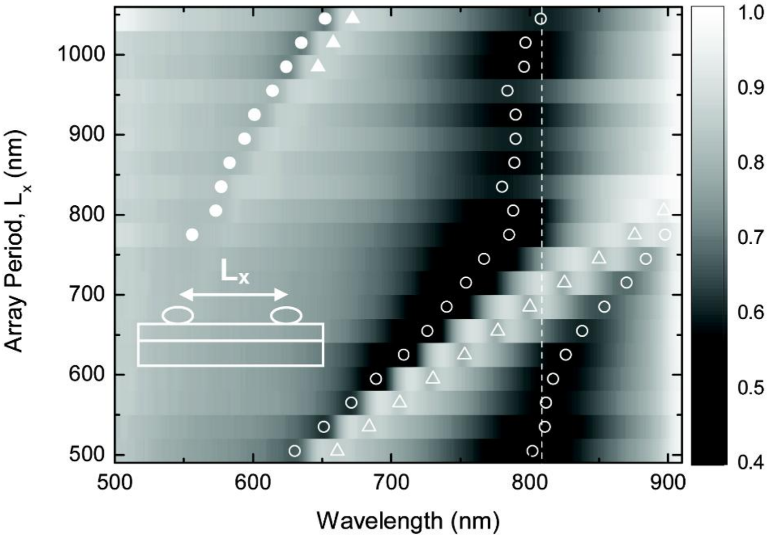

Figure 4.3. Geometry dependent reflection spectra of surface-coupled metal nanoparticle arrays as a function of longitudinal particle spacing L_x. The color scale represents normalized reflectivity. Symbols mark the positions of reflection minima. The lateral nanoparticle resonance wavelength is indicated by the dashed line.

4.4 Discussion and Analysis

To understand the experimental observations, we compare the location of the various reflection minima to the surface plasmon dispersion relation. Figure 4.4 shows the calculated surface plasmon dispersion relation for the air-silica-gold system in the absence of nanoparticles, calculated using the method developed by Ward[76] as a function of surface plasmon wavevector $k_x=k_{SP}$ using literature values for the Au optical properties[48] and measured values for the SiO_2 thickness and optical properties. Allowed low-loss surface modes appear as dark narrow lines, and the left and right bright lines correspond to the air and silica light-lines respectively. In order to excite propagating surface plasmons the grating equation needs to be satisfied, given by $k_{SP} = k_{//} \pm n \times G$ where $k_{//}$ is the wavevector component of incident light projected along the surface, $G=2\pi/L_x$ is the reciprocal grating vector of the structure, and n is an integer. Under normal incidence illumination with low N.A, we have $k_{//}\approx 0$, leading to the excitation condition $k_{SP}=G$ for $n=1$ (first order) and $k_{SP}=2G$ for $n=2$ (second order). The open symbols in Figure 4.4 show the angular frequency of the three prominent reflection minima observed in Figure 4.3 as a function of $k_x=G$. The weak reflection minima observed at $L_x>800$ nm are shown as a function of k_x=2G (filled symbols). Several features should be noted. First, the main reflection minima (open circles) clearly exhibit anticrossing. At frequencies away from the anticrossing region at $\lambda\approx 800$ nm, the location of the main reflection minimum is seen to converge to the calculated surface plasmon dispersion relation. In the region of anticrossing a large mismatch is observed between the positions of the reflection minima and the calculated surface plasmon dispersion relation, demonstrating that the large nanoparticle polarization near the particle resonance can strongly affect the surface plasmon dispersion relation in the array. Note that the high-frequency reflection minima (filled symbols) shown as a function of k_x=2G also lie very close to the calculated dispersion relation, demonstrating that these features

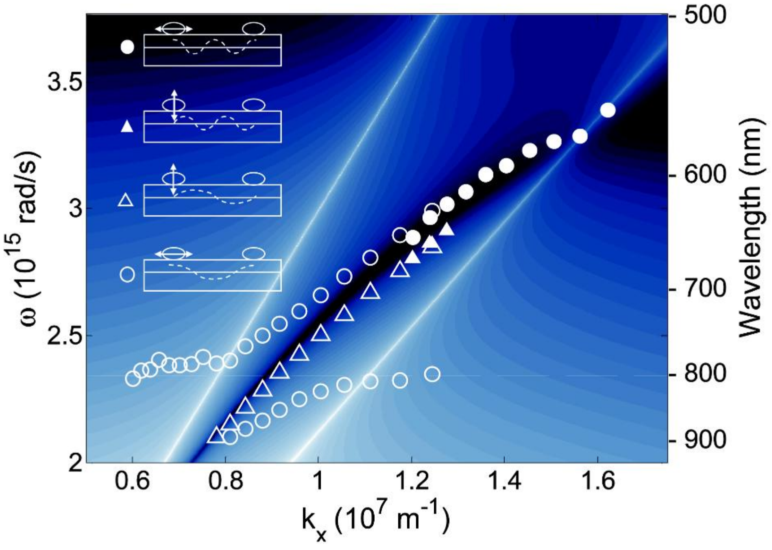

Figure 4.4. Calculated surface plasmon dispersion relation of the air-SiO$_2$-Au system. Experimentally observed reflection minima of the nanoparticle arrays are included as a function of k_x=G (open symbols) and k_x=2G (filled symbols). The corresponding modes are indicated schematically. The lateral nanoparticle resonance frequency is indicated by the dashed line.

correspond to the excitation of plasmon modes with a surface plasmon wavelength that is approximately half the inter-particle spacing.

Intriguingly, the weak reflection minima (open triangles) that were observed in Figure 4.3 are seen to almost exactly follow the calculated dispersion relation in Figure 4.4, without exhibiting any anticrossing near the nanoparticle resonance. This surprising result can be understood by considering the symmetry of the allowed modes. For near-normal incidence illumination the *x*-polarized incident field excites an *x*-polarized plasmon resonance in the nanoparticles. The interaction of the propagating surface plasmons with the strong *x*-polarized nanoparticle resonance gives rise to the anticrossing observed in Figure 4.4, as also observed in numerical simulations[65] and recent experimental work on square arrays of particles.[73] At finite N.A. values, the convergent nature of the incident light introduces a field contribution polarized normal to the sample surface. This leads to a weak vertical polarization of the nanoparticles that also produces surface plasmon excitation. In principle, this interaction could lead to strong particle- surface plasmon coupling and anticrossing. However, due to the anisotropic particle shape (aspect ratio ~2.5), the vertical particle resonance occurs at much higher frequency than the lateral particle resonance. As a result, any effects related to interaction with a vertical nanoparticle resonance are expected to occur at frequencies well above those investigated here and, in fact, above frequencies at which propagating surface plasmons can be excited in this material system. It is interesting to note that this vertically excited mode can act as an internal reference measurement, revealing the surface plasmon dispersion relation in the absence of strong particle-surface coupling. A final point worth noting is that the weak low-frequency second order (n=2) features (solid triangles) overlap with the first order (n=1) mode (open triangles) excited by vertical polarization, suggesting that these are also related to vertical polarization. The identification of all reflection features is summarized in the sketches in Figure 4.4, where the dashed line indicates the strength of the E_x electric field component along the Au-SiO_2 interface and the arrows indicate the corresponding particle polarization. The identification of all modes on this plasmon excitation structure is crucial for the further optimization of resonantly enhanced grating couplers, as the use of small coupler areas will necessitate the use of strongly convergent beams containing significant out-of-plane field components.

4.5 Summary

In summary, a spectroscopic analysis of electron-beam fabricated surface plasmon excitation structures was presented. Reflection measurements revealed various optical resonances that could all be identified by considering the surface plasmon dispersion relation and the anisotropic and frequency-dependent nanoparticle polarizability. The main reflection features were attributed to a lateral particle resonance and a surface plasmon related grating resonance. Varying the grating spacing revealed clear evidence of anticrossing, demonstrating strong coupling between the nanoparticle resonance and the grating resonance. An additional grating mode was found to be excited by incident field components normal to the sample surface and displayed no anticrossing due to the absence of a vertical particle plasmon resonance at the frequencies studied

5 SELECTIVE DETECTION OF PROPAGATING SURFACE PLASMONS EXCITED BY A METAL NANOPARTICLE ARRAY COUPLED TO A NEARBY METAL FILM

5.1 Introduction

The high degree of confinement of surface plasmons (SPs) at a single interface allows for various easily-fabricated single-interface waveguide designs.[2, 4, 15, 16] Dielectric loaded surface plasmon waveguides[2] represent a promising approach, allowing for the development of surface plasmon based optical links on standard silicon integrated circuits without the need for a thick lower cladding layer. In the previous chapters we studied the use of metal nanoparticle arrays near a metal surface for the excitation of propagating single-interface plasmons. Chapter 4 presented experimental results on gold nanoparticle array near an Au-SiO_2, and spectrally resolved reflection measurements provided evidence for two distinct collective resonances of the periodic structure, as well as a broad reflection feature that was attributed to absorption by the localized plasmon resonance of the individual gold nanoparticles. While these assignments could explain the experimental results, the presence of propagating surface plasmons was not directly demonstrated, but rather inferred from the reflection data.

In this chapter, we present leakage radiation measurements on a gold nanoparticle array near an Au-SiO_2 interface. This method enables the direct visualization of propagating surface plasmons, and allows for the identification of the localized surface plasmon mode of the nanoparticles and the propagating surface plasmon modes excited via the particle enhanced grating coupler.

5.2 *Sample Fabrication*

The structure under investigation is shown in Figure 5.1. The sample consists of a gold film deposited on a glass substrate, with nanoparticle arrays fabricated on top of a silica spacer layer. A 5 nm Cr adhesion layer was deposited onto the glass substrate (#1 cover-slip from SPI) using a BOC Edwards FL400 Thermal evaporator. The use of a transparent substrate as opposed to the Si substrate used in Chapter 4 was required to enable transmission measurements and leakage radiation measurements. The Cr deposition was followed immediately by thermal evaporation of 55 nm of gold (gold shot, purity 99.999%, International Advanced Materials) in the same system. Both metals were deposited at a rate of approximately 1 Å/s. Subsequently a 30 nm thick SiO_2 spacer layer was deposited at a rate of approximately 0.9 Å/s by plasma-enhanced chemical vapor deposition in the UnAxis PlasmaTherm 790 PECVD/RIE Reactor using the same process as described in section 4.2. Following the metal and silica depositions, nanoparticle arrays were fabricated on the sample using electron-beam lithography using the same process as described in Chapter 4. For these structures the electron-beam exposure dose used to make the structures was 600 μC/cm^2.

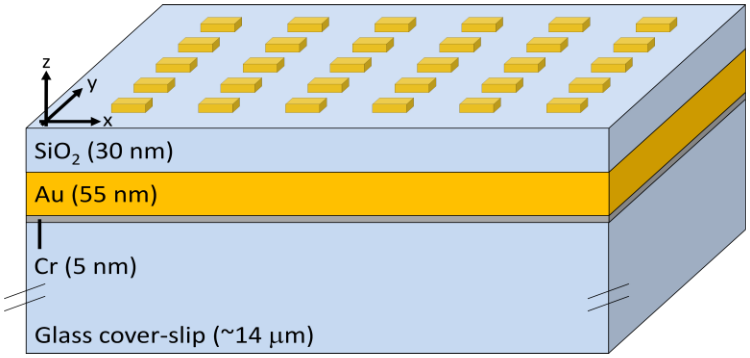

Figure 5.1. Schematic of the structure under investigation.

The nanoparticles were designed to be 130 nm long in the *x*-direction and 50 nm wide in the *y*-direction, giving an aspect ratio (AR = length/width) of 2.6. The arrays had a constant center-to-center spacing along the *y*-direction of 280 nm and a constant center-to-center spacing along the *x*-direction of 600 nm. The number of array periods in the transverse direction was 54, and the number of array periods in the lateral direction was 30, resulting in an array size of approximately 15 µm × 15 µm.

5.3 *Experimental Measurements*

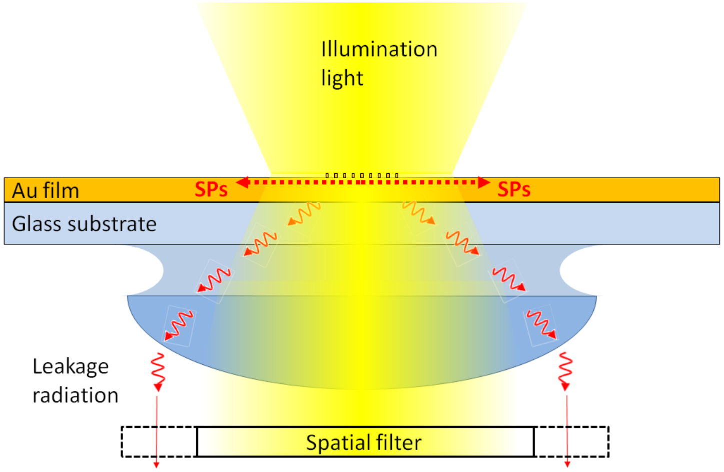

Figure 5.2. A schematic of the setup used to collect the transmission and leakage radiation spectra. For transmission measurements the spatial filter was removed, while for leakage radiation measurements the filter was kept in the collection path to block out the directly transmitted light.

Reflection measurements were done using an upright microscope (Olympus BX51) in combination with a fiber-coupled spectrometer, as described in detail in Chapter 4. The sample was illuminated using a standard halogen light source and a 5× microscope objective of numerical aperture N.A. = 0.15. The illumination was polarized along the *x*-direction. The collected light was sent to a single grating spectrometer via a multimode fiber with a 50 µm diameter core. Using these experimental parameters the collection area was smaller than the size of the array. The reflection spectrum was recorded with a spectral resolution of 7 nm using a thermoelectrically cooled silicon charge-coupled device (CCD) camera attached to the spectrometer at a sensor temperature of 195 K.

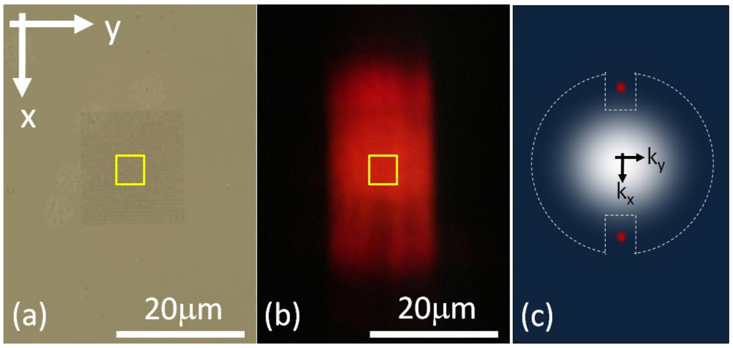

Figure 5.3. Images of the array captured using a CCD camera in (a) direct transmission mode and (b) leakage radiation mode. (c) A sketch of light in the collimated part of the collection path in the microscope. The bright spot in the center is the directly transmitted light, and the red spots on the top and bottom are the high angle leakage radiation corresponding to propagating surface plasmons. The dashed region is blocked off to allow only the high surface plasmon wavevector light to be collected. In panels (a) and (b) the yellow rectangles schematically mark the region of collection for spectroscopic analysis.

A schematic of the transmission and leakage radiation measurements is shown in Figure 5.2. Transmission spectra were taken using an infinity-corrected inverted optical microscope (Olympus IX-71). The sample was illuminated with *x*-polarized light using a standard halogen light source and a condenser with a N.A. of 0.15, equal to the N.A. used in the reflection measurement. The transmitted light was collected using a 60× oil immersion objective with a N.A. of 1.25. For the leakage radiation measurements, a spatial filter was inserted into the collimated part of the collection path to remove the directly transmitted light.

Figure 5.3 shows real-color images of the array in direct transmission mode (panel (a)) and leakage radiation mode (panel (b)). The vertical and horizontal directions correspond to the *x*- and *y*-directions of the sample. In direct transmission (Figure 5.3(a)) the array periods are clearly resolved at the large N.A. provided by the immersion objective. The finite transmitted intensity outside the array area corresponds to direct transmission through the SiO_2-Au-Cr-glass stack, which is estimated to be approximately 5% based on the film thicknesses used.

The leakage radiation (Figure 5.3(b)) corresponds to the same illumination conditions, but blocking the directly transmitted light in the collimated part of the microscope collection path. Figure 5.3(c) is a schematic representation of the light distribution in the collimated part of the collection path, showing a bright central spot corresponding to direct light transmission through the sample, as well as two red spots corresponding to leakage radiation emitted at well-defined large angles along the $+x$ and $-x$ directions. By placing a spatial filter in the collection path as indicated by the dashed outline, any contributions not related to leakage radiation from propagating surface plasmons are selectively suppressed for the leakage radiation measurements, and only intensity from the leaked propagating surface plasmons is imaged. The fact that only red surface plasmons are observed indicates that the plasmon excitation by the grating structure is wavelength dependent, and occurs predominantly at the long wavelength range of the visible spectrum. The leakage radiation was separately confirmed to originate from propagating surface plasmons by two methods. First, rotating the illumination polarization by 90 degrees in-plane resulted in the disappearance of the radiation pattern in Figure 5.3(b), consistent with the longitudinal nature of the excited surface plasmons. Second, scattering of the light at the edges of the array by surface defects was observed in leakage radiation imaging mode for some arrays that happened to have a nearby surface defect (as observed in standard transmission microscopy), confirming that the leaked radiation corresponds to a mode present at the sample surface, and is not an artifact related to the imaging system.

Spectroscopic analysis of the transmitted light and the leakage radiation was done by directing the light to an imaging spectrometer (Horiba Jobin Yvon iHR320) mounted to the microscope. Spectra were recorded using a front-illuminated thermo-electrically cooled silicon charge-coupled device (CCD, Horiba Jobin Yvon Synapse) at a sensor temperature of 203 K. The entrance slit size of the monochromator was set to 50 μm, resulting in a spectral resolution of 7 nm. All spectra taken were corrected by subtracting the detector background signal.

5.4 Results and Discussion

Figure 5.4 shows the results of reflection measurements, transmission measurements, and leakage radiation measurements on the same structure. For the leakage measurements any scattered light not related to leakage radiation was removed by selectively collecting light with a large positive and negative wavevector along the *x*- direction by inserting the spatial filter as schematically indicated in Figure 5.2. The spatial collection region was similar for all measurements in Figure 5.4, and corresponded approximately to the area marked by the rectangle in the center of the array shown in Figure 5.3. To obtain the reflectivity data in Figure 5.4(a), the array was aligned with the collection area of the fiber and the signal $S_R(\lambda)$ was recorded. A reference spectrum $S_{\mathrm{R},ref}(\lambda)$ was taken by measuring the reflected signal of a nearby region without nanoparticles. The relative reflectivity $R_{array}/R_{substrate} = S_R(\lambda)/S_{R,ref}(\lambda)$ thus represents a change in reflectivity due to the presence of the periodic array. The fact that the observed frequency dependent relative reflectivity is less than one indicates that energy was either deposited in the sample, e.g. due to the excitation of localized or propagating surface plasmons, or transmitted more efficiently through the sample due to the presence of the array. Three prominent reflectivity minima are observed at 620 nm, 670 nm, and 760 nm, as indicated by the vertical dotted lines. Based on the work presented in Chapter 4, we expect to observe reflection features related to two grating related features and a feature related to the excitation of a localized plasmon resonance of the Au nanoparticles.[74] However based solely on the reflection spectrum shown in Figure 5.4(a), it is not possible to distinguish between these very different plasmon resonance modes.

Figure 5.4(b) shows the relative transmissivity of the same array. For this measurement, a spectrum of the light transmitted through the array $S_T(\lambda)$ was recorded as a function of wavelength. A reference spectrum $S_{T,ref}(\lambda)$ was taken by measuring the transmission of a nearby region without nanoparticles. The resulting relative transmissivity $T_{array}/T_{substrate} = S_T(\lambda)/ S_{T,ref}(\lambda)$ represents a change in transmissivity of the sample due to the presence of the periodic array. Intriguingly, enhanced transmission is observed around 620 nm and 670 nm, seemingly suggesting that the array of metal particles acts as an anti-reflection coating. In addition, near the location of the previously observed reflection minimum at 760 nm, an asymmetric transmission response is observed: reduced transmission is observed near 725 nm, while increased transmission is observed around 850 nm. Finally, at short wavelengths, the presence of the nanoparticles appears to reduce both the transmission, as well as the reflectivity. This observation will be addressed in more detail below.

Figure 5.4(c) shows the measured leakage radiation spectrum under the same illumination conditions and using the same collection area as for Figure 5.4(b). The spectrum from the location of the array $S_{\mathrm{LR}}(\lambda)$ was recorded as a function of wavelength. A reference spectrum

$S_{ref}(\lambda)$ was taken by measuring the transmission of the glass substrate without any deposited films. The relative leakage radiation signal was calculated as $I_{LR}/I_{in} = S_{LR}(\lambda)/S_{ref}(\lambda)$. The resulting leakage radiation spectrum was scaled to a maximum value of 1, and represents a relative quantity that includes both the plasmon excitation efficiency as well as the surface plasmon leakage efficiency determined by the film thickness.[1] The leakage radiation spectrum displays two clear maxima with similar height and width, occurring at wavelengths close to two of the reflection minima observed in Figure 5.4(a). The fact that these features are observed in a leakage radiation measurement demonstrates that both features correspond to propagating plasmon modes. The fact that propagating surface plasmons can be excited at two distinct wavelengths using an array with a single inter-particle separation along the *x*-direction can be understood as described in detail in Chapter 4.[74] Briefly, the illumination contains field polarization components both along the surface (*x*-direction) and normal to the sample surface (*z*-direction), resulting in *x*-polarization and *z*-polarization of the gold nanoparticles. Both these particle polarization modes induce charge motion in the gold film, and can excite surface plasmons. The resulting grating resonances occur at slightly different frequencies due to the polarization dependent particle polarizability along the *x* and *z* directions. The corresponding particle polarization directions and electric field distributions are shown schematically in Figure 5.4(c). Notably, a very weak and broad shoulder is observed at wavelengths above ~720 nm.

With these observations, it is now possible to understand several features observed in Figure 5.4(a) and Figure 5.4(b). First, the observed reflection minima at 620 nm and 670 nm are due to the deposition of energy into propagating plasmon modes. Second, the broad reflection minimum around 760 nm is likely predominantly due to the excitation of a localized plasmon resonance on the gold nanoparticles, leading to resonantly enhanced absorption. The excitation of a propagating plasmon mode at this wavelength appears to contribute only a relatively small amount of absorption, since only a very weak leakage signal is observed (~5% of the maximum leakage radiation signal). A further discussion of the excitation of propagating surface plasmons near the nanoparticle resonance is presented in Chapter 6.

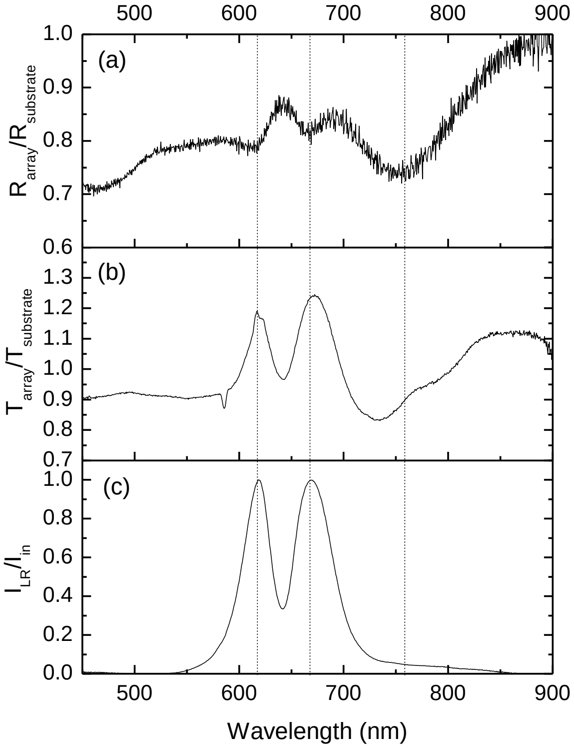

Figure 5.4. A comparison of the (a) reflection spectrum, (b) transmission spectrum, and (c) leakage radiation spectrum of the nanoparticle array. The reflection and transmission spectra were normalized to the corresponding spectra of a nearby area of the sample without the nanoparticle array.

An unexplained feature in Figure 4(b) involves the appearance of an asymmetric transmission feature around the particle resonance frequency. This line shape may be related to the frequency dependent particle polarizability, which is known to resemble the response of a Lorentz resonator. Light scattered in the forward direction by a Lorentz resonator is approximately in phase with the incident light when excited below its resonance frequency, and out of phase with the incident light when excited above its resonance frequency. At low frequencies this leads to constructive interference with the forward propagating incident light, while at high frequencies this leads to destructive interference with the forward propagating incident light. These considerations are consistent with the observed transmission reduction at wavelengths below the nanoparticle resonance and the transmission enhancement at wavelengths above the nanoparticle resonances. We therefore tentatively attribute the observed reduced transmission at wavelengths below 760 nm and increased transmission at wavelengths above 760 nm respectively to destructive and constructive interference of the transmitted light with the scattered dipole radiation by the nanoparticles.

Finally, the observed reduced transmission and reflectivity at wavelengths below 550 nm are tentatively attributed to absorption related to the additional gold contained in the nanoparticles. At these short wavelengths d-band electrons in gold are known to undergo interband transitions upon illumination, resulting in possible additional absorption contribution at wavelengths below ~550 nm.

5.5 Summary

In summary, we studied the optical response of resonant gold nanoparticle gratings near a metal film for exciting propagating surface plasmons. Reflection and transmission spectra show features associated with grating resonances as well as the localized nanoparticle surface plasmon resonance. Direct evidence was provided for the existence of propagating surface plasmons in and around these grating structures using leakage radiation microscopy measurements, and the plasmon radiation pattern was imaged. The reflection, transmission, and leakage radiation measurements were used to elucidate the relative importance of the different surface plasmon excitation mechanisms.

6 FREQUENCY DEPENDENT POWER EFFICIENCY OF A NANOSTRUCTURED SURFACE PLASMON COUPLER

6.1 Introduction

The previous chapters discussed coupling structures for coupling to surface plasmons based on periodic placement of plasmon resonant particles near a metal surface. Though the relative efficiency of these structures was studied as a function of particle shape (Chapter 2, numerical study), particle volume (Chapter 3, numerical study), and array period (Chapter 4, experimental study), the absolute efficiency of plasmon excitation could not be determined. In Chapter 5, leakage radiation microscopy and spectroscopy was used to collect a signal that was proportional to the surface plasmon intensity at the metal surface, enabling the selective detection of propagating modes excited by nanoparticle enhanced grating structures. In this chapter we focus on determining the absolute power efficiency of miniature plasmon couplers.

A variety of structures have been investigated for coupling light from free-space to surface plasmons. Hibbens *et*. *al*. investigated the use of a dielectric grating to excited surface plasmons on a nearby metal surface at microwave frequencies.[53, 77] Worthington *et*. *al*. measured the efficiency of out-coupling from surface plasmons to radiation via a square grating at 60%.[78] Ditlbacher *et*. *al*. measured monochromatic efficiency of coupling light into surface plasmons using a small line-grating on a film of thickness where the radiative loss of the surface plasmons into the high index substrate is exactly equal to the non-radiative losses in the metal film.[79] Giannattasio *et*. *al*. investigated the geometrical dependence of a square grating profile in exciting monochromatic surface plasmons on a metal film.[54] Lu *et*. *al*. numerically investigated the unidirectional excitation of surface plasmons by a freely modified finite grating to find a maximum coupling efficiency of 50%.[80] Large[73] and small[74] nanoparticle enhanced grating couplers have been investigated for exciting surface plasmons in an underlying metal film, and have shown a possible coupling efficiency of up to 60% in both cases as measured via a reduction in reflectivity. Recently Chengkun *et. al*. numerically investigated the coupling from a Gaussian beam into long range surface plasmons on a thin gold film and optimized the structure to find a coupling efficiency of approximately 19%.[81] Calculating the absolute coupling efficiency for coupling into surface plasmons is a challenge; the direct measurements of coupling efficiency into surface plasmons have been either using numerical simulations[80], or monochromatic and for a specific film thickness[79].

In this chapter we extend the leakage radiation spectroscopy measurements described in Chapter 5. We study a gold nanoparticle based grating coupler similar to the arrays studied in Chapter 5, and develop a general method that can be used to measure the absolute spectral coupling efficiency for a wide variety of coupling structures.

6.2 Theory

Leakage radiation measurements as described in Chapter 5 provide a signal proportional to the surface plasmon intensity at the metal surface. However to determine the absolute surface plasmon excitation efficiency a method is needed to relate the collected signal to the incident irradiance on the coupler structure. To obtain this relation we consider a 3-layer system extended infinitely in the *x*-*y* plane consisting of a central metal layer of thickness *d* surrounded by transparent semi-infinite top (cover) and bottom (substrate) layers. Surface plasmons are excited primarily on the cover-metal interface via a nanostructured array illuminated from the top, and the refractive index of the substrate is chosen to be higher than the refractive index of the cover layer.

The efficiency η of surface plasmon excitation by the nanostructured array is defined as the ratio of the total power coupled into surface plasmons propagating away from the array, $P_{SP,tot}$, to the total power incident on the coupling structure P_{inc}:

$$\eta = \frac{P_{SP,tot}}{P_{inc}}. \tag{6.1}$$

The total power deposited into propagating surface plasmons is dissipated by either radiative or non-radiative means, giving

$$P_{SP,tot} = P_{SP,rad} + P_{SP,i} \tag{6.2}$$

where $P_{SP,rad}$ is the power of the surface plasmon dissipated radiatively via leakage radiation into the substrate, and $P_{SP,i}$ is the power of the surface plasmon dissipated via intrinsic losses in the metal (non-radiative losses). In steady state, the ratio of the radiative and intrinsic dissipation of the surface plasmon power is equal to the ratio of the calculated rates of dissipation of the surface plasmon fields. That is,

$$\frac{P_{SP,i}}{P_{SP,rad}} = \left(\frac{\Gamma_i}{\Gamma_{rad}}\right) \tag{6.3}$$

where Γ_{rad} is the rate of radiative loss of the surface plasmon electric field amplitude determined by the film thickness and the surrounding refractive indices, and Γ_i is and rate of intrinsic loss of the surface plasmon electric field amplitude. Note that the latter rate Γ_i is related to but not equal to the electron scattering rate in the metal, and may be calculated explicitly as described in detail in Section 3.4. Combining equations (6.1) and (6.2) , and substituting for $P_{SP,tot}$ into eqn. (6.3) gives:

$$\eta = \frac{P_{SP,rad}}{P_{inc}} \cdot \left(1 + \left(\frac{\Gamma_i}{\Gamma_{rad}}\right)\right). \tag{6.4}$$

The ratio Γ_i / Γ_{rad} for a smooth metal film can be calculated from known material properties based on the following approach (described in part in Ref. [1]). We consider the complex surface plasmon wavevector $k_x = k_x' + ik_x''$ of the two-layer semi-infinite cover-metal interface, where k_x' and k_x'' are the real and imaginary parts of the surface plasmon wavevector respectively, and *x* is the direction of surface plasmon propagation. The metal-substrate interface is assumed to have a very small effect on the metal-cover surface plasmon dispersion relation, which is a valid assumption when $e^{2ik_{z,m}''d} << 1$, where $k_{z,m}''$ is the imaginary part of the *z*-component of the surface plasmon wavevector in the metal film. Under these conditions one can obtain an expression for the complex change in surface plasmon wavevector due to the finite film thickness and the presence of the substrate given by[1]:

$$\Delta k_x = r_{sm}^{TM} \cdot e^{2ik_{z,m}''d} \cdot 2 \cdot \left(\frac{\omega}{c}\right) \cdot \left(\frac{\varepsilon_m \varepsilon_c}{\varepsilon_m + \varepsilon_c}\right)^{3/2} \cdot \left(\frac{1}{\varepsilon_c - \varepsilon_m}\right) \tag{6.5}$$

where ε_m and ε_c are the complex dielectric constants of the metal film and the cover layer respectively, r_{sm}^{TM} is the electric field amplitude reflection coefficient of the substrate-metal interface for TM-polarized light incident on the metal from the substrate side, $\omega = \frac{2\pi c}{\lambda_0}$ with λ_0

the free-space wavelength, and *c* is the speed of light in vacuum. Since $k_x^{"}$ is proportional to Γ_i, and $\Delta k_x^{"}$, the imaginary part of Δk_x, is proportional to Γ_{rad}, we have:

$$\left(\frac{\Gamma_i}{\Gamma_{rad}}\right)=\left(\frac{k_x^{"}}{\Delta k_x^{"}}\right). \tag{6.6}$$

Based on the calculated values for Γ_i/Γ_{rad} we can now obtain the frequency dependent coupling efficiency η (equation (6.4)) by measuring $P_{SP,rad}$ and P_{inc}. In principle P_{inc} can be measured by measuring the transmitted power though an area of the sample that is not coated with metal and that has the same size as the coupling structure under consideration. In the present approach we instead measure the normal incidence transmitted power P_T through an unpatterned but metal coated area of the sample integrated over an area equivalent to the array size, given by $P_T = P_{inc} \times T$ with *T* the normal incidence transmissivity of the unpatterned sample . The transmissivity can either be calculated based on the known film thickness and optical properties, or measured separately. Combining equations (6.1) and (6.2) leads to:

$$\eta=\frac{P_{SP,rad}}{P_T}\cdot T\cdot\left(1+\left(\frac{k_x^{"}}{\Delta k_x^{"}}\right)\right). \tag{6.7}$$

Equation (6.1) shows that a frequency dependent surface plasmon excitation efficiency can be obtained through a simple comparison of the measured radiated and transmitted power, combined with an either calculated or measured transmissivity and the analytically calculated wavevectors.

6.3 Sample Fabrication

The sample is similar to that discussed in Chapter 5 (see Figure 5.1). A detailed description of the sample fabrication is provided in Section 5.2. In brief, the sample consists of a gold film deposited on a glass substrate, with nanoparticle arrays fabricated on top of a silica spacer layer. A 5 nm Cr adhesion layer was deposited onto a glass cover slip, followed by thermal evaporation of a 55 nm thick gold layer. Subsequently a 30 nm thick SiO_2 spacer layer was deposited by plasma-enhanced chemical vapor deposition. Nanoparticle arrays were fabricated on the SiO_2 spacer layer using electron-beam lithography as described in Section 4.2. A 5 nm Cr adhesion layer was deposited onto an electron-beam patterned polymethyl methacrylate (PMMA) layer on the sample, followed by a 35 nm thick gold layer. After lift-off, a gold nanoparticle array remains on the SiO_2 surface. The nanoparticles were designed to be 130 nm long in the *x*-direction and 50 nm wide in the *y*-direction, giving an in-plane aspect ratio (AR = length/width) of 2.6. The particles had a constant center-to-center spacing in the *x*- and *y*-directions of 600 nm and 280 nm respectively. The array contains 20 and 54 periods in the *x*- and *y*-direction respectively, giving an array size of approximately 10 μm × 15 μm.

6.4 Experimental Measurements

For spectral analysis the sample was top-illuminated with light from a standard halogen light source, via a condenser of numerical aperture (N.A.) 0.15. The incident light was polarized along the *x*-direction before entering the condenser, resulting in polarization in the *x*-z plane at the sample due to focusing by the condenser. Surface plasmons were excited on the top metal film surface via the nanoparticle grating. For this gold film thickness, the presence of surface plasmons at the top Au surface leads to a small amount of leakage radiation into the substrate. The leakage radiation measurement was performed as described in detail in section 5.3. Briefly, leakage radiation from propagating surface plasmons was collected using a 60× oil immersion objective with a N.A. of 1.25. A drop of index matching oil (n = 1.516) was placed between the substrate and the objective. A spatial filter was inserted near the optical axis in the collimated part of the collection path to remove the directly transmitted light and allow the imaging of only the large-wavevector leakage radiation for surface plasmons propagating along the positive and negative *x*-directions. For normal incidence transmission measurements on unpatterned regions of the sample the spatial filter was removed.

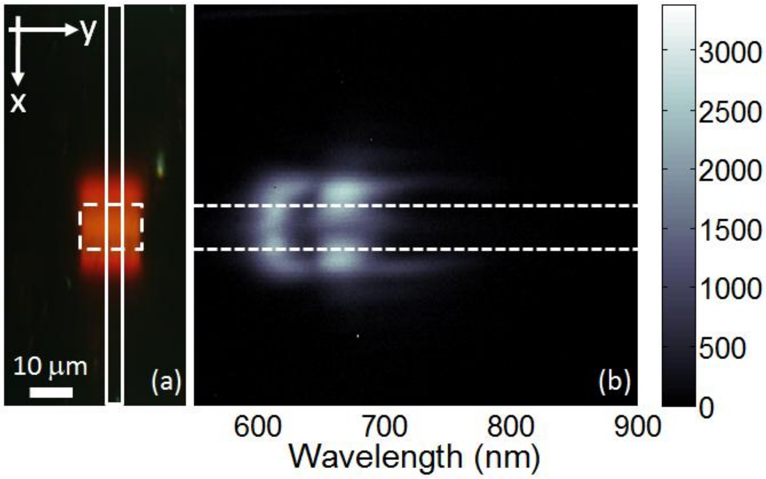

Figure 6.1. (a) Image of surface plasmons excited by the array captured using a CCD camera in leakage radiation mode. (b) Spectroscopic composition of the light collected from the solid rectangular area in panel (a). The horizontal dashed lines mark the edges of the array.

Figure 6.1(a) shows an image of the collected leakage radiation recorded using a digital camera. The dashed rectangle marks the location of the array, and surface plasmons can be seen to be propagating in the positive and negative *x*-directions. For spectral analysis the collected light was projected onto the entrance slit of an imaging spectrometer (Horiba Jobin Yvon iHR320). The region of the image collected through the entrance slit is shown schematically by the solid rectangle in Figure 6.1(a). Spectra were recorded using a silicon charge coupled device (CCD, Horiba Jobin Yvon Synapse). All spectral measurements were corrected for the corresponding detector background signal. The entrance slit size was set to 50 μm, resulting in a spectral resolution of 7 nm. Figure 6.1(b) shows the thus obtained spatially resolved leakage radiation spectrum. The vertical direction in the image corresponds to the position along the direction of surface plasmon propagation (x-direction). The color represents the intensity of the leakage radiation at each wavelength and spatial coordinate. The dashed horizontal lines mark the edges of the array.

6.5 Results and Discussion

In order to determine the quantity $P_{SP,rad}/P_T$ used in equation (6.3) the power in the leakage radiation of propagating surface plasmons was measured by integrating the signal corresponding to surface plasmons propagating away from the array $S_{LR}(\lambda)$ over the x-dimension – the regions above and below the dashed lines in Figure 6.1(b). The transmitted signal through the deposited film, $S_T(\lambda)$, was collected over an area equal to the array size (area between dashed lines in Figure 6.1(b)) using the same detection parameters as used for $S_{LR}(\lambda)$. Figure 6.2(a) shows the resulting ratio $S_{LR}(\lambda)/S_T(\lambda)$. Since both S_{LR} and S_T contain the lamp spectrum and the wavelength dependent detector sensitivity, we have $S_{LR}(\lambda)/S_T(\lambda) = P_{SP,rad}/P_T$.

Figure 6.2(b) shows the wavelength dependent transmissivity of the film given by $T = (1 - R_s) \cdot S_T(\lambda)/S_s(\lambda)$, where R_s is the reflectivity of the uncoated glass substrate (R = 0.04) and $S_s(\lambda)$ is the measured transmitted signal through the substrate measured in an uncoated and unpatterned region of the sample. The transmissivity is seen to drop continuously as the wavelength is increased, as expected for a continuous metal film.

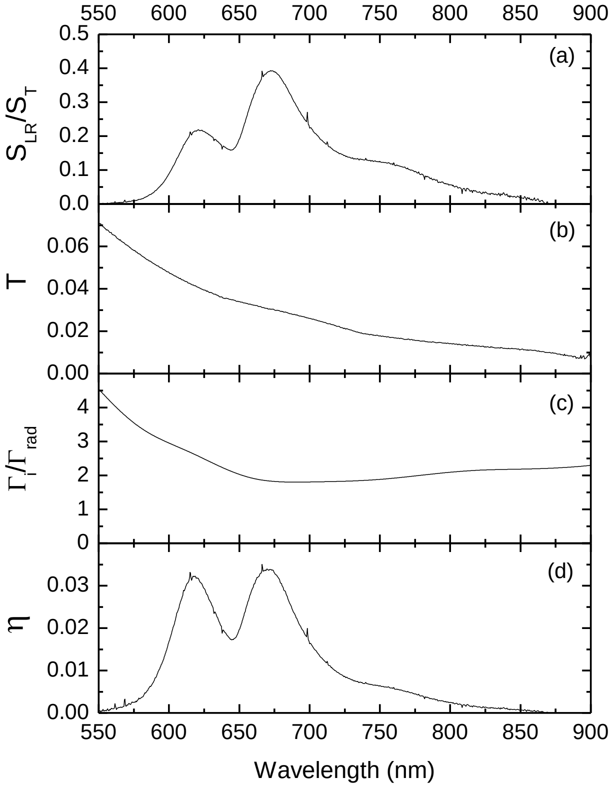

Figure 6.2. Spectra of (a) Leakage radiation from surface plasmons excited on the film, normalized to the transmission through the film, (b) the transmissivity of the film, (c) the wavelength dependent ratio Γ_i/Γ_{rad}, and (d) the wavelength dependent efficiency η of coupling to surface plasmons. The two peaks near 620 nm and 670 nm are related to the propagating surface plasmons excited constructively by the grating.

Figure 6.2(c) shows the wavelength dependent ratio Γ_i / Γ_{rad} calculated using equations (6.5) and (6.6) in combination with literature values for the material properties[48] and the gold film thickness parameters of the sample. Note that scattering of surface plasmons by film roughness was assumed to be negligible in this analysis; dark field images of the unpatterned sample showed very little optical scattering. To account for the 30 nm SiO_2 spacer layer, an effective dielectric function $\varepsilon_c = 1.05$ was used as the dielectric function of the cover layer in the calculations of Δk_x. The bottom 5 nm Cr adhesion layer was replaced in the calculation by an additional 5 nm of Au. Note that these approximations were not necessary for calculating the r_{sm}^{TM} term in equation (6.5) . It was found that $e^{2ik''_{z,m}d} < 0.035$ for all wavelengths considered based on the literature values for the dielectric function of Au and assuming a film thickness of 60 nm, satisfying the previously discussed requirement $e^{2ik''_{z,m}d} << 1$ for the validity of equation (6.5) .

Figure 6.2(d) shows the obtained spectral coupling efficiency η of the nanoparticle grating coupler evaluated using equation (6.1) and the measurements of $P_{SP,rad}/P_T$, T, and the calculated values of Γ_i / Γ_{rad}. Two main peaks are observed in the efficiency of surface plasmon excitation. Based on the grating spacing and the surface plasmon dispersion, it is expected that under normal plane-wave illumination surface plasmons excited by each row of particles will interfere constructively with the surface plasmons excited by neighboring rows for a free-space wavelength of approximately 630 nm. The two main peaks in the efficiency lie above and below the expected wavelength of the grating resonance. Chapter 4 of nanoparticle arrays near a thick metal film has shown that these two peaks correspond to grating modes excited by the *x*- and *z*-polarization of the illumination, and are a necessary result of convergent illumination. This conclusion was confirmed by verifying the dependence of the collected intensity for each mode in response to changing the N.A. of the illumination. Increasing the illumination N.A. (not shown) leads to an enhancement of the peak at 675 nm, demonstrating that the peak near 675 nm corresponds to the *z*-polarized grating mode, and the peak near 625 nm corresponds to the *x*-polarized grating mode. In addition to the two grating related surface plasmon excitation peaks, a broad and weak peak is observed at approximately 770 nm. Excitation of surface plasmons at wavelengths far from grating resonance seems counter-intuitive, since no constructive addition of surface plasmon amplitude is possible. However, it should be noted that the individual Au nanoparticles support a dipolar plasmon resonance. Isolated ellipsoidal Au nanoparticles with dimensions 130 nm × 50 nm × 35 nm are predicted to have a resonance frequency of 592 nm in air, and 727 nm in SiO_2 based on literature dielectric functions. The relatively large size of the particles will lead to a red-shift of the resonance, and interaction with the metal surface will lead to an additional red-shift due to the excitation of an oscillatory image charge distribution[62]. We therefore attribute the broad peak at 770 nm to the excitation of surface plasmons by the resonantly excited local fields around the rows of particles near the edge of the array. Interestingly, Figure 6.1(b) shows that little leakage radiation at 770 nm is collected within the array, but measurable leakage radiation intensity is observed just outside the array (above and below the dashed lines). This observation is tentatively ascribed to destructive interference of leakage radiation by out-of-phase contributions from different rows within the array.

The maximum efficiency of the structure observed in Figure 6.2(d) occurs at the two grating resonances, and is approximately 3.5%. Note that this figure indicates the useful excited surface plasmon power, i.e. it does not include any surface plasmon power dissipated within the excitation structure. This relatively low efficiency does not reflect the maximum attainable efficiency. Simulations of a similar structure – an infinite array of ellipsoidal silver nanoparticles embedded in SiO_2 and near a silver surface – show that the surface plasmon excitation strength depends critically on the particle-surface separation, showing a rapid drop in excited surface plasmon amplitude for small particle-surface spacing.[82] In the study, the strength of the excited surface plasmon was observed to increase with increasing particle distance from the metal film, and then decrease beyond an optimum particle-surface separation. Thus, changing the thickness of the spacer layer could increase the coupling efficiency further. Finally, the illumination used in the present work is highly convergent with an N.A. of 0.15. Since the incident light contains several angles of incidence and the plasmon excitation is angle dependent, it is likely that the obtained efficiency represents a lower limit to the actual efficiency. It is important that this is only a limitation of the illumination method. Using the same method as described here, and applying illumination at a smaller numerical aperture will provide an improved estimate of the absolute surface plasmon excitation efficiency.

6.6 Summary

The wavelength dependent surface plasmon excitation efficiency of a miniature nanoparticle enhanced grating coupler was determined using spatially resolved leakage radiation spectroscopy. A generally applicable method for determining the wavelength dependent efficiency of plasmon excitation structures exciting propagating surface plasmons on a thin metal film. It was found that the constructive excitation of propagating surface plasmons led to an increase in the excited surface plasmon amplitude at the grating resonance. The maximum observed coupling efficiency was approximately 3.5%, possibly limited by the numerical aperture of the illumination optics.

7 SATURATION OF SURFACE PLASMON EXCITATION IN A NANOPARTICLE ENHANCED GRATING COUPLER AS A FUNCTION OF ARRAY SIZE

7.1 Introduction

The previous chapters discussed the excitation of surface plasmon by a periodic array of nanoparticles near a metal film. The coupling between particle and grating resonances was predicted (Chapter 2), modeled (also Chapter 2), and measured (Chapter 4). The understanding of excitation and scattering of propagating surface plasmons developed in Chapter 3 (numerical simulations) allowed us to make predictions about the saturation of surface plasmon excitation in finite arrays (Section 3.5). Chapters 5 and 6 presented methods to measure the relative and absolute efficiency of exciting propagating surface plasmons. In this chapter we use the surface plasmon characterizing tools presented in Chapter 5 to test the effect of array size on surface plasmon excitation and find a maximum array size for useful excitation of surface plasmons.

In this work we spectroscopically investigate small gold nanoparticle grating-like structures coupled via a nearby metal film. We study the evolution of polarization dependent modes in the grating, and show that there is an optimum array size for exciting surface plasmons on the metal film. We present a mechanism for this saturation based on a discussion of the balance between the increased surface plasmon amplitude due to the constructive addition of surface plasmons excited by neighboring grating periods and scattering of already propagating surface plasmons by the same array periods.

7.2 Sample preparation

The structure under investigation is similar to that sketched in Chapter 5, Figure 5.1, and a detailed description of the sample fabrication process is presented in section 5.2. In brief, the sample consists of a gold plasmon guiding layer on a glass substrate, with shape tuned nanoparticle arrays defined on a thin silica spacer layer. The guiding layer was prepared by depositing a 5 nm thick Cr adhesion layer onto the glass cover slip substrate, followed by thermal evaporation of a 55 nm thick gold layer. Subsequently a 30 nm thick SiO_2 spacer layer was deposited by plasma-enhanced chemical vapor deposition. Nanoparticle arrays were fabricated on the SiO_2 spacer layer by depositing a 5 nm Cr adhesion layer onto an electron beam patterned and developed polymethyl methacrylate (PMMA) layer on the sample, followed by the deposition of a 35 nm thick gold layer. After lift-off, gold nanoparticle arrays remain on the SiO_2 surface. The nanoparticles were designed to have a length $L_x = 100$ nm along the *x*-direction and a width of $L_y = 70$ nm along the *y*-direction, giving an in-plane aspect ratio AR = $L_x/L_y = 1.4$. Note that these particle dimensions are different than those used in Chapters 5 and 6 in order to bring the nanoparticle plasmon resonance closer to the location of the grating resonances. The inter-particle center-to-center spacing along the *x*- and *y*-directions was 600 nm and 280 nm respectively. At this inter-particle spacing, normal incidence excitation of propagating surface plasmons is expected to occur at $\lambda = 632$ nm for weak particle-film interaction, based on the known dielectric functions and film thicknesses used. All fabricated arrays contain 54 periods along the *y*-direction. The number of periods along the *x*-direction, *N*, was varied from 1 to 21, giving a maximum $x \times y$ array size of approximately 10 μm × 15 μm.

7.3 Experimental Measurements

Transmission measurements and leakage radiation measurements of the nanoparticle arrays were carried out in an inverted microscope. The sample was top-illuminated with light from a standard halogen light source, using a brightfield condenser of numerical aperture (N.A.) 0.45. The incident light was *x*-polarized before the condenser, resulting in the presence of both *x*-polarization and *z*-polarization components at the sample surface after focusing by the condenser. Surface plasmons excited at the top Au-SiO_2 interface via the nanoparticle array were spatially and spectrally analyzed using leakage radiation microscopy. The leakage radiation measurement was performed as described in detail in Section 5.3. Briefly, leakage radiation from propagating surface plasmons was captured via an oil immersion objective (magnification 60×, N.A. = 1.25). Index matching fluid of $n = 1.516$ was placed between the substrate and the objective to allow the high angle leakage radiation to be collected. A spatial filter, as sketched in Figure 7.1(b), was inserted into the collimated part of the collection path to collect only the propagating surface plasmon-related leakage radiation. The collected light was imaged onto a digital camera, or projected onto the entrance slit of a monochromator for spectral analysis. Leakage radiation spectra were measured using an imaging spectrometer (Horiba Jobin Yvon iHR-320) mounted to the microscope. Spectra were recorded using a thermo-electrically cooled silicon charge-coupled device (CCD, Horiba Jobin Yvon Synapse) at a sensor temperature of 203 K. The entrance slit size was set to 50 μm, and the corresponding spectral resolution was 7 nm. The integration time for all spectra was 60 seconds. For all spectral measurements the corresponding dark spectrum was subtracted to remove the CCD background signal.

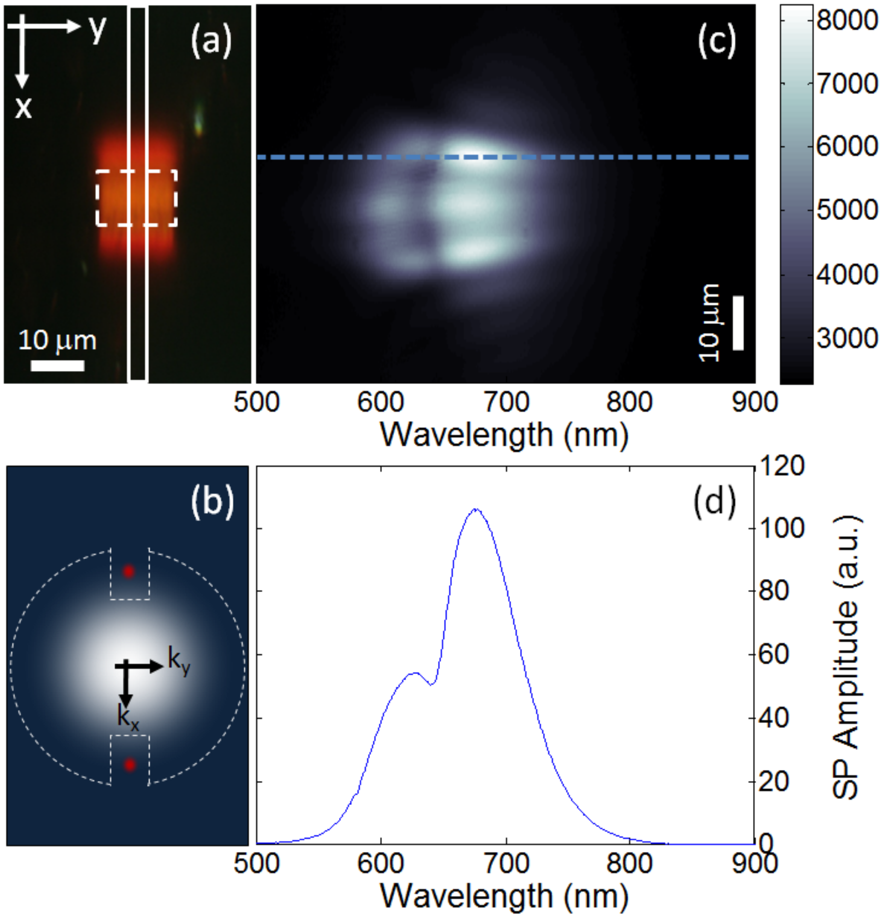

Figure 7.1. (a) A leakage radiation image of an array with 20 periods captured using a CCD camera. The dashed rectangle marks the location of the array. The solid vertical rectangle schematically marks the area of the slit from which spectra were collected. (b) Schematic representation of light in the collimated part of the collection path in the microscope. The bright spot in the center indicates the directly transmitted light, and the red spots on the top and bottom are the high angle leakage radiation corresponding to propagating surface plasmons. The dashed region is blocked off to allow only the large-wavevector surface plasmon related contributions to be collected. (c) Spatially resolved spectrum of the collected surface plasmon related radiation. The blue dashed line marks the location surface plasmon amplitude exiting the array. (d) Spectrum of the maximum surface plasmon amplitude leaving the array, collected from the *x*-position indicated by the dashed line in panel (b).

7.4 Results and Discussion

Figure 7.1(a) shows a real-color leakage radiation (LR) image collected from an array with 20 periods in the *x*-direction illuminated with white light polarized in the *x*-*z* plane. The dashed rectangle indicates the location of the array. The image was obtained after spatial filtering of the transmitted light. Figure 7.1(b) represents a schematic representation of the light distribution in the collimated part of the collection path, showing a bright central spot corresponding to direct light transmission through the sample, as well as two red spots corresponding to leakage radiation emitted at well-defined large angles along the +*x* and –*x* directions. By placing a spatial filter in the collection path as indicated by the dashed outline, any contributions not related to leakage radiation from propagating surface plasmons are selectively suppressed. Note that the collected leakage radiation seen in Figure 7.1(a) extends ~20 μm beyond the edge of the array in both the +*x* and –*x* directions. The fact that the collected radiation appears red indicates that the surface plasmons are excited most efficiently at relatively long wavelengths. Rotating the spatial filter and the incident polarization by 90° in the *x*-*y* plane causes the extended surface plasmon features to disappear, confirming that the collected radiation is related to longitudinal surface plasmon waves.

To evaluate the spectrally resolved excitation efficiency for each array, part of the image in Figure 7.1(a) was imaged onto the entrance slit of a monochromator as indicated schematically by the solid white rectangle. The spectrally dispersed image was projected onto the CCD camera. Figure 7.1(c) shows the corresponding spatially resolved leakage radiation spectrum of the array shown in Figure 7.1(a). The light is dispersed by wavelength along the horizontal axis, while the vertical direction corresponds to the direction of surface plasmon propagation (*x*-direction). The color represents the intensity of the light collected at each location and wavelength coordinate. To obtain a signal representative of the surface plasmon intensity launched from the array, the leakage radiation spectrum just outside the array was collected. The collection region is marked by the dashed line in Figure 7.1(c). The leakage radiation spectrum was normalized to the lamp spectrum transmitted through the uncoated glass substrate. Figure 7.1(d) shows the obtained normalized leakage radiation spectrum calculated as $S_{LR}(\lambda)/S_{ref}(\lambda)$. Two distinct peaks are visible in the leakage spectrum at wavelengths close to the wavelength of 632 nm expected for weak nanoparticle-film interaction based on the inter-particle spacing and the Au and SiO_2 film thickness. The origin of these features will be discussed in detail below. Note that in panel (c) a minimum is observed in the collected leakage radiation near the edge of the array. This observation is tentatively attributed to presence of a weak contribution of light scattered directly by the nanoparticles into the substrate. Due to the periodicity of the array, the collectively excited nanoparticles are expected to produce both a zero order scattering signal along the system optical axis, as well as two first order diffraction peaks into the substrate determined by the inter-particle spacing. This diffracted order necessarily occurs at the same angle as the leakage radiation, since the in-plane wavevector and therefore the radiation angle of both contributions is determined by the grating periodicity. Destructive interference of this directly scattered light with the leakage radiation could give rise to the observed suppression of leakage radiation signal within the array.

In order to determine the surface plasmon excitation efficiency as a function of array size, the measurement shown in Figure 7.1(d) was repeated for 21 arrays with identical particle shape and spacing, but with a varying number of periods *N* ranging from 1 to 21. All leakage radiation spectra were taken at the same distance from the edge of the array to enable a direct comparison of the excited surface plasmon intensity. Figure 7.2 summarizes the thus obtained leakage radiation spectra a function of the number of periods. The wavelength-dependent surface plasmon intensity excited by each array is indicated by the height and color of the traces. For *N* = 1, a single peak near a wavelength of 650 nm is observed with a linewidth of ~90 nm. As *N* is increased from 1 to 7 periods, the collected leakage radiation intensity is seen to increase rapidly, followed by a gradual saturation of the excited intensity for larger numbers of periods. Additionally, the single peak observed for *N* = 1 is seen to split into two distinct features as N is increased, eventually leading to the well resolved peaks observed in Figure 7.1(d) for *N* = 20 occurring at 3.08×10^{15} rad/s (615 nm) and 2.75×10^{15} rad/s (685 nm), as obtained from a two-peak Lorentz fit.

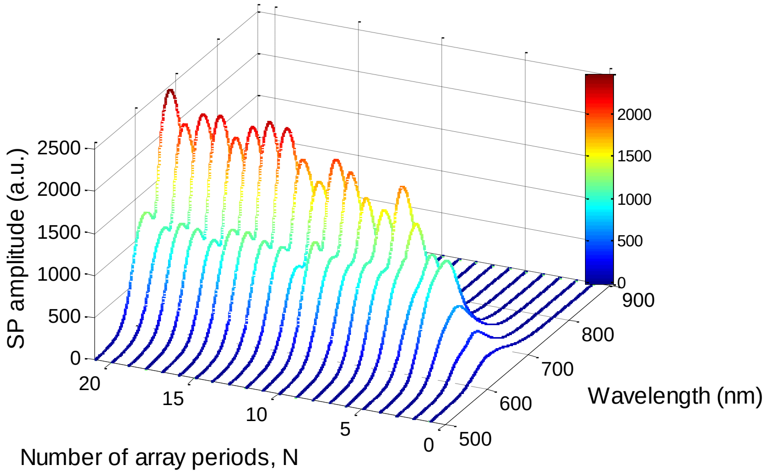

Figure 7.2. Absolute surface plasmon amplitude leaving arrays with 1 to 21 periods, normalized to the illumination spectrum.

The observation of a well defined resonance feature at λ = 650 nm in the leakage radiation spectrum for *N* = 1 seems surprising, since no periodic structure is present along the *x*-direction, and consequently no grating modes can exist along this direction. However, it should be noted that the calculated dipolar nanoparticle plasmon resonance frequency for isolated Au nanoparticles of this aspect ratio in air is predicted to occur at ~540 nm based on theoretical calculations. From ref. [62] it is expected that the resonance wavelength of the nanoparticle be red-shifted due to the close proximity to the metal substrate. Consequently the observed resonance in the leakage radiation signal for $N = 1$ is attributed to the excitation of propagating surface plasmons through the resonantly enhanced local fields from the Au nanoparticles at frequencies near the nanoparticle resonance. This interpretation is supported by the close correspondence of the observed linewidth of ~90 nm with the theoretically obtained linewidth of 90 nm for an ellipsoidal Au nanoparticle of axes 100 nm × 70 nm × 35 nm in air (not shown). As N is increased, the single peak is seen to split into two peaks that rapidly separate and arrive close to their limiting peak position for $N \approx 7$. The high and low frequency peaks are tentatively assigned to x- and z-polarized grating modes respectively, as identified by N.A. dependent measurements (not shown) similar to those performed in Chapter 4.[74] Reducing the N.A. was found to reduce the amplitude of the long wavelength peak relative to the short wavelength peak, suggesting that the high frequency mode is x-polarized in nature mode, and that the low frequency mode is predominantly z-polarized.

The data presented in Figure 7.2 lead to several important observations. First, the mode that was attributed to z-polarized excitation near $\lambda = 685$ nm is stronger than the short wavelength mode that was assigned to x-polarized surface plasmon excitation near $\lambda = 615$ nm. This is surprising, since the illumination N.A. of 0.45 corresponds to a maximum illumination angle of 26^{o}. Even at this high angle of incidence the ratio between the z-component and the x-component of the incident field is 0.49, leading to a corresponding maximum intensity ratio between the two excitation modes of 0.24. The relatively large contribution of the z-polarized mode may be related to the incident field distribution near the sample surface. In the absence of Au nanoparticles, the high reflection from the Au-SiO_2 interface leads to a standing wave pattern above the sample. The difference in amplitude reflection coefficients for *s*- and *p*-polarized light is expected to lead to a strongly reduced E_x amplitude at the metal surface. Although analyzing the final field distribution near the particle array is complicated due to the contribution of significant absorption and scattering by the nanoparticles, it seems likely that reflection from the interface would similarly reduce the E_x contribution near the nanoparticles, leading to a relatively enhanced E_z excitation of surface plasmon modes.

Since the observed grating modes change amplitude and spectral location a function of N, the determination of the surface plasmon excitation efficiency at a fixed wavelength does not provide a clear picture of the excitation process. Instead, the excited surface plasmon intensity for each array was evaluated by integrating the normalized leakage radiation spectrum over all wavelengths. Figure 7.3 shows the thus obtained integrated leakage radiation intensity as a function of N (circles). Note that the point (0,0) was added to the dataset since for $N = 0$, the surface plasmon amplitude must necessarily be 0. Significant scatter is observed in the experimental data due to fabrication variations from array to array. Despite these fluctuations, the data clearly shows a rapid increase in the total excited surface plasmon intensity as the number of periods is increased, and a gradually decreasing contribution to the total intensity by each additional array period. Based on this observation, the array size dependence of the surface plasmon intensity was empirically modeled with the function $\left(1 - e^{-N/N_{sat}}\right)$, where N_{sat} represents the array size at which the total surface plasmon intensity comes within 1/e of its saturation value. The resulting fit is shown as the solid line in Figure 7.3. From the fit, N_{sat} was found to be 7.7, as marked by the vertical dashed line in Figure 7.3.

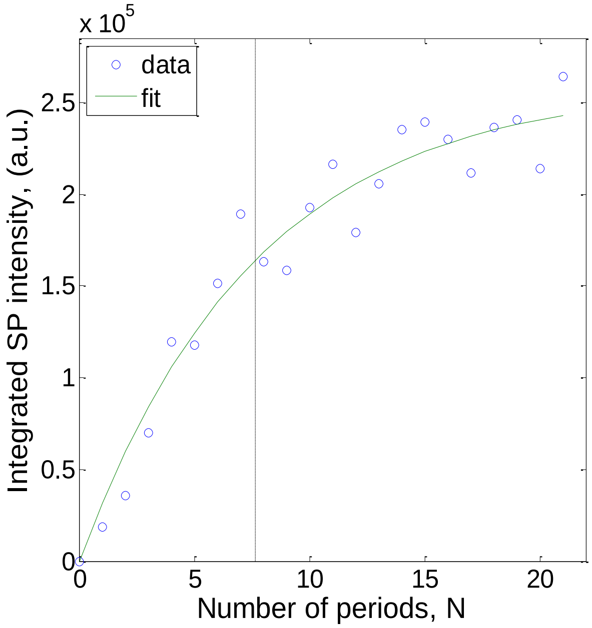

Figure 7.3. Integrated surface plasmon amplitude (circles) as a function of the number of array periods *N*. The solid line is an emperical exponential fit to the data. The dashed line marks the number of periods needed to reach 1/e of the saturation intensity, derived from the fit.

The saturation of the surface plasmon excitation as a function of *N* can be understood by considering the effect of each additional line of nanoparticles on the propagating surface plasmons. In the case of a single array period (*N* = 1), surface plasmons are excited by the single row of nanoparticles and propagate away. As the array size increases, surface plasmons excited by each additional particle row interfere constructively with the surface plasmons excited by previous particle rows, resulting in a larger excited surface plasmon intensity. However, as surface plasmons propagating within the array encounter additional particle rows, each row dissipates some of the incident surface plasmon intensity both radiatively and non-radiatively.

Thus, each additional array period (1) *excites* surface plasmons that interfere constructively with already present surface plasmons at wavelengths close to the grating spacing, and (2) *introduces additional damping* of the already propagating surface plasmons. Consequently, optimum surface plasmon excitation requires a balance between additional surface plasmon excitation and additional damping of already excited surface plasmons. In the case of the structure under investigation it appears that this optimum occurs a approximately 8 array periods, which corresponds to a compact array size of approximately 4 μm.

7.5 Summary

In conclusion, spectroscopic measurements were presented of surface plasmons excited on a metal film by a resonant gold nanoparticle array. The formation of two grating modes corresponding to *x*- and *z*-polarized modes was observed in the coupled array-film system. Consideration of the total excited surface plasmon amplitude shows that saturation of the excited surface plasmon amplitude is reached rapidly as a function of array size. The mechanism of this saturation was explained in terms of a balance between amplification of the surface plasmon amplitude by neighboring particle rows and reduction of any existing surface plasmon amplitude by these same particles. Under the presented illumination conditions the optimum array size was found to be as small as 4 μm.

8 SUMMARY AND OUTLOOK

The behavior of metal nanoparticle arrays in proximity to a metal surface was studied using numerical, theoretical, and experimental techniques with the intention of using a combination of the metal nanoparticle resonance and the grating resonance to excite surface plasmons on the metal surface. The strong coupling between resonantly excited near-field around the metal nanoparticles was anticipated to lead to the possibility of developing miniature surface plasmon excitation devices.

A nanoparticle-enhanced plasmon excitation structure consisting of a periodic array of ellipsoidal Ag nanoparticles in close proximity to a Ag-SiO_2 interface was studied under normal illumination using full-field simulations in Chapter 3. Varying the nanoparticle geometry enabled control over the nanoparticle resonance and consequently the frequency dependent surface plasmon excitation. A second resonance – the grating resonance – associated with the constructive excitation of surface plasmons on the film due to the periodic arrangement of the nanoparticles was observed. Strong coupling between the particle resonance and the grating resonance was observed as evidenced by anti-crossing of the particle and grating resonances. The coupled system was successfully modeled as a system of coupled Lorentz oscillators. It was observed that for infinite arrays the maximum surface plasmon field amplitude was *not* achieved when the particle resonance frequency and grating resonance frequency were matched. These observations were explained in terms of a balance between nanoparticle induced damping and intrinsic surface plasmon damping at the Ag-SiO_2 interface.

The effect of particle volume on the excitation of surface plasmons at the grating resonance was investigated via further full-field simulations in Chapter 3. The structure was similar to that in Chapter 2, and the surface plasmon excitation strength at the grating resonance was studied as a function of particle volume for three cases – two where the particle resonance was far from the grating resonance and one where the particle resonance was close to the grating resonance. The effect of the particle resonance was observed primarily via particle-induced damping of the surface plasmon on the metal film. We compared the damping as found through the grating resonance linewidth observed in the simulations to independently calculated nanoparticle contributions to the surface plasmon damping. This provided insight into the physical mechanism of the surface plasmon excitation and damping. We found that the minimum damping of the surface plasmon in the system was limited by the intrinsic damping of the surface plasmon in the metal film. The maximum damping of the surface plasmon was found to exhibit saturation at the volume of the nanoparticle at which the nanoparticle optical cross-section equals the area of the unit cell under consideration. The simulations suggested that the resonance frequency of the nanoparticle surface plasmon is not a critical parameter in the optimization of surface plasmon excitation in infinite arrays if the particle volume can be arbitrarily chosen. The maximum surface plasmon amplitude occurs due to the combined effect of an increased excitation of surface plasmons as the particle volume increases, counteracted by an increase in the particle-induced damping at large particle volumes.

Finite arrays of electron-beam fabricated finite gold nanoparticles separated by a thin SiO_2 spacer layer from a thick gold film were studied under convergent illumination using reflection spectroscopy in Chapter 4. Numerical aperture dependent reflection measurements showed that the strength of the surface plasmons excited by the in-plane-polarized illumination could selectively be increased. Varying the grating spacing to scan the grating resonance through the lateral particle resonance showed a strong interaction between the two resonances, and the anticrossing predicted in Chapter 2 was reproduced experimentally. Due to the convergent illumination, an additional grating mode was excited by the polarization normal to the sample surface. This mode displayed no interaction with the lateral particle resonance. Instead, the reflection minima associated with this mode were seen to closely follow the calculated surface plasmon dispersion relation, indicating weak interaction of the surface plasmon with vertical particle polarization. The large observed mode splitting demonstrates that strong particle-surface plasmon interactions can be obtained experimentally by proper design of the nanoparticle resonance and the grating spacing.

In Chapter 5 leakage radiation microscopy was used to investigate the frequency dependent surface plasmon excitation process. While reflection and transmission spectra provided indirect evidence of surface plasmon excitation and particle-induced absorption, the leakage radiation measurements directly demonstrated the presence of propagating surface plasmons.

In Chapter 6 we presented a method for measuring the free-space surface plasmon excitation efficiency through a finite size coupling structure. The method described used leakage radiation measurements, and can be used to evaluate the wavelength dependent efficiency of a wide variety of plasmon excitation structures. The wavelength dependent surface plasmon excitation efficiency of a miniature nanoparticle enhanced grating coupler was determined and found to be highest at the two polarization-dependent grating resonances discussed in Chapters 5 and 6. The relatively long-wavelength nanoparticle resonance was found to only weakly excite surface plasmons due to the lack of constructive excitation by the periodic array. The maximum observed coupling efficiency was approximately 3.5%.

Chapter 7 studied the array-size dependent surface plasmon excitation. The formation of two grating modes was observed corresponding to *x*- and *z*-polarized modes of the array-film coupled system. A study of the total excited surface plasmon amplitude showed that saturation of the excited surface plasmon amplitude was reached rapidly as a function of array size. This saturation was understood by considering the balance between an increase of surface plasmon amplitude by adding additional periods, and the resulting increased surface plasmon absorption and scattering of the already propagating surface plasmon amplitude by these same periods. It was found that the optimum array size for exciting surface plasmons was as small as 8 periods, corresponding to a 4 μm array size.

The leakage radiation measurements in Chapter 7 all showed relatively high efficiency of surface plasmon excitation at the two grating resonances. Notably, the *z*-polarized grating resonance showed a higher efficiency compared to the *x*-polarized grating resonance, even though the illumination angle was only 26^o. This was attributed to the larger amplitude of the E_z field of the surface plasmon compared to the incident E_x amplitude.

The insights from the numerical study of varying the particle volume presented in Chapter 3 were supported by the investigation of surface plasmon excitation amplitude as a function of array size in Chapter 7. We found that increasing the array size increased the strength of the surface plasmon leaving the array, but with diminishing returns; the strength of the surface plasmon leaving the array saturated within 10 array periods. In addition to array size, the saturation length is also expected to vary with particle volume, in a fashion similar to the behavior observed in the simulations. It is expected that for arrays with particles of smaller volume (smaller cross-section, smaller surface plasmon excitation and damping via nanoparticle) the saturation length would be longer compared to that for arrays with particles of relatively larger volume (larger cross-section, larger surface plasmon excitation and damping via nanoparticle). Thus, a study similar to that in Chapter 7, but with particles of different volumes would elucidate the surface plasmon excitation mechanism further. In addition, as noted in Chapter 6, changing the spacer thickness is expected to affect surface plasmon excitation efficiency. An experimental study of surface plasmon excitation efficiency as a function of array size would yield the optimum spacer thickness for such a miniature nanoparticle coupler.

The development of a high efficiency compact coupling structure is with the goal of possible on-chip communication. Towards this end, the next step would be to couple the excited surface plasmons into waveguides. This involves two steps. One is to develop arrays to focus the excited surface plasmons into a focal point to couple into surface plasmons. This would involve initial phased-array calculations for designing such an array. The second step is to create the waveguides on the metal layer and the array above the spacer layer. This will require developing a process for 2-step electron-beam exposure. While involved, the additional steps are not expected to raise insurmountable challenges, and demonstration of such a device should be feasible.

While similar compact coupling elements could be designed using suspended metal line arrays, nanoparticle arrays have distinct practical advantages over line arrays for the excitation of surface plasmons. Varying the nanoparticle spacing in the direction normal to surface plasmon propagation can be used for beam-shaping of the excited surface plasmons, effectively offering a way to tune the plasmon excitation strength within each line. This design freedom is expected to be useful for efficient coupling into surface plasmon waveguides. In addition, for experimental investigation, nanoparticles have three controllable dimensions compared to two for line arrays, and the third dimension allows for easier control of resonances of the individual structures. In contrast, line arrays are much easier to fabricate compared to nanoparticle arrays. Thus, nanoparticle arrays are useful for experimental studies and for fine-tuning the spectral and spatial response of the structure, enabling in-depth investigation of the fundamental physical processes affecting device performance, while line arrays could be used for near-optimal device-level implementation.

The recent development of surface plasmon based lasers[21, 22] presents the exciting possibility of combining a nanoparticle based laser with structures similar to those investigated in this work to excite surface plasmons. Such a structure would have the distinct advantage of combining the light source and coupler structure, allowing for a compact on-chip plasmon source with a tailored in-plane radiation pattern.

9 REFERENCES

1. Raether, H., *Surface Plasmons on Smooth and Rough Surfaces and on Gratings*. Springer Tracts in Modern Physics. Vol. 111. 1988, Berlin: Springer-Verlag.
2. Steinberger, B., et al., *Dielectric stripes on gold as surface plasmon waveguides.* Applied Physics Letters, 2006. **88**(9): p. 094104.
3. Krenn, J.R., et al., *Non diffraction-limited light transport by gold nanowires.* Europhysics Letters, 2002. **60**(5): p. 663-669.
4. Pile, D.F.P., et al., *Numerical analysis of coupled wedge plasmons in a structure of two metal wedges separated by a gap.* Journal Of Applied Physics, 2006. **100**(1): p. 013101.
5. Pile, D.F.P., et al., *Two-dimensionally localized modes of a nanoscale gap plasmon waveguide.* Applied Physics Letters, 2005. **87**(26): p. 261114.
6. Gramotnev, D.K. and D.F.P. Pile, *Single-mode subwavelength waveguide with channel plasmon-polaritons in triangular grooves on a metal surface.* Applied Physics Letters, 2004. **85(**26): p. 6323-6325.
7. Pile, D.F.P. and D.K. Gramotnev, *Channel plasmon-polariton in a triangular groove on a metal surface.* Optics Letters, 2004. **29**(10): p. 1069-1071.
8. Tanaka, K. and M. Tanaka, *Simulations of nanometric optical circuits based on surface plasmon polariton gap waveguide.* Applied Physics Letters, 2003. **82**(8): p. 1158-1160.
9. Leosson, K., et al., *Long-range surface plasmon polariton nanowire waveguides for device applications.* Optics Express, 2006. **14**(1): p. 314-319.
10. Nikolajsen, T., et al., *Polymer-based surface-plasmon-polariton stripe waveguides at telecommunication wavelengths.* Applied Physics Letters, 2003. **82**(5): p. 668-670.

11. Bozhevolnyi, S.I., et al., *Waveguiding in surface plasmon polariton band gap structures.* Physical Review Letters, 2001. **86**(14): p. 3008-3011.

12. Dionne, J.A., et al., *Plasmon slot waveguides: Towards chip-scale propagation with subwavelength-scale localization.* Physical Review B, 2006. **73**(3): p. 035407.

13. Maier, S.A., et al., *Local detection of electromagnetic energy transport below the diffraction limit in metal nanoparticle plasmon waveguides.* Nature Materials, 2003. **2**(4): p. 229.

14. Krenn, J. and J. Weeber, *Surface plasmon polaritons in metal stripes and wires.* Philosophical Transactions of the Royal Society A: Mathematical, Physical and Engineering Sciences, 2004. **362**(1817): p. 739-756.

15. Weeber, J.-C., Y. Lacroute, and A. Dereux, *Optical near-field distributions of surface plasmon waveguide modes.* Physical Review B (Condensed Matter and Materials Physics), 2003. **68**(11): p. 115401.

16. Tanaka, K., M. Tanaka, and T. Sugiyama, *Simulation of practical nanometric optical circuits based on surface plasmon polariton gap waveguides.* Optics Express, 2005. **13**(1): p. 256-266.

17. Nikolajsen, T., K. Leosson, and S.I. Bozhevolnyi, *Surface plasmon polariton based modulators and switches operating at telecom wavelengths.* Applied Physics Letters, 2004. **85**(24): p. 5833-5835.

18. Bozhevolnyi, S.I., et al., *Channel plasmon subwavelength waveguide components including interferometers and ring resonators.* Nature, 2006. **440**(7083): p. 508-511.

19. Maier, S.A., et al., *Observation of near-field coupling in metal nanoparticle chains using far-field polarization spectroscopy.* Physical Review B, 2002. **65**(19): p. 193408.

20. Maier, S.A., P.G. Kik, and H.A. Atwater, *Observation of coupled plasmon-polariton modes in Au nanoparticle chain waveguides of different lengths: Estimation of waveguide loss.* Applied Physics Letters, 2002. **81**(9): p. 1714-1716.

21. Bergman, D.J. and M.I. Stockman, *Surface Plasmon Amplification by Stimulated Emission of Radiation: Quantum Generation of Coherent Surface Plasmons in Nanosystems.* Physical Review Letters, 2003. **90**(2): p. 027402.

22. Stockman, M.I., *Spasers explained.* Nat Photon, 2008. **2**(6): p. 327-329.

23. Thaxton, C.S., D.G. Georganopoulou, and C.A. Mirkin, *Gold nanoparticle probes for the detection of nucleic acid targets.* Clin Chim Acta, 2005. **363**(1-2): p. 120-126.

24. Michaels, A.M., M. Nirmal, and L.E. Brus, *Surface Enhanced Raman Spectroscopy of Individual Rhodamine 6G Molecules on Large Ag Nanocrystals.* Chem. Phys, 1999. **87**: p. 4189-4200.

25. Felidj, N., et al., *Controlling the optical response of regular arrays of gold particles for surface-enhanced Raman scattering.* Physical Review B, 2002. **65**(7).

26. Felidj, N., et al., *Gold particle interaction in regular arrays probed by surface enhanced Raman scattering.* Journal Of Chemical Physics, 2004. **120**(15): p. 7141-7146.

27. Laurent, G., et al., *Raman scattering images and spectra of gold ring arrays.* Physical Review B, 2006. **73**(24): p. 245417/5.

28. Homola, J., S.S. Yee, and G. Gauglitz, *Surface plasmon resonance sensors: review.* Sensors and Actuators B: Chemical, 1999. **54**(1): p. 3-15.

29. Schuck, P., *Use of surface plasmon resonance to probe the equilibrium and dynamic aspects of interactions between biological macromolecules.* Annual Review of Biophysics and Biomolecular Structure, 1997. **26**(1): p. 541-566.

30. Bennink, R.S., Y.K. Yoon, and R.W. Boyd, *Accessing the optical nonlinearity of metals with metal-dielectric photonic bandgap structures.* Opt. Lett, 1999. **24**: p. 1416-1418.

31. Takeda, Y., et al., *Optical switching performance of metal nanoparticles fabricated by negative ion implantation.* Nuclear Inst. and Methods in Physics Research, B, 2006. **242**(1-2): p. 194-197.

32. Scalisi, A.A., et al., *Nonlinear optical activity in Ag-SiO*$_2$ *nanocomposite thin films with different silver concentration.* Applied Surface Science, 2004. **226**: p. 237-241.

33. Zhan, C., et al., *The excited-state absorption and third-order optical nonlinearity from 1-dodecanethiol protected gold nanoparticles: Application for optical limiting.* Optical Materials, 2004. **26**(1): p. 11-15.

34. Pillai, S., et al., *Surface plasmon enhanced silicon solar cells.* Journal Of Applied Physics, 2007. **101**(9).

35. Anthony, J.M., et al., *Plasmon-enhanced solar energy conversion in organic bulk heterojunction photovoltaics.* Applied Physics Letters, 2008. **92**(1): p. 013504.

36. Carl, H., et al., *Electromagnetic coupling of light into a silicon solar cell by nanodisk plasmons.* Applied Physics Letters, 2008. **92**(5): p. 053110.

37. Catchpole, K.R. and A. Polman, *Design principles for particle plasmon enhanced solar cells.* Applied Physics Letters, 2008. **93**(19): p. 191113.

38. Catchpole, K.R. and A. Polman, *Plasmonic solar cells.* Opt. Express, 2008. **16**(26): p. 21793-21800.

39. Keisuke, N., T. Katsuaki, and A.A. Harry, *Plasmonic nanoparticle enhanced light absorption in GaAs solar cells.* Applied Physics Letters, 2008. **93**(12): p. 121904.

40. Ting-Yen, C., B. Shieh, and K.C. Saraswat. *Impact of Joule heating on scaling of deep sub-micron Cu/low-k interconnects*. in *Symposium on VLSI Technology, 2002. Digest of Technical Papers.* 2002.

41. Miller, D.A.B., *Rationale and challenges for optical interconnects to electronic chips.* Proceedings of the IEEE, 2000. **88**(6).

42. Bohr, M.T. *Interconnect scaling-the real limiter to high performance ULSI*. in *Electron Devices Meeting, International*. 1995. Washington, DC, USA.

43. Bozhevolnyi, S.I., *Plasmonic Nanoguides and Circuits*. 2008, Singapore: Pan Stanford Publishing.

44. Brongersma, M.L. and P.G. Kik, *Surface Plasmon Nanophotonics*. Surface Plasmon Nanophotonics, Edited by ML Brongersma and G., ed. W.T. Rhodes. 2007, AA Dordrecht: Springer. 268.

45. Zia, R., et al., *Plasmonics: the next chip-scale technology.* Materials today, 2006. **9**(7-8): p. 20-27.

46. Tucker, R.S., *Energy Consumption in Digital Optical ICs With Plasmon Waveguide Interconnects.* Photonics Technology Letters, IEEE, 2007. **19**(24): p. 2036-2038.

47. Foteinopoulou, S., J.P. Vigneron, and C. Vandenbem, *Optical near-field excitations on plasmonic nanoparticle-based structures.* Opt. Express, 2007. **15**(7): p. 4253-4267.

48. Johnson, P.B. and R.W. Christy, *Optical Constants of the Noble Metals.* Physical Review B, 1972. **6**(12): p. 4370-4379.

49. Palik, E.D., *Handbook of optical constants of solids.* Academic Press Handbook Series, New York: Academic Press, 1985, edited by Palik, Edward D., 1985.

50. Boyd, G.T., Z.H. Yu, and Y.R. Shen, *Photoinduced luminescence from the noble metals and its enhancement on roughened surfaces.* Physical Review B (Condensed Matter), 1986. **33**(12, Part 1): p. 7923.

51. Mohamed, M.B., et al., *The 'lightning' gold nanorods: fluorescence enhancement of over a million compared to the gold metal.* Chemical Physics Letters, 2000. **317**(6): p. 517.

52. Bohren, C.F. and D.R. Huffman, *Absorption and Scattering of Light by Small Particles*. 1998, New York: John Wiley & Sons, Inc.

53. Hibbins, A.P., J.R. Sambles, and C.R. Lawrence, *The coupling of microwave radiation to surface plasmon polaritons and guided modes via dielectric gratings.* Journal of Applied Physics, 2000. **87**(6): p. 2677.

54. Giannattasio, A., I.R. Hooper, and W.L. Barnes, *Dependence on surface profile in grating-assisted coupling of light to surface plasmon-polaritons.* Optics Communications, 2006. **261**(2): p. 291-295.

55. Powell, C.J. and J.B. Swan, *Origin of the Characteristic Electron Energy Losses in Aluminum.* Physical Review, 1959. **115**(4): p. 869-875.

56. Powell, C.J. and J.B. Swan, *Origin of the Characteristic Electron Energy Losses in Magnesium.* Physical Review, 1959. **116**(1): p. 81-83.

57. Hecht, B., et al., *Local Excitation, Scattering, and Interference of Surface Plasmons.* Physical Review Letters, 1996. **77**(9): p. 1889-1892.

58. Zou, S.L., N. Janel, and G.C. Schatz, *Silver nanoparticle array structures that produce remarkably narrow plasmon lineshapes.* Journal Of Chemical Physics, 2004. **120**(23): p. 10871-10875.

59. Zou, S.L. and G.C. Schatz, *Narrow plasmonic/photonic extinction and scattering line shapes for one and two dimensional silver nanoparticle arrays.* Journal Of Chemical Physics, 2004. **121**(24): p. 12606-12612.

60. Sweatlock, L.A., et al., *Highly confined electromagnetic fields in arrays of strongly coupled Ag nanoparticles.* Physical Review B, 2005. **71**(23): p. 235408.

61. Griffiths, D.J., *Introductions to Electrodynamics*. 1999, New Jersey: Prentice-Hall.

62. Takemori, T., M. Inoue, and K. Ohtaka, *Optical-Response Of A Sphere Coupled To A Metal-Substrate.* Journal Of The Physical Society Of Japan, 1987. **56**(4): p. 1587-1602.

63. Evlyukhin, A.B. and S.I. Bozhevolnyi, *Surface plasmon polariton scattering by small ellipsoid particles.* Surface Science, 2005. **590**(2-3): p. 173-180.

64. *Microwave Studio*. 2006, Computer Simulation Technology: Darmstadt, Germany.

65. Ghoshal, A. and P.G. Kik, *Theory and simulation of surface plasmon excitation using resonant metal nanoparticle arrays.* Journal Of Applied Physics, 2008. **103**: p. 113111.

66. Weiland, T., *Eine Methode zur Losung der Maxwellschen Gleichungen fur sechskomponentige Felder auf diskreter Basis.* AEU, 1977. **31**: p. 116–120.

67. Soennichsen, C., et al., *Plasmon resonances in large noble-metal clusters.* New Journal of Physics, 2002. **4**: p. 93.1-93.8.

68. Ghoshal, A. and P.G. Kik, *Excitation of propagating surface plasmons by a periodic nanoparticle array: Trade-off between particle-induced near-field excitation and damping.* Applied Physics Letters, 2009. **94**: p. 251102.

69. *Microwave Studio Suite*. 2008, Computer Simulation Technology: Darmstadt, Germany.

70. Klar, T., et al., *Surface-Plasmon Resonances in Single Metallic Nanoparticles.* Physical Review Letters, 1998. **80**(19): p. 4249/4.

71. Oldenburg, S.J., et al., *Light scattering from dipole and quadrupole nanoshell antennas.* Applied Physics Letters, 1999. **75**(8): p. 1063-1065.

72. Wang, H., et al., *Light scattering from spherical plasmonic nanoantennas: effects of nanoscale roughness.* Applied Physics B-Lasers And Optics, 2006. **84**(1-2): p. 191-195.

73. Chu, Y. and K.B. Crozier, *Experimental study of the interaction between localized and propagating surface plasmons.* Opt. Lett., 2009. **34**(3): p. 244-246.

74. Ghoshal, A., I. Divliansky, and P.G. Kik, *Experimental observation of mode-selective anticrossing in surface-plasmon-coupled metal nanoparticle arrays.* Applied Physics Letters, 2009. **94**(17): p. 171108-3.

75. Madou, M., *Fundamentals of Microfabrication.* Contact. **650**: p. 926-2411.

76. Ward, C.A., et al., *Multimedia dispersion relation for surface electromagnetic waves.* Journal of Chemical Physics, 1975. **62**(5): p. 1674.

77. Hibbins, A.P., J.R. Sambles, and C.R. Lawrence, *Grating-coupled surface plasmons at microwave frequencies.* Journal of Applied Physics, 1999. **86**(4): p. 1791-1795.

78. Worthing, P.T. and W.L. Barnes, *Efficient coupling of surface plasmon polaritons to radiation using a bi-grating.* Applied Physics Letters, 2001. **79**(19): p. 3035.

79. Ditlbacher, H., et al., *Efficiency of local light-plasmon coupling.* Applied Physics Letters, 2003. **83**(18): p. 3665-3667.

80. Lu, J., et al., *Numerical optimization of a grating coupler for the efficient excitation of surface plasmons at an Ag-SiO_2 interface.* Journal of the Optical Society of America B-Optical Physics, 2007. **24**(9): p. 2268-2272.

81. Chengkun, C. and P. Berini, *Broadside Excitation of Long-Range Surface Plasmons via Grating Coupling.* Photonics Technology Letters, IEEE, 2009. **21**(24): p. 1831-1833.

82. Ghoshal, A. and P.G. Kik, *Optimization of surface plasmon excitation using resonant nanoparticle arrays above a silver film.* Proc. SPIE, 2007. **6641**: p. 7.